

AD A0 66606

DDC FILE COPY

C

LEVEL II

2

AFFDL-TR-78-72

**FACTORS INFLUENCING THE ACCURACY OF
AERODYNAMIC HINGE-MOMENT PREDICTION**

*WEN-FAN LIN
MICHAEL D. CLARKE
BOEING AEROSPACE COMPANY
P. O. BOX 3999
SEATTLE, WASHINGTON 98124*

AUGUST 1978

TECHNICAL REPORT AFFDL-TR-78-72
Final Report April 1977 - April 1978

Approved for public release; distribution unlimited.

AIR FORCE FLIGHT DYNAMIC LABORATORY
AIR FORCE WRIGHT AERONAUTICAL LABORATORIES
AIR FORCE SYSTEMS COMMAND
WRIGHT-PATTERSON AIR FORCE BASE, OHIO 45433

DDC
RECEIVED
MAR 30 1979
D


[Handwritten signature]

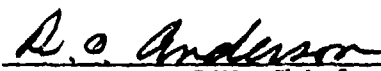
NOTICE

When Government drawings, specifications, or other data are used for any purpose other than in connection with a definitely related Government procurement operation, the United States Government thereby incurs no responsibility nor any obligation whatsoever; and the fact that the government may have formulated, furnished, or in any way supplied the said drawings, specifications, or other data, is not to be regarded by implication or otherwise as in any manner licensing the holder or any other person or corporation, or conveying any rights or permission to manufacture, use, or sell any patented invention that may in any way be related thereto.

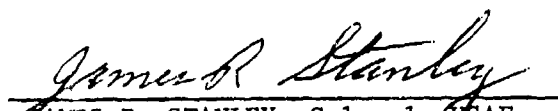
This report has been reviewed by the Information Office (OI) and is releasable to the National Technical Information Service (NTIS). At NTIS, it will be available to the general public, including foreign nations.

This technical report has been reviewed and is approved for publication.


JERRELL W. SOUTHERN, 1Lt, USAF
Project Engineer
Control Dynamics Branch


R. O. ANDERSON, Chief
Control Dynamics Branch
Flight Control Division

FOR THE COMMANDER


JAMES R. STANLEY, Colonel, USAF
Chief, Flight Control Division

"If your address has changed, if you wish to be removed from our mailing list, or if the addressee is no longer employed by your organization please notify AFFDL/FGC, W-PAFB, OH 45433 to help us maintain a current mailing list".

Copies of this report should not be returned unless return is required by security considerations, contractual obligations, or notice on a specific document.

UNCLASSIFIED

SECURITY CLASSIFICATION OF THIS PAGE (When Data Entered)

REPORT DOCUMENTATION PAGE		READ INSTRUCTIONS BEFORE COMPLETING FORM
1. REPORT NUMBER	2. GOVT ACCESSION NO.	3. RECIPIENT'S CATALOG NUMBER
4. TITLE (and Subtitle)		5. TYPE OF REPORT & PERIOD COVERED
6. AUTHOR(s)		7. PERFORMING ORG. REPORT NUMBER
8. PERFORMING ORGANIZATION NAME AND ADDRESS		9. CONTRACT OR GRANT NUMBER(s)
10. PROGRAM ELEMENT, PROJECT, TASK AREA & WORK UNIT NUMBERS		11. REPORT DATE
12. CONTROLLING OFFICE NAME AND ADDRESS		13. NUMBER OF PAGES
14. MONITORING AGENCY NAME & ADDRESS (if different from Controlling Office)		15. SECURITY CLASS. (of this report)
16. DISTRIBUTION STATEMENT (of this Report)		15a. DECLASSIFICATION/DOWNGRADING SCHEDULE
17. DISTRIBUTION STATEMENT (of the abstract entered in Block 20, if different from Report)		
18. SUPPLEMENTARY NOTES		
19. KEY WORDS (Continue on reverse side if necessary and identify by block number)		
20. ABSTRACT (Continue on reverse side if necessary and identify by block number)		

19

12 AFFDL-TR-78-72

6

FACTORS INFLUENCING THE ACCURACY OF AERODYNAMIC HINGE-MOMENT PREDICTION

10

Wen-Fan/Lin
Michael D./Clarke

Boeing Aerospace Company
P.O. Box 3999
Seattle, Washington 98124

Air Force Flight Dynamics Laboratory (FGC)
Air Force Systems Command
Wright-Patterson Air Force Base, Ohio 45433

Final Report
April 1977 - April 1978

D180-24604-1

F33615-76-C-3170

2403-05-13

August 1978

106

Unclassified

Approved for public release; distribution unlimited.

FLEXSTAB Singular loading TEA 230
Hinge moments Datcom PAN AIR pilot program
Control surface RHO 4
YF-16

This report is concerned with factors influencing the accuracy of aerodynamic hinge-moment analyses. The formulation and coding of the hinge-moment analysis in the FLEXSTAB system of computer programs are reviewed. The investigation is centered on the sensitivity of the hinge moments of the YF-16 airplane to paneling configuration, including the near-field/far-field techniques. The results are compared with test data. The effect of elasticity is also considered.

(Abstract continued on back)

UNCLASSIFIED

20.

Abstract (continued)

↙ The other existing aerodynamic methods for predicting control-surface loading are also reviewed and discussed. These methods include Datcom, RHO 4, higher order lifting-surface methods such as TEA 230 and the PAN AIR pilot program, and new theoretical approaches employing asymptotic expansion methods to account for local hinge-line, corner, and side-edge effects. Recommendations are made as to the best approach currently to employ in the panel methods, as well as future research areas related to hinge-moment analysis. ↗

Unclassified

SECURITY CLASSIFICATION OF THIS PAGE(When Data Entered)

FOREWORD

The work described in this report was performed by Boeing Aerospace Company, Seattle, Washington, under Air Force contract F33615-76-C-3170, task No. 3. The AFFDL task number 2403-05, "Design Methods for Aeroelastic Military Flight Vehicles," was under project number 2403, "Stability and Control of Aerospace Vehicles."

The work was directed by the Control Dynamics Branch, Flight Control Division, Air Force Flight Dynamics Laboratory, Air Force Systems Command, Wright-Patterson Air Force Base, Ohio. The work was administered by Lt. Ron Johnson and Lt. Jerry Southern of the Control Dynamics Branch.

Mr. Donald L. Grande was the program manager. Dr. Wen-Fan Lin and Mr. Michael D. Clarke, senior engineers at Boeing Aerospace Company, were the investigators. Mr. Gerald M. Dornfeld, specialist engineer and prime investigator on the contract, assisted in the review.

This report covers work from April 1977 to April 1978. The report was submitted by the authors in August 1978.

LEVEL II

ADDRESS TO	
DTIC	White Section <input checked="" type="checkbox"/>
DDO	Dist Section <input type="checkbox"/>
UNANNOUNCED	<input type="checkbox"/>
JUSTIFICATION	
BY	
DISTRIBUTION/AVAILABILITY CODE	
Dist.	AVAIL. AND/OR SPECIAL
A	

DDC
RECEIVED
MAR 30 1979
D

TABLE OF CONTENTS

Section	Page
I INTRODUCTION	1
II FLEXSTAB PROGRAM REVIEW AND DEMONSTRATION	2
2.1 Hinge-Moment Formulation and Code	2
2.2 Hinge-Moment Analysis for YF-16	3
2.2.1 Comparison of AFFDL and Boeing Results for Basic Panelled Model	3
2.2.2 Investigation of Other Paneling Configurations	4
III REVIEW AND DISCUSSION OF EXISTING HINGE-MOMENT ANALYSIS METHODS	6
3.1 FLEXSTAB Method	8
3.1.1 Aerodynamics in the FLEXSTAB System	8
3.1.2 Computation of Hinge Moment	11
3.1.3 Discussion of Numerical Characteristics	12
3.2 Datcom Methods	15
3.2.1 Method of Computing Hinge-Moment Derivative $C_{h\alpha}$	16
3.2.2 Method of Computing Hinge-Moment Derivative $C_{h\delta}$	17
3.2.3 Numerical Results for YF-16 Wing	18
3.2.4 Discussion of Datcom Methods	22
3.3 RHO 4 Method	23
3.3.1 Collocation Method of RHO 4	23
3.3.2 Discussion of RHO 4 Method	25
3.4 TEA 230 Method	27
3.4.1 Potential-Flow Theory	27
3.4.2 Numerical Method of TEA 230	29
3.4.3 Discussion of TEA 230 Method and Solutions	32
3.5 PAN AIR Pilot Program Method	34
3.5.1 Outline of PAN AIR Method	34
3.5.2 Discussion of PAN AIR Method	37
3.6 Summary of Methodologies of Potential-Flow Programs	39
IV RECOMMENDATIONS FOR THE BEST APPROACH USING THE FLEXSTAB METHOD	39
4.1 Integral Representation of Differential Problems	39
4.2 Methods of Solving Integral Equation	40
4.3 Improved FLEXSTAB Method of Solving Integral Equation	43

TABLE OF CONTENTS (Continued)

Section	Page
V RECOMMENDATIONS FOR FUTURE RESEARCH AREAS FOR HINGE-MOMENT ANALYSIS	48
VI CONCLUSIONS	52
REFERENCES	55

LIST OF ILLUSTRATIONS

Figure	Page
1 YF-16 Model With Basic Paneling	57
2 YF-16 Model With Low-Dens.ity Near-Field/Far-Field Simulation	58
3 YF-16 Model With "Improved" Paneling	59
4 Typical Loading on Control Surface	60
5 Breakpoint Edge Redefinition	61
6 Typical Load and Downwash Distributions on a Constant-Pressure Panel and on a Wing in Subsonic Flow	62
7 Arrangement of Panels Used for FLEXSTAB Analysis of Arrow-Wing-Body Configuration	63
8 Load Distributions on the Arrow-Wing-Body Configuration—FLEXSTAB Versus Experiment	64
9 Theoretical and Experimental Chordwise Load Distributions for a Full-Span Flap Deflected by $\delta = 10$ Deg at $\alpha = 0$ Deg and $M = 0.21$	65
10 Theoretical and Experimental Load Distributions for Partial-Span Flap Deflected by $\delta = 10$ Deg at $\alpha = 0$ Deg and $M = 0.60$	66
11 Comparison of Measured and Calculated Static Hinge-Moment Coefficients	67
12 Potential-Flow Regions	68
13 Internal Vortex Strength	69
14 Outboard Boeing 747 Wing Pressure Distributions for Two Aileron-Tab Configurations	70
15 Source-Panel and Internal Vortex Arrangement on NASA Model Wing With Deflected Flap	71
16 Spanwise Load Distribution on NASA Model Wing	72
17 Comparison of Theoretical Force and Moment Results With Experimental Data on NASA Model Wing	73
18 Comparison of Theoretical and Experimental Pressure Distributions on NASA Model Wing	74

LIST OF ILLUSTRATIONS (Continued)

Figure	Page
19 Arrangement of Panels Used for TEA 230 Analysis of Arrow-Wing-Body Configuration	75
20 Load Distributions on the Arrow-Wing-Body Configuration--TEA 230, FLEXSTAB Versus Experiment	76
21 A 35-Deg Sweptback Wing With Control Surface	77
22 Theoretical Lift Distributions on NASA Wing	78
23 Graphic Illustration of Equation (54)	79
24 Planform Breakpoints	80
25 Load and Downwash Distributions on YF-16 Wing With Control Surface	81
26 Load and Downwash Distributions on a 35-Deg Sweptback Wing With Control Surface	82
27 Theoretical and Experimental Pressure Distributions for Partial-Span Flap Deflected by $\delta = 10$ Deg at $\alpha = 0$ Deg and $M = 0.60$	83
28 Comparison of Experimental and Calculated Lifting Pressure Distributions on a Sweptwing With Partial-Span Flap at $M = 0.60$	84

LIST OF TABLES

Table	Page
1 SD&SS Runs for Correlation and Hinge-Moment Improvement (Item 2.0)	85
2 Antisymmetric Stability and Control Derivatives, Comparison of FLEXSTAB and Wind Tunnel Data (from Ref. 4), Basic Paneled Model	86
3 Comparison of Hinge-Moment Derivatives -- AFFDL and Boeing, Basic Paneled Model.	87
4 Comparison of Boeing and AFFDL Flaperon Hinge-Moment Derivatives Using the Near-Field/Far-Field Option (Low-Density Paneling) on the Basic Model, Rigid Airplane	90
5 Comparison of Flaperon Hinge-Moment Derivatives of Basic Paneled Model With Incorrect and Correct Hinge Lines, Rigid Airplane	91
6 Comparison of Hinge-Moment Derivatives for Various Paneling Configurations	92
7 Comparison of (Boeing) FLEXSTAB Derived Hinge Moments $C_{h\alpha}$, $C_{h\delta}^S$, and $C_{h\delta}^A$ With Wind Tunnel and Simulation Data, Rigid Airplane	95
8 Methodologies of Potential-Flow Programs	96

ABBREVIATIONS AND SYMBOLS

a	Lift-curve slope (eq. (4))
[a,b]	Interval of integration (eq. (53))
[AIC]	Aerodynamic influence coefficient matrix (eq. (5))
a_k	Coefficient (eq. (57))
a_{mn}	Coefficients (eq. (28))
$[A_{p\theta}]$	Reduced [LSC] matrix (eq. (9))
AR	Aspect ratio
b	Span (eq. (28))
B_2	Defined in figure 6.1.6.1-19c of reference 10
c	Chord; constant (eq. (50))
C_h	Hinge-moment coefficient
C_l	Section lift coefficient
C_L	Lift coefficient
C_p	Pressure coefficient
$[CPM^V], [CPM^{CS}], [CPM^{LS}]$	Pressure influence coefficient matrices (eqs. (6), (8))
d	Moment arm (eq. (13))
$\frac{D}{Dt}$	Total derivative operator
E_n	Error (eq. (54))
f, g	Trigonometric functions (eq. (28))
g_k	Loading function (eq. (57))
H_j	Weight coefficient (eq. (54))
HM	Hinge moment
i_t	Tail angle (eq. (4))
K	Kernel function
K_α, K_δ	Defined in equations (6.1.6.1-b) and (6.1.6.2-b) of reference 10
L_j	Interpolation function (eq. (60))
[LSC]	Lift strength coefficient matrix (eq. (7))
M	Mach number
MIC_{ik}	Mode influence coefficient (eq. (59))
n	Normal vector (eq. (33))
N	Mode shape (eq. (26))
\hat{p}	Nondimensional rolling rate
q	Generalized coordinate (eq. (26))

\hat{q}	Nondimensional pitching rate
\bar{q}_1	Dynamic pressure at steady reference-flight condition
r	Distance between two points (eq. (33))
\hat{r}	Nondimensional yawing rate
R	Square error (eqs. (46), (49))
Re	Reynolds number
S	Surface area
$[S^V], [S^{CS}], [S^{LS}]$	Singularity strengths (eqs. (5), (8))
t	Tangent vectors (eqs. (44), (51))
$[TD]$	Thickness influence coefficient matrix (eq. (11))
$[T_{FP}]$	Matrix containing area factors (eq. (13))
(U, V, W)	Velocity components
W_k	Weight coefficient (eqs. (46), (49))
(x, y, z)	Coordinate system

GREEK

α	Angle of attack
α_δ	Lift-effectiveness parameter (eqs. (23), (24))
β	Sideslip angle; right-hand side of boundary condition (eq. (39))
γ	Vorticity
δ	Control-surface deflection angle
ϵ	Tail downwash (eq. (4))
η	Nondimensional span location ($\equiv \frac{2y}{b}$)
λ	Singularity strength (eq. (39))
Λ	Sweep angle (eq. (19))
μ	Viscosity; doublet strength (eq. (38))
(ξ, η, ζ)	Coordinate system
ρ	Density
σ	Source strength (eq. (38))
τ	Thickness ratio (eq. (16))
ϕ	Trailing-edge angle (eq. (16)); potential (eq. (33))
ψ	Flow incidence (eqs. (5), (10), (14))

SUBSCRIPTS

AE	Asymptotic expansion
c	Control surface
LE	Leading edge
o	Reference
t	Tail
TE	Trailing edge
w	Wake

SUPERSCRIPTS

A	Antisymmetric
CS	Constant source
LS	Linear source
S	Symmetric
v	Vorticity
(\cdot)	Nondimensional time derivative

SECTION I

INTRODUCTION

The purpose of the work documented in this report is to improve the accuracy of aerodynamic hinge-moment analysis. When addressing this subject, one is primarily concerned with the flow over--and the pressure, force, and moment experienced by--the nonplanar, multiple lifting surfaces. When the control surface is deflected, the pressure distribution on the lifting surface is significantly altered by the presence of the discontinuous kinematic downwash field. Associated with the change of geometry are such phenomena as boundary-layer separation, free vortex flow, and thick wake. In the transonic flow regime, the shocks lie partway back on the lifting surfaces and interact with the boundary layer, which makes the problem highly nonlinear. Attention to these phenomena would necessitate a long-term study and an evaluation of each individual effect. Indeed, the prediction of the hinge moment is a complicated subject. In view of the current status of the theoretical development and the numerical schemes in various aspects of computational aerodynamics, one might want to place reliance for such information on measurements by wind tunnel or other experimental means when available.

In the development of highly maneuverable aircraft, the accuracy of hinge-moment prediction is important with respect to the vehicle stability and controllability. To design such aircraft certainly calls for a more efficient tool using the product of theoretical aerodynamics instead of relying solely on measurements. The bulk of this study is to review and exemplify several of the existing methods for analyzing the aerodynamic loadings on the control surfaces, among which one is of semiempirical nature.

The first part of this work (sec. II) is concerned with reviewing the formulation and coding of the hinge-moment subprogram in FLEXSTAB. Aerodynamic hinge-moment derivatives have previously been computed using the FLEXSTAB programs. References 1 and 2 present results for the YF-16 and B-52E aircraft, respectively. The YF-16 analysis was conducted by the AFFDL and the B-52E analysis was completed by Boeing. An objective of the present study is to review the work of reference 1 and to improve the accuracy of hinge-moment prediction.

Hinge moments were obtained by Boeing for the YF-16 Government-furnished geometry model. The effect of airplane flexibility on hinge moments was investigated using AFFDL-supplied NASTAP data. The near-field/far-field option was applied to the control surfaces. The results of these analyses were compared with those reported in reference 1. To investigate the effect of paneling on hinge moments, the YF-16 was analyzed with various paneling configurations and the results correlated with the Government-furnished hinge-moment data.

The second part of the work (sec. III) is to review and discuss the theoretical and numerical characteristics of several aerodynamic methods relating to the load prediction on the lifting surfaces. These methods include FLEXSTAB, Datcom, RHO 4, TEA 230, and the PAN AIR pilot code. The discussions are focused on the behavior of their steady, subsonic solutions in regions of singularity, namely at the control-surface hinge line and side edges, and at planform breaks that exhibit discontinuities in surface slope, planform shape, dihedral, etc.

Recommendations are made in sections IV and V to improve the aerodynamic methods for better prediction of the load distributions on the control surfaces. A solution procedure that combines the merits of panel and kernel function methods is proposed as an effective scheme to predict the loading on a control surface with nonseparated flow.

Conclusions are presented in section VI.

SECTION II

FLEXSTAB PROGRAM REVIEW AND DEMONSTRATION

2.1 HINGE-MOMENT FORMULATION AND CODE

The hinge-moment theory, as derived by Boeing, was reviewed and judged essentially correct in the context of the aerodynamic theory as used in FLEXSTAB (ref. 3, vol. I). The code and flow charts were also checked. The code was found to describe the theory properly; however, a few minor improvements and corrections, as reported in monthly progress report No. 2 (31 May 1977) submitted to AFFDL, are required at the printout level. A large number of errors were found in the hinge-moment program flow charts (ref. 3, vol. III) and therefore were corrected to represent the coding.

2.2 HINGE-MOMENT ANALYSIS FOR YF-16

The initial aim of the analysis was to rerun the AFFDL data at Boeing to establish a baseline to compare the AFFDL results with the Boeing results. This comparison consisted of analyzing the basic paneled model with the residual elastic option at sea level and 15,000 ft. A further comparison was made with the near-field/far-field option (with low-density paneling) applied to the rigid model. (For a description of the near-field/far-field option, see sec. 3.1.3.) These correlation runs are listed as SD&SS runs 1 through 3 in table 1.

Having established a correlation of analyses between AFFDL and Boeing for the basic airplane, the balance of the analyses was devoted to investigating modified paneling configurations and to the further application of the near-field/far-field option.

These modified paneling configurations are listed as SD&SS runs 4 through 8 in table 1. Each successive paneling configuration was based on the experience obtained from the previous model, with the objective being to improve both the hinge moments and airplane derivatives.

2.2.1 Comparison of AFFDL and Boeing Results for Basic Paneled Model

The basic paneled model analyzed by the AFFDL is shown in figure 1. This model was used to compare directly the AFFDL and Boeing results.

To check the quality of the basic model, the antisymmetric stability and control derivatives for both the rigid and flexible airplane as obtained by the Boeing/AFFDL FLEXSTAB analyses were compared (table 2) with wind-tunnel data obtained from reference 4.

Table 3 compares the hinge moments for the flaperon, horizontal tail, and rudder obtained by the AFFDL and Boeing analyses for the rigid airplane and the flexible airplane at sea level and 15,000 ft. For the rigid airplane the results (except for a few minor discrepancies) are in agreement. However, large differences are apparent in the comparison of the hinge-moment derivatives for the flexible airplane both at sea level and at 15,000 ft. The rudder hinge-moment derivatives show the smallest differences between the Boeing and AFFDL results. The reasons for these differences are not known, but they could be due to using a different NASTAP or a different version of ESIC.

Table 4 compares the AFFDL and Boeing flaperon hinge-moment derivatives using the near-field/far-field option. The low-density paneling case was compared for the flaperon only because it was evident from the AFFDL results that while the basic flaperon hinge-moment derivatives C_{h_α} , $C_{h_\delta}^S$, and $C_{h_\delta}^A$ compared poorly with wind-tunnel data, application of the near-field/far-field option considerably improved them as compared to the wind-tunnel data.

While the basic flaperon hinge-moment results between AFFDL and Boeing correlated well, as noted above, this is not the case when using the near-field/far-field option. The Boeing near-field/far-field results are more commensurate with the basic results (as is to be expected) than are the AFFDL results and generally show much smaller changes.

Because AFFDL applied the near-field/far-field option to all the control surfaces while Boeing applied it to the flaperon only, there are a different number of thin bodies and panels involved. Also, it is concluded that there are some coding errors in the option; this may explain the differences in the results.

2.2.2 Investigation of Other Paneling Configurations

Having completed the comparison runs with the basic AFFDL paneling, alternative configurations were investigated; however, while this work was in progress, it was discovered that there was an error in the hinge-line definition of the flaperon in the AFFDL input data. Although the x-coordinates describing the hinge line were correct, the y-coordinates were displaced inboard, which resulted in the flaperon hinge line being further aft than the correct position. This error is the direct cause of the flaperon hinge moments being so small compared to the wind-tunnel data. As shown in table 5, correction of the hinge line greatly improves the flaperon hinge moments.

By the same argument the horizontal-tail hinge moments could be improved since, compared with wind tunnel data, $+C_{h_\alpha}$ is too large and $-C_{h_\delta}$ is too small. It is evident that by redefining the horizontal-tail hinge line a little further forward, $+C_{h_\alpha}$ would be reduced and $-C_{h_\delta}$ increased.

Table 6 compares the hinge-moment derivatives obtained from the various paneling configurations investigated. In each case the flaperon hinge line is in the correct location. In table 6 the first model is the basic paneled model with the corrected flaperon hinge line (fig. 1).

The second model has the same paneling as the basic model except that the innermost row of panels along the interference body has been incorporated into one thin body called STRAKE. Previously the forward panels were part of the wing and the aft panels comprised a thin body called IHTAIL. In general, it is better to have adjacent thin bodies in contact along chordwise lines rather than spanwise lines, although this is more important when leading-edge thrust or thickness is being considered.

The third column of table 6 lists the hinge-moment derivatives for the basic paneled model with the low-density near-field/far-field option applied to the flaperon only. The flaperon hinge moments $C_{h\delta}^S$ and $C_{h\delta}^A$ and, especially, $C_{h\alpha}$ are improved over the corresponding hinge moments of the basic paneled model when compared with the wind-tunnel data in table 7.

The fourth column of table 6 lists the hinge-moment derivatives for the model that was paneled to simulate the low-density near-field/far-field model (fig. 2). This model gives, in general, no better results than the basic model while being much more expensive (293 versus 254 singularities).

The fifth column contains the hinge-moment derivatives for an "improved" paneled model (fig. 3). The paneling for this model is changed from the basic in the following ways:

- 1) The wing panels are denser both spanwise and chordwise so that the disparity in size between the panels just ahead of the flaperon hinge line and those just behind is reduced.
- 2) The triangular panels in the basic model (believed not to be good from a numerical point of view) are removed and the fine paneling on the flaperon is continued across the interference body.
- 3) The horizontal-tail paneling is changed in order that the streamwise panel intersections continue to line up with those on the wing. The paneling on the interference body is lined up with that on the horizontal tail.
- 4) The final row of panels on the interference body is removed in order partially to represent the gaps between the empennage and the fuselage.
- 5) The fin and rudder paneling is left unchanged since the rudder hinge-moment results are good.

In spite of these various modifications and a further increase in the number of singularities (299) over the low-density simulation (293), comparison to wind-tunnel data shows that the hinge moments are not improved correspondingly.

SECTION III

REVIEW AND DISCUSSION OF EXISTING HINGE-MOMENT ANALYSIS METHODS

In view of the complexity of the subject, the discussion here is limited to longitudinal control in the subsonic flight regime. The general discussion, however, can be extended to lateral-directional control and to the supersonic flight regime where applicable. The control devices include various types of flaps and slats, such as plain or split flaps, single- or double-slotted flaps, Fowler flaps, leading-edge flaps, and slats. Complicating the analysis of hinge moments are geometric arrangements such as basic airfoil characteristics, trailing-edge bluntness and angle, gap size and geometry, nose shape, and balance ratio. Except for very small angles of attack and control deflections, the hinge moments are basically nonlinear. At larger angles, the flow is bound to separate on the upper surface of the trailing-edge control surface and hence is characterized by the boundary-layer formulation. All of these factors make the prediction of the hinge moment extremely difficult.

A typical longitudinal control may be provided by deflecting the elevator, which may be all or part of the tail, or a trailing-edge flap in a tailless design. In addition, a tab may also be mounted on the elevator or flap. For small control deflections, δ , as is usually stipulated, one may assume that the hinge moment, C_h , is linear in the control deflection such that

$$C_h = C_h(\alpha, \hat{q}) + C_{h\delta} \delta \quad (1)$$

where $C_h(\alpha, \hat{q})$ is the basic hinge moment when $\delta = 0$ and $C_{h\delta} = \frac{\partial C_h}{\partial \delta}$. In the case of small angle of attack, α , and pitch rate, \hat{q} , the linear relation holds among the hinge moment, the pitch rate, and the angle of attack of the surface that contains the control surface. Then,

$$C_h = C_{h_0} + \frac{\partial C_h}{\partial \alpha} \alpha + C_{h\hat{q}} \hat{q} + C_{h\delta} \delta \quad (2)$$

In terms of the angle of attack, α , we have

$$C_h = C_{h_0} + C_{h\alpha} \alpha + C_{h\hat{q}} \hat{q} + C_{h\delta} \delta \quad (3)$$

where the coefficients are related through tail downwash, etc. (ref. 5), as

$$C_{h_o} = C_{h_o}' + \frac{\partial C_h}{\partial \alpha_s} (i_t - \epsilon_o) \left[1 - \frac{a_t}{a} \frac{S_t}{S} \left(1 - \frac{\partial \epsilon}{\partial \alpha'} \right) \right]$$

$$C_{h_\alpha} = \frac{\partial C_h}{\partial \alpha_s} \left(1 - \frac{\partial \epsilon}{\partial \alpha'} \right) \quad (4)$$

Hence, for the range where linearity holds, the calculation of hinge moments reduces to the evaluation of C_{h_o} , C_{h_α} , $C_{h_{\dot{q}}}$, and C_{h_δ} separately. Basically, C_{h_o} is the camber effect; C_{h_α} and $C_{h_{\dot{q}}}$ are, respectively, the hinge moments due to unit angle of attack and unit pitch rate at zero control deflection; and C_{h_δ} is the hinge moment due to unit control deflection angle with camber, angle of attack, and pitch rate set to zero. A typical load distribution on the control surface with and without deflection is shown in figure 4.

If the control surface is not deflected, the evaluation of the coefficients C_{h_o} , C_{h_α} , and $C_{h_{\dot{q}}}$ is no different from that of lift and moment of the basic airfoil for which various techniques, either analytical or experimental, are available. The prediction of C_{h_δ} , however, is quite involved. Physically, when the control surface is deflected, the geometry of the configuration becomes more complicated, either through the change in the geometry of the lifting surface or through the creation of the gap between the basic airfoil and the control surface. The actuation of the control surface also induces viscous effects that may alter the boundary layer ahead of the control-surface leading edge and, possibly, cause the flow to separate from the control surface, depending on a variety of geometric factors. Mathematically, potential-flow considerations tell us that the deflection of the control surface includes a discontinuity in the planform and/or the slope; both factors introduce singular behavior along the hinge line, the planform breaks, and the side edges. Aside from the above complications, if the flow separation does occur, as is usual on the upper surface of the trailing-edge control with moderate or higher angles, the existing analytical methods break down completely since the current theories for inviscid flow and boundary-layer flow no longer apply. Consequently, wind-tunnel tests or semiempirical methods are the last resort for hinge-moment predictions. Nevertheless, it would be more beneficial if a certain degree of confidence could be achieved through the development of capable analytical schemes.

The object of the current task is to review and discuss the theoretical and numerical characteristics of the FLEXSTAB method (ref. 3) and a few other

numerical methods, with particular emphasis on the prediction of the hinge-moment control derivative, $C_{h\delta}$.

3.1 FLEXSTAB METHOD

The FLEXSTAB method for predicting stability characteristics of the airplane is based on the numerical scheme developed by Woodward (refs. 6, 7, 8). The governing flow equation is the linearized potential flow with boundary conditions satisfied on the mean surfaces; i.e., in a linearized sense. Numerically, the resulting finite set of integral equations, which correspond to a set of boundary conditions applied at finite points, is reduced to a system of linear algebraic equations with coefficients called the "aerodynamic influence coefficients" (AIC). The solutions of the linearized boundary-value problem are given in terms of perturbation velocities and pressure coefficients, from which the forces, moments, and stability parameters are consequently derived. A brief description of the aerodynamics in the FLEXSTAB system is given below, followed by the hinge-moment calculations and the discussion of the numerical characteristics of the solutions.

3.1.1 Aerodynamics in the FLEXSTAB System

In the FLEXSTAB system, the components in a general airplane configuration are categorized as either thin bodies (wing, tail, strut, pylon) or slender bodies (fuselage, nacelle, external storage). Still another category of imaginary bodies, called interference bodies, is needed to serve as the medium of interference between the thin bodies and the slender bodies.

Since both the flow equation and the boundary condition are linearized, the principle of superposition applies. Thus, for a body having camber and thickness, the total effect can be considered as the sum of the individual effects of camber alone and thickness. Each individual effect is described below.

Thin-Body Lifting Problem--It is known that the lift is associated with flow circulation, which can be realized on a sheet of vorticity. The lift of a thin body is simulated by placing horseshoe vortices on the mean camber surface. The distribution of the vortices is made simpler by dividing the mean surface into quadrilateral panels with the vorticity strength on each panel specified as a constant. The boundary condition on the solid surface is such that the cumulative velocity normal to the surface is identical to the

kinematic downwash ψ on the boundary point (control point) of the surface. Mathematically, the vorticity strength S^V on each panel is determined from the equation

$$\{\psi\} = [AIC] \{S^V\} \quad (5)$$

where each element of the [AIC] matrix, the aerodynamic influence coefficient, is precisely the normal component of the perturbation velocity induced by a vortex panel of unit strength. Since the lifting pressure is directly related to the circulation or the vortex strength, the lifting pressure at each panel centroid location is calculated as

$$\{C_p\} = [CPM^V] \{S^V\} \quad (6)$$

where $[CPM^V]$ is a diagonal matrix with each element equal to 2. When substituting equation (5), the lifting pressure is seen to be related to the boundary condition as

$$\{C_p\} = [LSC] \{\psi\} \quad (7)$$

where

$$[LSC] = [CPM^V] [AIC]^{-1}$$

Thin-Body Thickness Problem--Since the combination of sources with a uniform freestream yields stream surfaces that resemble solid surfaces, the thickness effect of thin bodies is simulated by replacing the vortex singularity distribution in the lifting problem by source singularities. The thickness pressure on the thin body can be calculated without solving the boundary-value problem since the source strength is known to be proportional to the surface slope which has been specified. In the FLEXSTAB system, the source distribution on each panel is either constant (CS) (for $M > 1$) or linear (LS) (for $M < 1$). In general, we have

$$\{C_p^S\} = [CPM^{CS}] \{S^{CS}\} + [CPM^{LS}] \{S^{LS}\} \quad (8)$$

where each element of the $[CPM^S]$ matrices is related to the U-component of the perturbation velocity induced by source singularity distributions (constant or linear) of unit strength.

Slender-Body Thickness Problem--In a manner similar to the modeling of the thin-body thickness, the slender-body thickness can be simulated by distributing source singularity on the mean centerline. To simplify the numerical

procedures, a slender body is divided transversely into many segments. The constant-strength line source is used in subsonic flow and the linearly varying line source is used in supersonic flow. At a boundary point of each slender-body segment, the flow tangency condition is imposed. The source strength is derived from the tangency condition, and the pressure due to thickness effect is computed as in equation (8). Since the flow property is symmetric with respect to the mean centerline axis, this problem is also referred to as the axial flow problem.

Slender-Body Lifting Problem--For a cambered slender body or a slender body subject to angle of attack or sideslip, a lifting force or side force can be developed. Both phenomena are referred to as the crossflow problem. It is known that the derivative of the axial flow potential with respect to the radial coordinate identically satisfies the crossflow equation. The lift on a slender body is simulated by replacing the line source distribution in the thickness problem by the line doublet distribution, as the doublet potential is derived from the source potential by differentiation. The doublet singularity can be quadratically distributed (for $M > 1$) or even splined over three centerline segments (for $M \cdot 1$). The strength of the line doublet singularity on each centerline segment is constrained by the boundary condition imposed at a certain point on the mean centerline of the slender body. The resultant lifting pressure on each segment can be expressed similarly to equation (7), with the reference areas properly accounted for.

Multiple-Body Interference Problem--If there are more than one body, either of the same or different category, in the same flow field, interference effects take place between the bodies. These interference effects must be separately accounted for and then combined with the results of the solutions due to isolated bodies. The mutual interference among bodies can be illustrated by a simple wing-body configuration. The effect of the camber and incidence of the body on the wing is expressed in terms of extra downwash on the mean wing surface induced by doublet singularity on the body. On the other hand, the presence of the camber and the incidence on the wing also affect the body. However, this influence is only indirect; i.e., it is expressed as the downwash on an imaginary shield--the interference body--that wraps around the slender body. The extra downwash on the interference body is canceled by the normal velocity induced by singularities distributed on the interference-body panels.

These panels are vortex panels, as are those on the thin bodies. The resultant pressure on the interference body is then transferred to the slender body with which it is associated. In general, the pressure on the slender-body segments and interference-body and thin-body panels can be expressed as:

$$\{C_p\} = [A_{p0}] \{\psi\} \quad (9)$$

where $\{\psi\}$ includes incidence and camber on slender-body centerline segments and thin-body panels, while $[A_{p0}]$ contains the ensemble of $[LSC]$ for each body, with the columns corresponding to interference-body panels deleted. The contribution of thickness to the lift (buoyancy force) can likewise be included as

$$\{C_p^V\}^{int} = [LSC] \{\psi^S\}^{int} \quad (10)$$

where $\{\psi^S\}^{int}$ is the negative of the flow incidence on interference-body and thin-body panels due to source singularities that are employed to simulate the volume of the wing and the body, i.e.,

$$\{\psi^S\}^{int} = [TD] \{S^S\} \quad (11)$$

with $[TD]$ being the thickness downwash matrix. The resulting pressure, which includes the thickness effect, is then

$$\{C_p\} = [A_{p0}] \{\psi\} - \{C_p^V\}^{int} \quad (12)$$

3.1.2 Computation of Hinge Moment

The lifting pressure given in equation (12) contains the loading on the control surface, which is part of the thin body. The hinge-moment coefficient is computed as

$$\begin{aligned} C_h &= \frac{1}{S_c C_c} \sum_i d_{c_i} S_i \Delta C_{p_i} \\ &= \frac{1}{S_c C_c} [d_c] [T_{FP}] \{[A_{p0}] \{\psi\} - \{C_p^V\}^{int}\} \end{aligned} \quad (13)$$

where the nonzero elements of $[d_c]$ are the distances from the centroid of the control surface panels to the hinge line. The elements in $[T_{FP}]$ are the areas of control surface panels, and S_c and C_c are, respectively, the reference area and length for the hinge-moment coefficient.

Note that the incidence vector $\{\psi\}$ consists of the effects due to camber and control-surface deflections as well as various motion variables, such as

angle of attack, sideslip, pitching, rolling, and yawing velocities. Since only a linear relationship is considered, we have

$$\begin{aligned} \{\psi\} = & \{\psi_c\} + \{\psi_\delta\} \delta + \{\psi_\alpha\} \alpha + \{\psi_\beta\} \beta \\ & + \{\psi_p\} \hat{p} + \{\psi_Q\} \hat{q} + \{\psi_R\} \hat{r} \end{aligned} \quad (14)$$

For longitudinal motion, only the incidences due to camber, angle of attack α , pitch rate \hat{q} , and the elevator type of the control deflection δ are considered. With equation (14) in mind, the hinge-moment derivatives for longitudinal motion can be obtained from equation (13) as

$$\begin{aligned} C_{h_0} &= \frac{1}{S_c C_c} [d_c] [T_{FP}] \{[\Lambda_{p_0}] \{\psi_c\} - \{C_p^V\}^{int}\} \\ C_{h_\alpha} &= \frac{1}{S_c C_c} [d_c] [T_{FP}] [\Lambda_{p_0}] \{\psi_\alpha\} \\ C_{h_{\hat{q}}} &= \frac{1}{S_c C_c} [d_c] [T_{FP}] [\Lambda_{p_0}] \{\psi_Q\} \\ C_{h_\delta} &= \frac{1}{S_c C_c} [d_c] [T_{FP}] [\Lambda_{p_0}] \{\psi_\delta\} \end{aligned} \quad (15)$$

3.1.3 Discussion of Numerical Characteristics

Without elaborating on the limitations that are imposed on the potential flow solutions, it should be noted that the linearization of the flow equation and boundary condition takes on different forms that vary from one panel method to another. In the FLEXSTAB analysis, the aerodynamic representation is such that the boundary condition is also applied in a linearized sense; i.e., the boundary condition is satisfied only on the mean surface rather than the actual configuration surface. Although the approximation of the boundary condition is fully consistent with the linearized theory, it does impose a severe restriction on the control-surface deflection as far as the computation of the hinge moment is concerned. Thus, the vortex singularities used to simulate the lift on the control surface are placed on a mean surface as if the control surface were not deflected, and the boundary condition is also applied at the mean surface, with the tangency condition (local incidence) evaluated at the deflected configuration. Furthermore, the FLEXSTAB analysis employs the velocity condition, while in the linearized theory it has been shown that it is the mass flux, instead of the velocity boundary condition, that satisfies the flow equation. That is to say, the tangency condition implies that the mass flux is tangent to the configuration surface. The perturbation mass flux differs from the perturbation velocity in the component

lying in the compressibility axis direction in which the mass flux component is equal to the velocity components multiplied by a factor $(1 - M^2)$.

Although the interference effect between all aerodynamic components has been accounted for in the manner inherent in equation (9), the role of the thickness only manifests itself as the effect of buoyancy. Consequently, the thickness of an isolated airfoil, in particular the trailing-edge angle of the control surface, has no effect on either the loading distribution in equation (12) or the hinge moment and its derivatives in equations (13) and (15) since $\{C_p^V\}^{int}$ in equation (10) is identically zero. It is known, however, that both the control-surface leading-edge bluntness and the trailing-edge angle are crucial in the hinge-moment calculation. The information on the thickness of the airfoil is lost through the assumption that, in the linearized theory, the flow problem can be separated into the symmetric problem due to thickness and the antisymmetric problem due to angle of attack and camber. Because of the symmetry of the thickness problem, the thickness of the airfoil produces no net effect on the loading. Thus, a FLEXSTAB analysis concerning hinge moments is further limited to very thin wings unless it is corrected by the local effect due to thickness, such as the correction on the local velocity induced by the thickness of the airfoil. Since the lift is associated with circulation, and hence the vorticity, the constant-vortex panel implies a constant-pressure panel. In the linearized theory, the singular behavior of the flow is realized in the areas close to a subsonic leading edge, planform breaks, control-surface hinge lines, and side edges. The resultant loading in these regions, therefore, exhibits a large gradient in a certain direction. The effort to simulate this type of loading with constant-pressure panels is rather stringent. An obvious way to achieve accuracy in the solution is to increase the density of the panels in the region of the leading edge and planform breaks, and on control surfaces. This may not be a good practice from an economics viewpoint and because of the core limitation of the computer. Thus, a better paneling scheme must be sought to yield a loading distribution with a certain accuracy. The panel scheme should be intimately related to the planform geometry and the kinematic downwash distribution. One cannot overemphasize the significance of the solution near the planform breaks, hinge line, etc. However, a poor algorithm concerned with planform breaks has been built into the FLEXSTAB program. If a stream-wise panel row spans either a leading- or trailing-edge breakpoint in the

planform, the breakpoint edge is automatically redefined by connecting the row and planform edge intersections with a straight line (fig. 5). The singular behavior of the solution near the original breakpoint is therefore smeared and relocated to the neighboring regions. The result of this practice will incur more errors.

An alternative method for computing the aerodynamic influence coefficients in the regions of control surfaces, wingtips, wing-body intersections, etc., has been provided in the FLEXSTAB program. This method is the near-field/far-field option, which has been applied to analyze the hinge moment for the YF-16 airplane in section II. This method presumably yields more accurate results in the region where the loading is changing rapidly; however, it has had very little evaluation and is basically unproven. The mechanism of this method is described as follows. A near-field region may encompass a few panels. Each panel in the region is equally subdivided into many near-field panels. The downwash-singularity strength relationship is still described as in equation (5), except that the incidence on the control point of each sub-panel is set equal to that on the control point of the far-field panel, which has been subdivided. Since each near-field region has been isolated from the global region, the singularity distribution and, hence, the loading on the region are identically the same as produced by an isolated wing. The diagonal elements of the aerodynamic influence coefficients based on the near-field calculation are then equivalent to those that would yield the average loading over the near-field region as an isolated wing. As an illustration, we assign a single panel in a many-panel wing as a near-field region and then find the aerodynamic influence coefficient using the near-field method. Suppose we properly subdivide this panel into 10 panel rows and 5 panel columns and then compute the near-field aerodynamic influence coefficient matrix of size 50 by 50. The singularity strengths and hence the lifting pressure on each subpanel will then resemble the loading distribution on the panel as an isolated wing corresponding to the flow incidence ψ . A typical chordwise load distribution of a lifting surface in subsonic flow is depicted in figure 6(a). The method states that the aerodynamic influence coefficient of this panel based on the near-field calculation is proportional to the incidence divided by the average loading of this isolated panel wing,

$$-\psi \left[\frac{1}{\Delta x} \int \Delta C_p \cdot dx \right]^{-1} = -\psi / \Delta \bar{C}_p$$

On the other hand, the chordwise and spanwise downwash distributions induced by a constant-pressure panel are shown in figures 6(b) and 6(c), respectively. The usual aerodynamic influence coefficient in the far-field sense is the downwash evaluated at the control point of the panel. Whether the near-field/far-field method can yield a more accurate result is still an open question, as is the optimum location of the control point in the panel method.

Finally, this section concludes with numerical results generated by the FLEXSTAB program and comparisons with test data. The test model is an arrow-wing wing-body combination provided with leading- and trailing-edge flaps. The arrangement of panels used for the subsonic flow analysis is shown in figure 7. The chordwise pressure distributions at three spanwise stations on the wing with the full-span trailing edge deflected are shown in figure 8. Also included in figure 8 are the wind-tunnel data given in reference 9. By comparison, the FLEXSTAB method is shown to be capable of predicting the overall trend of the loading distribution qualitatively. However, in this case at least, the predictions are quantitatively poor near the hinge line, even at the inboard sections of this highly swept, low-aspect-ratio wing.

3.2 DATCOM METHODS

The Datcom (Data Compendium) methods of aerodynamic stability and control (ref. 10) as compiled by the USAF are basically semiempirical. This is the only reference included for the discussion of semiempirical hinge-moment calculations. The Datcom methods for computing hinge-moment derivatives are limited to small angles so that flow separation does not take place. Under such restrictions, the hinge moments are expected to be linear. Additional parameters that constrain the solution to the linear range of the hinge moments are the trailing-edge angles, the airfoil thickness ratios, the nose shape, and the balance ratio. The effects of seals and gaps are important for either plain or balanced controls, since the pressure distribution changes according to whether the gap is sealed or unsealed. Additional factors such as type and/or location of the seal, the nose shape, balancing, and the basic airfoil shape must also be considered. The Datcom methods, however, do not account for unsealed gaps.

The hinge-moment derivatives discussed in the Datcom methods are $C_{h\alpha}$ and $C_{h\delta}$. For either case, the section derivatives are given first, based on

the lifting-line theory. The hinge-moment derivatives are then computed from section characteristics, using a lifting-surface correction to account for sweep and aspect ratio. The Mach-number effect is accounted for by using the Prandtl-Glauert rule. Hence the Datcom methods are suitable only for higher aspect-ratio wings and lower Mach numbers. They do not provide the detail required for the load distributions on control surfaces. In this section, an excerpt is given from Datcom concerning the calculations of hinge-moment derivatives. This is followed by an analysis of the hinge-moment derivatives, C_{h_α} and C_{h_δ} , for the YF-16 wing configuration using the Datcom methods, and a discussion of the methods in general.

3.2.1 Method of Computing Hinge-Moment Derivative C_{h_α}

The semiempirical method of Datcom for evaluating section hinge-moment derivative C_{h_α} applies only to sealed trailing-edge control surfaces in the linear moment range. This derivative is computed as

$$C_{h_\alpha} = \left[\frac{C_{h_\alpha}}{(C_{h_\alpha})_{\text{theory}}} \right] (C_{h_\alpha})_{\text{theory}} + 2 (C_{\ell_\alpha})_{\text{theory}} \left[1 - \frac{C_{\ell_\alpha}}{(C_{\ell_\alpha})_{\text{theory}}} \right] \left(\tan \frac{\phi}{2} - \tau \right) \quad (16)$$

where $C_{h_\alpha}/(C_{h_\alpha})_{\text{theory}}$ and $C_{\ell_\alpha}/(C_{\ell_\alpha})_{\text{theory}}$ are empirical. The second term accounts for the thickness distribution, with ϕ being the trailing-edge angle and τ the thickness ratio.

The nose shape and the nose-balance effects are given by another empirical relation as

$$(C_{h_\alpha})_{\text{balance}} = C_{h_\alpha} \left[\frac{(C_{h_\alpha})_{\text{balance}}}{C_{h_\alpha}} \right] \quad (17)$$

and the compressibility effect is included via the Prandtl-Glauert rule

$$(C_{h_\alpha})_M = \frac{(C_{h_\alpha})_{\text{low-speed}}}{\sqrt{1 - M^2}} \quad (18)$$

This section hinge-moment derivative is then used to compute the hinge-moment derivative for an entire wing as

$$C_{h_\alpha} = \frac{AR \cos \Lambda_{C/4}}{AR + 2 \cos \Lambda_{C/4}} (C_{h_\alpha})_M + \Delta C_{h_\alpha} \quad (19)$$

where $\Delta C_{h\alpha}$ is an approximate lifting-surface correction accounting for induced camber effects.

The expression is directly applicable to control surfaces having constant chord ratios and constant airfoil sections. Otherwise, the average value of the section characteristics should be used.

3.2.2 Method of Computing Hinge-Moment Derivative $C_{h\delta}$

The Datcom method of computing $C_{h\delta}$ is very similar to that for $C_{h\alpha}$. It is also subject to the limitations as discussed for the $C_{h\alpha}$ computations.

The basic section derivative is given as

$$C_{h\delta}' = \left[\frac{C_{h\delta}'}{(C_{h\delta})_{\text{theory}}} \right] (C_{h\delta})_{\text{theory}} + 2 (C_{\ell\delta})_{\text{theory}} \left[1 - \frac{C_{\ell\delta}}{(C_{\ell\delta})_{\text{theory}}} \right] \left(\tan \frac{\phi}{2} - \tau \right) \quad (20)$$

The nose shape and the balance effects are corrected as

$$(C_{h\delta})_{\text{balance}} = C_{h\delta}' \left[\frac{(C_{h\delta})_{\text{balance}}}{C_{h\delta}'} \right] \quad (21)$$

and the compressibility is likewise included by using the Prandtl-Glauert rule.

The hinge moment is computed from the section characteristics as

$$C_{h\delta} = \cos \Lambda_{C/4} \cos \Lambda_{HL} \left[(C_{h\delta})_M + \alpha_{\delta} (C_{h\alpha})_M \frac{2 \cos \Lambda_{C/4}}{AR + 2 \cos \Lambda_{C/4}} \right] + \Delta C_{h\delta} \quad (22)$$

where α_{δ} is the two-dimensional lift-effectiveness parameter calculated either as

$$\alpha_{\delta} = - \frac{(C_{\ell\delta})_{\alpha}}{(C_{\ell\alpha})_{\delta}} \quad (23)$$

or, if experimental values of the section-lift increment ΔC_{ℓ} are available, as

$$(\alpha_{\delta})_{C_{\ell}} = - \frac{(\Delta C_{\ell})_{\text{exp}}}{(C_{\ell\alpha})_{\delta}} \quad (24)$$

3.2.3 Numerical Results for YF-16 Wing

The computations of hinge-moment derivatives for the YF-16 wing using the Datcom methods are given below.

Wing Data:

$b = 348.4$ in	$M = 0.9$
$S = 40,320$ in ²	$\bar{q}_1 = 1,201.43$ lb/ft ²
$AR = 3$	Balance ratio = 0
$C_c = 21.85$ in	$\tan \Lambda_{HL} = 0.15893$
$S_c = 4,067.6$ in ²	$\tan \Lambda_{C/4} = 0.62635$
$C_c/c = 0.191$	No thickness

From equation (6.1.3.1-a) of reference 10, we have

$$C_{h\alpha}' = \left[\frac{C_{h\alpha}'}{(C_{h\alpha})_{\text{theory}}} \right] (C_{h\alpha})_{\text{theory}} \text{ per radian}$$

Next, compute the Reynolds number,

$$\begin{aligned} \rho &= 0.00237689 \text{ slug/ft}^3 \\ U_\infty &= 1,005.4475 \text{ ft/sec} \\ c &= 131.244 \text{ in} \\ \mu &= 3.719 \times 10^{-7} \text{ slug/ft-sec} \\ \text{Re} &= \frac{\rho U_\infty c}{\mu} = 7.03 \times 10^7 \end{aligned}$$

From figure 4.1.1.2-8a of reference 10, we find

$$\frac{C_{l\alpha}}{(C_{l\alpha})_{\text{theory}}} \approx 0.96$$

Then, use figure 6.1.3.1-11a of reference 10,

$$\frac{C_{h\alpha}'}{(C_{h\alpha})_{\text{theory}}} = 0.9$$

Also from figure 6.1.3.1-11b of reference 10,

$$(C_{h\alpha})_{\text{theory}} = -0.5 \text{ per radian}$$

Thus,

$$C_{h\alpha}' = -0.45 \text{ per radian}$$

Correcting for Mach number by the Prandtl-Glauert rule, we have

$$(C_{h\alpha})_M = -1.032$$

Next apply above section characteristics to the entire wing as follows: From equation (6.1.6.1-a) of reference 10,

$$\begin{aligned} C_{h\alpha} &= \frac{AR \cos \Lambda_{C/4}}{AR + 2 \cos \Lambda_{C/4}} (C_{h\alpha})_M + \Delta C_{h\alpha} \\ &= -0.55886 + \Delta C_{h\alpha} \end{aligned}$$

Then, from figure 6.1.6.1-19a of reference 10, we find

$$\frac{\Delta C_{h\alpha}}{C_{\ell_\alpha} B_2 K_2 \cos \Lambda_{C/4}} = 0.014$$

Using figure 6.1.6.1-19c of reference 10, we have

$$B_2 = 0.92$$

From section 4.1.1.2 of reference 10, we calculate C_{ℓ_α} as

$$\begin{aligned} C_{\ell_\alpha} &= \frac{1.05}{\beta} \left[\frac{C_{\ell_\alpha}}{(C_{\ell_\alpha})_{\text{theory}}} \right] (C_{\ell_\alpha})_{\text{theory}} \\ &= 14.523 \text{ per radian} \end{aligned}$$

Next,

$$\eta_1 = \frac{y_1}{b/2} = 0.2405$$

$$\eta_0 = \frac{y_0}{b/2} = 0.775$$

From figure 6.1.6.1-19 of reference 10, we find

$$(K_\alpha)_{\eta_1} = 1.35$$

$$(K_\alpha)_{\eta_0} = 2.90$$

then, use equation (6.1.6.1-b) of reference 10,

$$K_\alpha = \frac{(K_\alpha)_{\eta_1} (1 - \eta_1) - (K_\alpha)_{\eta_0} (1 - \eta_0)}{\eta_c - \eta_1} = 0.6975$$

Finally,

$$\Delta C_{h\alpha} = 0.1106$$

Hence,

$$C_{h\alpha} = -0.55886 + 0.1106 = -0.44828 \text{ per radian}$$

On the other hand, the FLEXSTAB result for an entire YF-16 configuration is

$$HM_{\alpha} = -1,375,229 \text{ lb-in per radian}$$

or

$$C_{h\alpha} = \frac{HM_{\alpha}}{\bar{q}_1 S_c C_c} = -0.1855$$

The comparable wind-tunnel result as shown in section II (with S_c and C_c adjusted) is

$$C_{h\alpha} = -0.2127 \text{ per radian}$$

Next, from equation (6.1.3.2-a) of reference 10, the section hinge-moment derivative $C_{h\delta}$ is calculated as

$$C_{h\delta}' = \left[\frac{C_{h\delta}'}{(C_{h\delta})_{\text{theory}}} \right] (C_{h\delta})_{\text{theory}} \text{ per radian}$$

with $\frac{C_c}{C} = 0.191$ and $C_{h\alpha}/(C_{h\alpha})_{\text{theory}} = 0.96$, we find from figure 6.1.3.2-12a of reference 10,

$$\frac{C_{h\delta}'}{(C_{h\delta})_{\text{theory}}} = 0.97$$

whereas $(C_{h\delta})_{\text{theory}}$ is given by figure 6.1.3.2-12b of reference 10 as -0.92.

Thus

$$C_{h\delta}' = -0.8924 \text{ per radian}$$

At $M = 0.9$, we have

$$(C_{h\delta})_M = -2.0473$$

The hinge-moment derivative $C_{h\delta}$ for the entire wing is given in figure 6.1.6.2-a of reference 10 as

$$C_{h\delta} = \cos \Lambda_{C/4} \cos \Lambda_{HL} \left[(C_{h\delta})_M + \alpha_{\delta} (C_{h\alpha})_M \frac{2 \cos \Lambda_{C/4}}{AR + 2 \cos \Lambda_{C/4}} \right] + \Delta C_{h\delta}$$

Now, the definition of the lift-effectiveness parameter is

$$\alpha_{\delta} = -(C_{\ell_{\delta}})_{\alpha} / (C_{\ell_{\alpha}})_{\delta}$$

where $(C_{L\delta})_\alpha$ can be obtained from equation (6.1.1.1-c) of reference 10, for small flap deflection, as

$$(C_{L\delta})_\alpha = \left[\frac{C_{L\delta}}{(C_{L\delta})_{\text{theory}}} \right] (C_{L\delta})_{\text{theory}}$$

From figure 6.1.1.1-39a of reference 10,

$$(C_{L\delta})_{\text{theory}} = 3.4 \text{ per radian}$$

and from figure 6.1.1.1-39b of reference 10,

$$\frac{C_{L\delta}}{(C_{L\delta})_{\text{theory}}} = 0.93$$

then

$$(C_{L\delta})_\alpha = 3.162$$

so that

$$\alpha_\delta = -0.218$$

Thus

$$C_{h\delta} = -1.646 + \Delta C_{h\delta}$$

Now, from figure 6.1.6.2-15a of reference 10,

$$\frac{\Delta C_{h\delta}}{C_{L\delta} B_2 K_\delta \cos \Lambda_{C/4} \cos \Lambda_{HL}} = 0.025$$

where $C_{L\delta} = 3.162$, $B_2 = 0.92$, and from figure 6.1.6.2-15b of reference 10, we find

$$(K_\delta)_{\eta_1} = 1.25$$

$$(K_\delta)_{\eta_0} = 2.80$$

So that

$$K_\delta = \frac{(K_\delta)_{\eta_1} (1 - \eta_1) - (K_\delta)_{\eta_0} (1 - \eta_0)}{\eta_0 - \eta_1} = 0.5975$$

Finally,

$$\Delta C_{h\delta} = 0.036372$$

Hence the hinge-moment derivative $C_{h\delta}$ is

$$C_{h\delta} = -1.646 + 0.036372 = -1.6096 \text{ per radian}$$

The FLEXSTAB result for the entire YF-16 airplane is

$$HM_{\delta} = -598,490.2 \text{ lb-in/radian}$$

or

$$C_{h\delta} = \frac{HM_{\delta}}{q_1 S_c C_c} = -0.8075 \text{ per radian}$$

The comparable wind-tunnel result as shown in section II (with S_c and C_c adjusted) is $C_{h\delta} = -0.4592$ per radian. It is noted that both the hinge-moment derivatives $C_{h\alpha}$ and $C_{h\delta}$ computed from the Datcom methods are about twice as large as the FLEXSTAB results. No conclusion could be made since the FLEXSTAB's prediction is based on the entire YF-16 configuration. Also, the Datcom methods break down for a low-aspect-ratio wing as on the YF-16.

3.2.4 Discussion of Datcom Methods

The Datcom methods for hinge-moment calculation are restricted to a linear relationship between small angles and flow properties. The flow is also assumed to be attached and the gaps are sealed. The analysis is restricted to plain trailing-edge flap types of control surfaces. The hinge-moment derivatives are computed from the section characteristics such as the lift-effectiveness parameter α_{δ} as well as $C_{L\alpha}$, $C_{L\delta}$, $C_{h\alpha}$, and $C_{h\delta}$. Basically, the analysis employs the lifting-line theory to calculate the two-dimensional hinge-moment derivatives, with an additional lifting-surface correction to account for sweep. Consequently, the methods do not account for wing-body interference effects that may be important for inboard controls. The analysis is directly applicable to control surfaces having constant chord ratios and constant airfoil contours across the span; otherwise, the average section characteristics have to be used. It does not apply to configurations with wing cutouts or with control surfaces that do not have ends parallel to the plane of symmetry. The method does account for such factors as balance-chord ratio and shape, trailing-edge angle, and bluntness as well as the nose shape. Since the methods are based on the lifting-line theory, the calculations do not include the planform irregularities such as planform breaks where the solutions exhibit singular behavior. In summary, the semiempirical methods

of Datcom are not superior to the analytical methods so long as they offer no solution for separated flows or unsealed gaps.

3.3 RHO 4 METHOD

RHO 4 is a computer program for predicting unsteady lifting-surface loadings caused by motions of leading- and trailing-edge control surfaces having sealed gaps (refs. 11, 12, and 13). In the regions of singularities, namely at hinge lines and side edges, the discontinuities in downwash are removed and handled separately by the technique developed in references 14 and 15. The residual downwash, which is fairly smooth, is then processed using the mode-kernel function approach.

The methods of solution for steady flow are described, followed by a discussion of the numerical results.

3.3.1 Collocation Method of RHO 4

The analyses of RHO 4 are applicable to thin configurations having full-span or multiple partial-span control surfaces on the leading or trailing edge in subsonic flow. The basic flow is described by the linearized potential-flow equation. The numerical scheme of solving the flow equation can be facilitated by using the Green's function method. The resulting integral equation is of the form

$$w(x,y) = \iint \Delta C_p(\xi,\eta) K(x,y;\xi,\eta) d\xi d\eta \quad (25)$$

where $K(x,y;\xi,\eta)$ is the kernel function, which defines the downwash at the field point due to the doublet singularity on the surface point, and $\Delta C_p(\xi,\eta)$ is the lifting pressure related to singularity strength. The solution procedures differ according to the condition of the kinematic downwash distribution, described below.

Solution Procedures for Smooth Downwash Distribution--The solution of the integral equation is obtained by assuming that the deflections of the lifting surface may be represented by a finite sum of discrete mode shapes. For steady flow,

$$z = \sum_1 N_1(x,y) q_1 \quad (26)$$

where $N_1(x,y)$ is the i th mode shape and q_1 is the i th generalized coordinate. Corresponding to a particular mode, we have the lifting pressure Δp_1 , then

$$\Delta p = \sum_i (\Delta p_i) q_i \quad (27)$$

Using the relation $W = Dz/Dt$, equation (25) describes the link between the mode-shape slope and the lifting pressure of that particular mode.

The kernel function is further divided into a nonsingular part and a singular part; the latter contains the dipole, the inverse square root, and the logarithmic singularities.

Upon integration in the chordwise direction, the singularities in the integrand of the spanwise integral can be identified. In the evaluation of the spanwise portion of the downwash integral, the integration interval is divided into subregions and appropriate quadrature formulas are applied to each subregion; i.e., the square-root quadrature formula applied at the ends of the interval, the logarithmic quadrature formula applied on either side of the downwash station, and the Legendre quadrature formula applied within the remaining integration interval. Near the leading edge, an assumed pressure function that is inversely proportional to the square root of the distance from the leading edge is employed, which will provide the least error in downwash value near the leading edge. The above scheme is so implemented that the solution will not be too sensitive to the collocation stations.

The solution of the integral equation is approximated by generating a finite set of downwash distributions, the combination of which satisfies the boundary condition at a finite set of control points. Each downwash distribution is obtained by evaluating the downwash integral using assumed polynomial pressure distributions that conform to the loading condition on the planform edges. Mathematically, the loading function of the j th mode has the following form:

$$\Delta p^j(\xi, \eta) = \sqrt{(b/2)^2 - \eta^2} \sum_m \sum_n a_{mn}^{(j)} f^{(m)}(\eta) g^{(n)}(\xi, \eta) \quad (28)$$

where f and g are certain trigonometric functions and a_{mn} are the unknown coefficients to be determined from the integral equations.

Solution Procedures for Discontinuous Downwash Distributions--The above solution procedures for predicting loading over a smooth downwash field may fail to produce reasonable results when applied to configurations having discontinuous downwash, which may be caused, for instance, by control-surface deflections. The technique used to circumvent this difficulty is the introduction of the residual downwash.

The residual downwash is the difference between the kinematic downwash and the downwash produced by pressure distribution $\Delta p_{\Lambda E}$ obtained from the process of matched asymptotic expansion, which will provide the proper discontinuous downwash condition near the hinge line and the side edges of the control surfaces (refs. 14 and 15). These pressure distributions (inner solution) are valid only in the localized regions. However, they can be extended to the outer region since the distributions in the outer region may take any convenient form as long as they satisfy the required loading condition along the edge of the planform. A unique solution will be determined from the outer region at a later stage. The usual condition imposed on these loading functions is that the pressure distribution diminishes in proportion to the square root of the distance from the edges.

The residual downwash, defined as

$$W_{\text{residual}} = W_{\text{kinematic}} - \iint \Delta p_{\Lambda E}(\xi, \eta) K(x, y; \xi, \eta) d\xi d\eta \quad (29)$$

is expected to be fairly smooth and therefore is amenable to the standard lifting-surface solution process, i.e.,

$$W_{\text{residual}} = \left[\iint \Delta p_j(\xi, \eta) K(x, y; \xi, \eta) d\xi d\eta \right] q_j \quad (30)$$

After solving for Δp_j , the resultant lifting pressure becomes

$$\Delta p(\xi, \eta) = p_{\Lambda E}(\xi, \eta) + \sum_j \Delta p_j(\xi, \eta) q_j \quad (31)$$

The hinge moment can be easily calculated using the lifting pressure computed in equation (31).

3.3.2 Discussion of RHO 4 Method

The analysis in this program is based on the mode-kernel function method, which uses a predetermined polynomial type of loading distribution with coefficients determined by satisfying the kinematic downwash at certain collocation points (standard flat-plate boundary points). The method is applicable to thin lifting surfaces with twist via local linearization. The thickness effect can be included in the downwash boundary condition in terms of local streamwise velocity variations. The control surfaces are assumed to have sealed gaps, and the balance ratios are set to zero. The side edges are required to be parallel to the plane of symmetry. The control surfaces symmetrically located on the lifting surfaces are allowed to deflect either symmetrically or anti-symmetrically. The input mode shapes have to be defined.

The special feature of the RHO 4 method is the manner in which it handles the discontinuous downwash as manifested in the control-surface deflection. The downwash discontinuity is removed by using the inner solution, which provides the proper discontinuous downwash near the hinge line and side edges. The residual downwash is therefore smooth and amendable to the standard kernel procedures. These procedures allow for the accurate prediction of the singular behavior of the flow properties near the irregular regions of the planform. In particular, the method is suitable for predicting the loading distribution on the control surface and hence the hinge moment. The method, however, may still encounter numerical difficulties in the regions of planform breaks. If the downwash chord were located at, or very close to, the planform break stations, the downwash integral would exhibit singular behavior due to the oversimplified loading distributions used in solving the downwash integral. Whenever the planform breaks are present, the spanwise loading becomes discontinuous at the spanwise stations, which causes numerical problems and produces singularities in the calculated downwash sheet. Although it is suggested in the method that either the downwash chord be placed at least a small distance away from the planform break stations or the planform near the breakpoints be modified by applying a small amount of smoothing, the accuracy of the solution may be degraded. Presumably, one may include certain appropriate loading functions corresponding to the inner solutions near the planform breaks in the manner exactly parallel to that of applying the inner solution near the hinge line. Since the method deals only with the lifting surfaces, the wing-body interference effect is not included in the solution. The thickness effect, especially at the nose and the trailing edge, can enter the solution through the change of the local velocity, since the boundary condition is applied in a linearized sense.

The numerical results on the chordwise load distribution obtained by the RHO 4 method are given in figures 9 and 10 for a full-span trailing-edge control surface at $M = 0.21$ and an inboard partial-span control surface at $M = 0.60$, respectively. Both predicted results agree well with experimental data. For a delta-wing model shown in figure 11, the hinge-moment coefficients are also computed and correlate favorably with measurements for a leading-edge control and a trailing-edge control. These comparisons indicate that the pressure distributions and the hinge moments can be predicted with reasonable accuracy using the RHO 4 program, provided one is aware of the limitations of the method.

3.4 TEA 230 METHOD

The Boeing aerodynamic program TEA 230 (refs. 16 and 17) was originally developed to determine the aerodynamic characteristics of fan-in-wing configurations using the subsonic-potential-flow theory. This program is applicable to wings with deflected control surfaces and a wide variety of potential-flow boundary-value problems. Although the solution is based on the linearized potential-flow equation, the nonlinear effect has been retained through the application of the exact boundary condition. Mathematically, the potential-flow solution is obtained by reducing the problem to solving an integral equation. Numerical solution of the integral equation is facilitated by the distributions of constant-strength source sheets over the configuration surface, and distributions of vortex filaments or doublets inside the configuration surface and on the wake. The source and the doublet strengths are determined by satisfying a set of boundary conditions at finite points on the boundary surfaces. Once the singularity strengths are known, the flow-field details may be calculated. Basically, the solution for the subsonic flow is obtained in the incompressible flow domain with the effect of compressibility accounted for by means of Göthert's rule. The TEA 230 method is an extension of the vortex-lattice method and provides for aerodynamic representation of thick wing configurations. A boundary-layer theory is also included in the program with the purpose of indicating the boundary-layer conditions in the areas that are prone to flow separation.

The basic elements of the potential-flow theory as used in the program are presented in detail because they are also used in the more advanced panel methods. They are followed by the description of the numerical method and a discussion of the numerical characteristics of the solutions pertinent to the load prediction on the control surfaces.

3.4.1 Potential-Flow Theory

A flow field that is uniform in the ambient can be considered as a potential flow except in the boundary layer adjacent to the configuration surfaces, the trailing vortex sheets, the jets, etc. The potential-flow equation can be derived from the conservations of mass, momentum, and energy. The resulting equation is in general highly nonlinear. The total flow is assumed to be made up of an onset flow and a perturbation flow. The perturbation flow, due to the presence of a disturbance in the onset flow, is considered to be very

small compared to the onset flow. Therefore, the governing equation of the perturbation flow can be linearized. By using the Görtler rule, the linearized flow equation can be further reduced to the Laplace equation. This solution is already known since it also governs a wide range of problems in mathematical physics.

The boundary-value problem can be stated as follows. The perturbation potential is governed by the Laplace equation

$$\nabla^2 \phi = 0 \quad (32)$$

subject to the boundary conditions

- 1) Neumann type in which $\partial\phi/\partial n$ is given
- 2) Dirichlet type in which ϕ is given
- 3) Mixed (Poincaré) type in which a linear combination of ϕ and $\partial\phi/\partial n$ is given

Mathematically, the solution to equation (32) can be found by expressing velocity potential at a point P in terms of ϕ and $\partial\phi/\partial n$ on the boundary of the flow field in the following integral equation (ref. 18):

$$\phi_P = -\frac{1}{4\pi} \iint_S \frac{1}{r} \frac{\partial\phi}{\partial n} dS + \frac{1}{4\pi} \iint_S \phi \frac{\partial}{\partial n} \left(\frac{1}{r} \right) dS \quad (33)$$

where $\partial\phi/\partial n$ can be identified as the source strength and ϕ as the doublet strength. The area S (fig. 12) need not include the boundary at infinity because the potential is known to be bounded at infinity.

When the exterior of the flow field ϕ' is considered, it can be related to the potential inside the flow field (ref. 18) as

$$\iint_S \phi \frac{\partial}{\partial n'} \left(\frac{1}{r} \right) dS = \iint_S \frac{1}{r} \frac{\partial\phi'}{\partial n'} dS \quad (34)$$

with $\partial/\partial n' = -\partial/\partial n$. Equations (33) and (34) combine to yield

$$\phi_P = -\frac{1}{4\pi} \iint_S \frac{1}{r} \left(\frac{\partial\phi}{\partial n} + \frac{\partial\phi'}{\partial n'} \right) dS + \frac{1}{4\pi} \iint_S (\phi - \phi') \frac{\partial}{\partial n} \left(\frac{1}{r} \right) dS \quad (35)$$

Note that there are an infinite number of combinations of the singularity strengths $(\partial\phi/\partial n + \partial\phi'/\partial n')$ and $(\phi - \phi')$ that will give the same value of ϕ at P. In order to render the system deterministic, we must either specify one of the two singularity strengths or provide a relationship between the two.

The boundary of the potential flow can now be identified. The outer flow beyond the edge of the boundary layer is essentially irrotational. Moreover, since the boundary layer is usually very thin, we extend the potential flow field to the configuration surface, but ignore the nonslip boundary condition (the "outer" solution). Since the wake is essentially a segment of the flow region filled with vortices shed from the trailing edge of the wing, it should be excluded from the potential flow field. A simplified treatment of the trailing vortices is to imagine the wake as a thin vortex sheet across which the normal velocity is continuous. With that in mind, equation (35) can be written as

$$\begin{aligned} \phi_P = & -\frac{1}{4\pi} \iint_{S_B} \frac{1}{r} \left(\frac{\partial\phi}{\partial n} + \frac{\partial\phi'}{\partial n'} \right) dS + \frac{1}{4\pi} \iint_{S_B} (\phi - \phi') \frac{\partial}{\partial \alpha} \left(\frac{1}{r} \right) dS \\ & + \frac{1}{4\pi} \iint_{S_w} \Delta\phi_w \frac{\partial}{\partial n} \left(\frac{1}{r} \right) dS \end{aligned} \quad (36)$$

where $\Delta\phi_w$ is the jump of potential across the wake.

In order to render the representation of equation (36) unique, we postulate certain conditions on the interior flow ϕ' , which is still at our disposal. If we put $\phi' = \phi$ and allow the normal velocity across the surface to be discontinuous, then equation (36) can be interpreted as a flow field set up by a distribution of sources on the surfaces. On the other hand, if we put $\partial\phi'/\partial n = \partial\phi/\partial n$, and allow the potential to be discontinuous across the surface, the flow field is disturbed from the onset flow by doublet distributions on the configuration surface and on the wake. Thus, the specification of the interior flow implies a selection of the type of singularity distribution to be placed on the surface. It should be noted that unless a linear relationship between the two types of the singularity strengths is specified (mixed boundary condition), the source and the doublet should not be allowed to be placed on the same portion of the boundary surface.

3.4.2 Numerical Method of TEA 230

In the present method, the source singularity is used on one part of the surface S_s , and the doublet singularity is used on other parts of the surface S_d and on the wake S_w . The Neumann type of boundary condition for analysis problems results in

$$\begin{aligned} \frac{\partial \phi}{\partial n} \Big|_{S_B} &= -\hat{n} \cdot \bar{U}_\infty && \text{on the body surfaces} \\ \Delta \phi_w &= \Delta \phi_{TE} && \text{on the wake} \end{aligned} \quad (37)$$

The singularity strengths can be uniquely determined from the integral equation

$$\begin{aligned} -\hat{n} \cdot \bar{U}_\infty &= -\frac{1}{4\pi} \frac{\partial}{\partial n} \iint_{S_S} \frac{\sigma}{r} dS + \frac{1}{4\pi} \frac{\partial}{\partial n} \iint_{S_d} \mu \frac{\partial}{\partial n} \left(\frac{1}{r} \right) dS \\ &+ \frac{1}{4\pi} \frac{\partial}{\partial n} \iint_{S_w} \Delta \phi_{TE} \frac{\partial}{\partial n} \left(\frac{1}{r} \right) dS \end{aligned} \quad (38)$$

where

$$\sigma = \left(\frac{\partial \phi}{\partial n} + \frac{\partial \phi'}{\partial n'} \right)$$

is the source strength and

$$\mu = \phi - \phi'$$

is the doublet strength.

In application, for nonlifting configurations only the first term on the right-hand side of equation (38) needs to be retained. For lifting configurations, the second term can be applied to model the shear surface such as fan faces, and the third term can be used to simulate the trailing vortex sheet. However, the doublet sheet starting at the trailing edge will imply a concentrated vorticity at the trailing edge of the wing. This concentrated trailing edge will cause numerical problems because the source strength near the trailing edge would have to adjust itself abnormally in order to satisfy the boundary condition near the trailing edge. The above numerical difficulty can be alleviated by providing a doublet sheet on the interior (preferably on the camber surface), as an extension of the trailing vortex sheet.

The numerical scheme to solve the integral equation, equation (38), is the standard panel method. The source sheet on S_S is divided into quadrilateral panels and passes through the midpoints of the straight lines connecting the corner points of a quadrilateral, on each of which the source strength is approximated as a constant. The doublet sheet on S_d is similarly divided into quadrilaterals. The doublet panel need not be planar because the velocity field induced by a constant-strength doublet panel turns out to be the same as that of a ring vortex along its perimeter for which the Biot-Savart law can be used.

For cases where there are more boundary points than the number of panels (equations), the boundary conditions must be satisfied in a least-squares sense. In this program, a boundary condition is applied at the centroid of each source panel and at the average point of each doublet panel. For each additional condition to be satisfied, an extra control point must be designated. For example, the Kutta condition can be imposed at the trailing edge by requiring that the velocity at the trailing edge be directed in the plane bisecting the trailing edge. This condition will control the spanwise variation of the wake doublet strength.

With this type of flexibility, the doublet singularity sheet of the internal lifting system can be placed in an arbitrary manner. If the near-field solution such as the load distribution on the wing is not of interest, one may eliminate a number of boundary points on the internal lifting system. This is done by arbitrarily assigning a certain pattern of vorticity strength (jump in potential), leaving only the imposition of the Kutta condition. The lifting-line theory implies a single, concentrated vortex placed at the quarter-chord location. Although the distribution of the bound vortices on the internal lifting system has no bearing on the far-field solution, it may impose a burden on the source distribution. This may result in a large gradient on the boundary surface close to the point where a large isolated bound vorticity is placed on the camber surface. The effect is further magnified for thin wings where the external surfaces are very close to the camber surface.

It is ideal to distribute the bound vortices in a smooth manner so that the source strength on the external surface will also be smooth. In figure 13, a number of concentrated bound vortices are shown to be located at a set of points on the camber surface. Each concentrated vorticity corresponds to a jump in potential. The only requirement is that the total jump be equal to the value at the trailing edge (and hence the value on the wake).

The induced normal velocity at each singularity panel is evaluated and the sum of all the contributions on a panel set equal to the known quantity at the boundary point on the panel. This results in a system of linear algebraic equations in the matrix form

$$[AIC] \{\lambda\} = \{\beta\} \quad (39)$$

where $\{\lambda\}$ contains μ and σ .

With source and doublet strengths solved, the flow properties such as velocity, pressure, forces, moments, and streamlines can be derived from equation (36). For instance, the pressure coefficient is calculated from the Bernoulli integral as

$$C_{p_i} = 1 - \frac{v^2}{U_\infty^2} \quad (40)$$

which is then scaled to the value in the compressible flow domain using the G6thert rule.

3.4.3 Discussion of TEA 230 Method and Solutions

The panels have many applications as basic building blocks in the TEA 230 program. The source panel can be considered as impermeable or permeable via the specification of the normal velocity. The permeable panel is used to simulate the mass transfer through surfaces, such as controlling the inflow to the fan face or adding the displacement thickness to simulate the boundary-layer effect. A boundary condition can also be specified at an off-body point; for example, on the engine inlet. The best result will be obtained by having a smooth source distribution with a small singularity gradient on each control point. A constant-strength doublet panel is a basic element of the lifting-system building blocks. Each doublet panel can be viewed as a ring vortex. Many constant-strength doublet panels can be positioned end to end to form a doublet column. Doublet columns can be in turn placed side by side to form a doublet lattice network.

By proper arrangement of these building blocks, a polynomial variation of the doublet strength on the network can be achieved. The versatility of this arrangement can be illustrated. For instance, each network can be overlapped to form a new element, thus providing an endless possibility for simulating a variety of lifting systems. These networks can provide the proper camber and twist of a surface and, therefore, can be used in the design of a surface for a given load distribution.

The superiority of this method compared with the FLEXSTAB method or its variants is its ability to model the actual configuration surface and the applicability of the boundary condition in the exact sense. Consequently, it will enable us to analyze the control-surface load distribution with provisions to account for the nose shape and the trailing-edge angle. As a matter of fact, the TEA 230 program is more capable of analyzing a thick wing than a

cambered wing because of the manner in which the lifting system is implemented in the program. For a very thin airfoil, a high density of internal panels is needed to prevent strong, localized effects on the source panels. In addition, since the wing-body interference effect takes place on the actual configuration surfaces, it eliminates the necessity for the interference shell employed in the FLEXSTAB system. This allows a greater flexibility of paneling since it does not require panel edges to be aligned in the streamwise direction.

The method of TEA 230 yields a pressure distribution on the source network surface; i.e., on the configuration surface. In terms of wing and tail, this implies the pressure on the upper and the lower surface. The load on the control surface can be taken as the difference of the pressures on the two surfaces. Alternatively, the hinge moment can be computed directly from the forces acting on each panel on the upper and the lower control-surface source network. For a load prediction near the planform breaks, the method of calculation does not differ from that of FLEXSTAB; i.e., neither method allows for the singular behavior near the breaks. For a control-surface load calculation, TEA 230 is superior in that it properly includes the thickness effect. The TEA 230 method also applies the boundary condition on the deflected control surface, although the boundary condition can be applied, as in the FLEXSTAB program, in a linearized sense. In essence, the linearized control surface is modeled as if it were undeflected, except that a local flow velocity (if known a priori) is used to more accurately simulate the perturbation velocity required on the panel surface, i.e.,

$$\bar{v} \cdot \hat{n} = -\bar{U}_\infty \cdot \hat{n} + V \sin \delta \quad (41)$$

whereas in FLEXSTAB, V is taken as U_∞ . The accuracy of the assumption can be evaluated by examining the streamlines resulting from the integration of the velocity field.

The outboard wing-pressure distributions for an aileron and an aileron-tab combination on a Boeing 747 wing are shown in figure 14. The solutions are obtained by applying the boundary condition in a linearized sense as given in equation (41). This approach was aimed at saving on the computer costs since only a reference configuration need be modeled.

A comparison of the results of this method with experimental data is made as follows for a modified NACA 65-210 airfoil shown in figure 15. This wing has an inboard partial-span trailing-edge flap deflected at 30 deg. The

computed spanwise load is shown in figure 16 while the forces, moment, and chordwise pressure distributions at five spanwise stations are displayed along with the experimental data in figures 17 and 18. The discrepancy is most likely the effect of boundary-layer thickening or separation on the flap.

The arrow-wing configuration (ref. 9) also was analyzed using the TEA 230 program. The panel arrangement is shown in figure 19, and the comparison of the result with experiment is given in figure 20. Also included in figure 20 is the result using the FLEXSTAB program. The chordwise-lifting-pressure distribution prediction by TEA 230 is clearly superior in many respects to the prediction of the FLEXSTAB method, especially in the neighborhood of the trailing-edge hinge line. However, for such a highly swept, low-aspect-ratio wing, both potential-flow programs are unable to predict the flow characteristics near the wingtip with a large flap deflection. The flow in that region is probably dominated by the spiral vortex, which is characterized by flow separation from the leading edge.

Since the TEA 230 method uses singularities of constant strength, the solution may also be sensitive to paneling of the network. A proper paneling scheme based on loading conditions on the planform breaks and discontinuous downwash locations may have to be sought so that a relatively sparse panel arrangement can still predict the loading with reasonable accuracy.

3.5 PAN AIR PILOT PROGRAM METHOD

The PAN AIR pilot code is a computer program system that employs advanced numerical techniques in solving the analysis and design problems for steady, subsonic potential flow (refs. 19 and 20). The outstanding features of the method include curved panel approximations, polynomial type of singularity strength variations, and exact boundary-condition applications. The numerical results are more accurate and stable compared with other existing potential-flow programs. The method is currently being expanded and improved both in engineering and software design under a contract with several Government agencies (NASA-ARC, NASA-LRC, AFFDL).

3.5.1 Outline of PAN AIR Method

The integral equation corresponding to the boundary-value problem for the potential flow is the same as that described in section 3.4 for the TEA 230 program. Specifically, the potential can be expressed as the sum of the surface integrals

$$\phi_p - \iint \sigma \left(-\frac{1}{4\pi r} \right) dS + \iint \mu \frac{\partial}{\partial n} \left(\frac{1}{4\pi r} \right) dS \quad (42)$$

For analysis problems, the specification of the boundary condition yields the integral equation

$$\frac{\partial \phi}{\partial n} = \frac{\partial}{\partial n} \iint \sigma \left(-\frac{1}{4\pi r} \right) dS + \frac{\partial}{\partial n} \iint \mu \frac{\partial}{\partial n} \left(\frac{1}{4\pi r} \right) dS \quad (43)$$

while the integral equation corresponding to the design problems is

$$\frac{\partial \phi}{\partial t} = \frac{\partial}{\partial t} \iint \sigma \left(-\frac{1}{4\pi r} \right) dS + \frac{\partial}{\partial t} \iint \mu \frac{\partial}{\partial n} \left(\frac{1}{4\pi r} \right) dS \quad (44)$$

Auxiliary conditions such as closure and finite downwash are required for uniqueness when solving equation (44). The standard panel schemes are used in solving these equations. While they are solved for the incompressible flow, the subsonic results are subsequently derived by transformation.

The advanced technique for representing panels and singularity distributions is designed to overcome certain practical difficulties encountered in the earlier panel methods. The flat panels with constant singularity strength are very crude in simulating boundary surfaces having large curvature, such as the wing leading edge, unless very dense paneling is used. The local curvature and an accurate singularity strength gradient are also needed for providing a more realistic velocity gradient that may be crucial in an area such as boundary-layer calculations. Moreover, most panel methods are known to exhibit sensitivity with respect to the panel configuration; the combined features of this method are to minimize this sort of sensitivity. The higher degree panel method is required from other considerations as well. For design problems, it turns out that a singularity strength with more than one degree of freedom is also needed.

The basic building block of the paneling scheme is the network. A network can be viewed as part of the paneled configuration surface that is used to simulate the specific physical phenomenon on that surface. These networks can be combined to allow the analysis and design on configurations having thin or thick wings, fuselage, nacelles, empennage, wake, efflux tubes, ducts, or flaps. Each network differs in singularity degrees of freedom and the boundary points at which the boundary conditions are enforced. Four general types of the networks are employed in this method: source-analysis, doublet-analysis, source-design, and doublet-design. These networks are characterized by a separate set of the geometry specification, singularity parameter location,

control point location, and the influence coefficient, of course. The new features of the method are briefly described as follows.

Panel Surface Definition--A curve panel is represented by fitting a paraboloid through the corner points that define the configuration surface. The discontinuities in surface, slope, and curvature occur only on the network edges.

Thus, the coefficients in the panel surface representation

$$\zeta = c_1 \xi^2 + c_2 \eta^2 + c_3 \xi \eta + c_4 \xi + c_5 \eta + c_6 \quad (45)$$

are obtained by minimization of the square error

$$R = \frac{1}{2} \sum_k W_k (\zeta - \zeta_k)^2 \quad (46)$$

where ζ_k is the ordinate for the kth mesh point and W_k is the weight that is chosen to be very large for a corner point through which the surface will pass. The ratio of the height to the diameter $|\zeta|/\sqrt{\xi^2 + \eta^2}$ is assumed to be small to allow for expansion of the kernel and the integrations in closed form.

Singularity Strength Definition--Discrete values of singularity strength are placed at certain standard points on each network. The distribution of singularity strength on a source network is assumed to be linear, i.e.,

$$\lambda(\xi, \eta) = \sigma(\xi, \eta) = \sigma_0 + \sigma_\xi \xi + \sigma_\eta \eta \quad (47)$$

and that on a doublet network is quadratic, i.e.,

$$\begin{aligned} \lambda(\xi, \eta) = \mu(\xi, \eta) = & \mu_0 + \mu_\xi \xi + \mu_\eta \eta + \frac{1}{2} \mu_{\xi\xi} \xi^2 \\ & + \mu_{\xi\eta} \xi\eta + \frac{1}{2} \mu_{\eta\eta} \eta^2 \end{aligned} \quad (48)$$

The coefficients of the singularity distribution on each panel, source or doublet, are obtained by minimizing the error

$$R = \frac{1}{2} \sum_k W_k (\lambda - \lambda_k)^2 \quad (49)$$

where the summation extends over all singularity parameter locations on the particular panel and the neighboring panels as well.

Boundary Condition and Boundary Points--At each panel center boundary point, the boundary condition for analysis problems reads

$$c_1(\hat{n} \cdot \bar{V}) + c_2\lambda = \beta \quad (50)$$

while for design problems

$$(\bar{t}_1 \cdot \bar{V}) + (\bar{t}_2 \cdot v\lambda) = \beta \quad (51)$$

For example, the usual condition for analyzing the flow over an impermeable surface is given by specifying $c_1 = 1$, $c_2 = \beta = 0$. In order to control the edge downwash or to provide a precise network matching, the boundary points are also placed on the network edges (which may be slightly withdrawn from the edges to eliminate numerical problems). Thus, the standard boundary points include the panel center points as well as edge abutment points in case of doublet network to enforce the aerodynamic requirements such as the Kutta condition or the continuity of singularity strength across the network junctions, etc.

For the source-design network, it is also required that on each panel column the closure condition

$$\iint [c_1(\hat{n} \cdot \bar{V}) + c_2\lambda] dS = \iint \beta dS \quad (52)$$

be satisfied.

Influence Coefficient Calculations--The potential due to the singularity distribution on a curved panel, as it stands, cannot be integrated in a closed form. However, the closed-form integration is superior to the numerical integration in all aspects. The closed-form integrals are obtained for the aerodynamic influence coefficients for the near-field through an expansion based on a small panel curvature assumption; and for the far-field, through an expansion based on the large separation between the singularity panel and field point. Recursion formulas that reduce the complicated expressions to those appearing in the flat-panel, constant-strength singularity techniques are used extensively to facilitate the economy and simplicity in the calculation of the influence coefficient.

3.5.2 Discussion of PAN AIR Method

In addition to the various versatile aspects found in the TEA 230 program, the PAN AIR pilot program has many extra features.

With higher order of singularity distributions on the panel, the accuracy of the solution is presumably better. Specifically, with linearly varying source singularity distribution and quadratically varying doublet singularity

distribution, the computed perturbation on each panel is linearly varying instead of constant as in FLEXSTAB or TEA 230. Using the Bernoulli integral, the pressure is piecewise quadratically varying on each panel. The forces and moments are obtained by integration on each panel and summed over all the panels. The hinge moment calculated in this manner is definitely superior to the constant-strength singularity panel method. Since the spline techniques are extensively used in the panel geometry definition and the singularity strength distributions, the solution is more stable and less sensitive to paneled configuration. However, numerical difficulties arise when the edges of some panels are near the control points of others, and the use of fine paneling in regions of rapid flow variation often forces fine paneling elsewhere. Therefore, as in all panel methods, the proper paneling criteria need to be determined.

The numerical results are presented for a 35-deg sweptback wing with partial-span trailing-edge control surface as depicted in figure 21. Three different models are used to simulate the flow on the wing, the flap, and the gaps. In the first two panel models, the exact boundary condition is applied on the flap surface. In the third panel model, the boundary condition is satisfied only in the linearized sense, similar to that implemented in the FLEXSTAB program. The modeling of the wake on the side-edge gaps differs in the first two panel models: for the first panel model, it is assumed that the vorticity is shed from the trailing edges only; for the second panel model, the vorticity is shed from the wing side edges but not from the flap side edges. The chordwise lift distributions at five spanwise stations are displayed in figure 22. The lift distributions for the first two panel models differ only along the wing side of the gaps as is expected. The difference diminishes toward the trailing edge and is not discernible along the flap side of the gap (and hence not shown in the figures). The lift distributions for the third panel model are shown to agree better with the FLEXSTAB results, as they should. Both are close to the lift distribution of RHO 4, which also uses the linearized boundary conditions. At the midspan, the lift distributions corresponding to those three panel models and the FLEXSTAB result are fairly close. However, these results indicate that the panel methods predict higher lift than the collocation method or the test data given in reference 21. It is unknown whether the discrepancy is attributable to the effect of thickness, which is not included in the panel-method analyses.

3.6 SUMMARY OF METHODOLOGIES OF POTENTIAL-FLOW PROGRAMS

The methodologies of FLEXSTAB, RHO 4, TEA 230, and PAN AIR pilot code are summarized in table 8. The entries of table 8 include the year a particular program was developed, the panel geometry, the singularity type, and the restrictions, if any. In application, FLEXSTAB and RHO 4 programs only accept mean surface paneling; therefore, the deflection of control surfaces is simulated in a linearized sense. On the other hand, the surface paneling is possible in either the TEA 230 or the PAN AIR pilot program; hence, the control-surface deflection can be treated in an exact manner. However, associated with the actual surface paneling is the difficulty of modeling the trailing vortices properly.

SECTION IV

RECOMMENDATIONS FOR THE BEST APPROACH USING THE FLEXSTAB METHOD

Despite the numerous cited limitations on the FLEXSTAB method, the method has been found to be adequate in predicting approximate aerodynamic characteristics, provided: (1) the assumption of small flow perturbations is not violated and (2) the proper paneling scheme is employed. For hinge-moment calculations in the linear range, i.e., when the control-surface deflection is small, condition (1) is likely to be satisfied. To satisfy condition (2), however, we need some insight into the local aerodynamic characteristics along the control-surface hinge line, the side edges, and the planform breaks. Inaccuracies arise in the analysis of the load distribution on a simple control-surface configuration, not only because condition (2) is difficult to achieve but also because a constant-pressure panel is inherently weak in handling the large pressure gradient near the hinge line and side edges. In this section, condition (2) is explored in depth to reveal the essential role it plays not only in the panel methods like FLEXSTAB but in virtually any numerical method that solves a differential equation using an integral representation. A better scheme of handling the loadings in the regions of singularity is also proposed for panel methods in general.

4.1 INTEGRAL REPRESENTATION OF DIFFERENTIAL PROBLEMS

It is known that an equivalence exists between the integral equation and

an initial-value or boundary-value problem of mathematical physics. In aerodynamics, these problems correspond to unsteady and steady flow problems, respectively. For fluid dynamic problems, the partial differential equation governing the conservation of mass, momentum, and energy in steady state is linearized and then transformed into the Laplace equation for which Green's function (or kernel function) is well known. Using Green's theorem, the solution of the partial differential equation is symbolically expressed by an integral equation. The solution of the flow problem is then obtained by solving the equivalent integral equation numerically.

Various methods such as algebraic, iterative, collocation, and least squares exist to solve the integral equation numerically. In general, panel methods (FLEXSTAB, TEA 230, or PAN AIR) involve direct integration over the panel, while the RHO 4 program employs the collocation method. Regardless of the method used, each results in an algebraic formulation of the problem employing matrix algebra. Two methods of solving the integral equation are reviewed in the next section for identifying certain properties that may be useful in the panel methods.

4.2 METHODS OF SOLVING INTEGRAL EQUATION

Consider the task of determining $\lambda(x)$ from the linear integral equation

$$\int_a^b K(x;\xi) \lambda(\xi) d\xi = w(x) \quad (53)$$

which is an integral equation of the first kind or Fredholm's equation. The function $K(x;\xi)$ represents a given kernel ($\hat{n} \cdot \nabla$ operates on the potential induced by a point source or doublet singularity), $w(x)$ is a prescribed function (normal velocity or mass flux on the boundary), and $\lambda(x)$ can be interpreted as the singularity strength or the load distribution.

With the procedures of the algebraic method, the integral on the left side of equation (53) is replaced by a summation of n terms augmented by an error term as

$$\int_a^b K(x;\xi) \lambda(\xi) d\xi = \sum_{j=1}^n H_j \lambda(\xi_j) + E_n \quad (54)$$

where the abscissas ξ_j as well as the corresponding coefficients H_j have been chosen to obtain the desired degree of accuracy with a given number of the terms and to suppress the error term E_n below a predetermined limit.

Inserting equation (54) into equation (53) and assuming that n is sufficiently large and H_j, ξ_j are properly chosen for the error E_n to be ignorable, the integral equation can then be replaced by an algebraic relation of the form

$$\sum_{j=1}^n H_j \lambda(\xi_j) = w(x) \quad (55)$$

Since there are n unknown $\lambda(\xi_j)$'s in equation (55), we can write the same equation for n discrete values of x as

$$\sum_{j=1}^n H_j \lambda(\xi_j) = w(x_i) \quad (56)$$

$i = 1, 2, \dots, n$

This represents a system of simultaneous linear algebraic equations with the same number of unknowns. The unknowns $\lambda(\xi_j) (j=1, 2, \dots, n)$ can be uniquely determined as long as the determinant of the coefficients on the left side of equation (56) does not vanish, which is generally the case for a well-imposed boundary-value problem. The approximate solution of $\lambda(x)$ in equation (53) can be regarded as a polynomial of degree $(n-1)$ passing through the n pivotal ordinates.

In the collocation method, we assume a solution in the form of a linear combination of suitably chosen mode functions $g_k(x)$ as

$$\lambda(x) = \sum_{k=1}^m a_k g_k(x) \quad (57)$$

where a_k are arbitrary constants. Substituting this expression into equation (53), we find

$$\sum_{k=1}^m a_k \int_a^b k(x; \xi) g_k(\xi) d\xi = w(x) \quad (58)$$

where the error of representing $\lambda(x)$ by equation (57) has been ignored.

When equation (58) is written for m distinct values of $x_i (i=1, 2, \dots, m)$, it becomes

$$\sum_{k=1}^m a_k \text{MIC}_{ik} = w(x_i) \quad (59)$$

where

$$MIC_{ik} = \int_a^b K(x_i; \xi) g_k(\xi) d\xi$$

can be evaluated as in equation (54). When the constants a_k ($k=1,2,\dots,m$) have been solved, the solution is given by equation (57).

The procedures, as they stand, are very simple. However, an error does arise because of ignoring the error term (apart from the round-off error). In fact, the determination of H_j and ξ_j , which renders the error term E_n a minimum, encompasses the whole subject of the mechanical quadratures (ref. 22).

Basically, we are concerned with a set of discrete abscissas ξ_j and the corresponding coefficients H_j , which will render the equivalence like that in equation (54) valid without the error term. By Weierstrass' theorem on polynomial approximation, any continuous function $\lambda(x)$ can be approximated within $[a,b]$ to any accuracy by a polynomial of sufficiently high degree. As a polynomial of n th degree can be uniquely specified by $(n+1)$ constants, the $2n$ constants (H_j and $\xi_j, j=1,n$) in equation (54) can, therefore, accurately determine a polynomial $\lambda(x)$ of degree $(2n-1)$ or less. If the function $\lambda(x)$ is of higher degree, as is usually the case in aerodynamic problems, it cannot be adequately represented by finite terms and an error cannot be avoided.

Graphically, equation (54) without the error term states that the shaded areas cancel each other between the curves; one represents the $(2n-1)$ st degree polynomial $\lambda(x)$ and the other represents the polynomial of $(n-1)$ st degree that passes through the pivotal points, as shown in figure 23.

A family of the formulas that are developed systematically to attain the maximum precision in mechanical quadratures is generally associated with the Gaussian quadratures. Gauss' work was extended subsequently by many others. A detailed account of the various types of quadratures can be found in reference 22. Only the essential elements of Gaussian quadrature need to be described here. It has been shown that the abscissas ξ_j ($j=1,n$) chosen to render the error term a minimum (zero if $\lambda(x)$ is a polynomial of $(2n-1)$ st degree or lower) are the roots of a certain orthogonal polynomial. The type of orthogonal polynomial depends on the type of the kernel and weight function that may be present. For example, for a smooth $\lambda(x)$ with unit weight function, the abscissas x_j are the roots of the Legendre polynomial, and the scheme is

called the Gauss-Legendre quadrature; for the logarithmic type of weight function we use the log-Gaussian quadrature, etc. The properties and the values of the coefficients $H_j(j=1,n)$ corresponding to each type of the quadrature are also given in reference 22. The purpose of the discussion here is to shed some light on the way the panel methods should preferably be directed.

4.3 IMPROVED FLEXSTAB METHOD OF SOLVING INTEGRAL EQUATION

Without loss of generality, we will consider the integral equation corresponding to the two-dimensional problem given in equation (53). Assuming that the function $\lambda(x)$ is expressible by its values at n points as

$$\lambda(x) = \sum_{j=1}^n L_j(x) \lambda(x_j) \quad (60)$$

where $L_j(j=1,n)$ are obtained by certain interpolation formulas or least-squares spline techniques, then equation (53) can be evaluated at $x = x_i$ as in equation (55), i.e.,

$$\sum_{j=1}^n H_j(x_i) \lambda(x_j) = w(x_i) \quad (61)$$

where

$$H_j(x_i) = \int_a^b L_j(\xi) K(x_i; \xi) d\xi \quad (62)$$

With the panel method, the interval $[a,b]$ is subdivided into n segments. Specifically, for the constant-vortex-panel method of FLEXSTAB, we have

$$L_j(x) \equiv 1 \text{ for } x \text{ in } \Delta_j \\ \equiv 0 \text{ otherwise}$$

where Δ_j is the j th segment or panel. Then equation (62) becomes

$$H_j(x_i) = \int_{\Delta_j} K(x_i; \xi) d\xi = AIC_{ij} \quad (63)$$

so that the solution of the integral equation reduces to solving the matrix equation

$$[AIC]\{\lambda\} = \{w\} \quad (64)$$

One notices that the above equation is identical to equation (5) if one identifies $\{\lambda\}$ as the singularity strength $\{S\}$ and also $\{w\}$ as the downwash $\{\psi\}$. This linkage provides a vehicle to convey the well-established knowledge developed in the mechanical quadrature to the panel scheme in the panel.

methods. As shown in section 4.2, the values of H_j and ξ_j ($j=1, n$) must be so determined from $K(x; \xi)$ that equation (55) can be adequately used to represent the integral equation, equation (53), with least error. However, the values of ξ_j are exactly the dominant factors in determining the paneling configuration for the panel methods.

The above consideration, however, is incomplete because in the panel methods the control point arrangement is also related to the paneling configuration (even though it need not be). In general, the control points at x_i ($i=1, n$), where the boundary conditions are imposed, are located somewhere within the panel. Thus, the determination of ξ_j will depend not only on the kernel function $K(x; \xi)$ but also on the downwash distribution $w(x)$.

For instance, a discontinuous downwash field occurs whenever the control surface is deflected. Corresponding to this downwash distribution, there are certain loading characteristics along the hinge line and side edges. The paneling configuration must therefore reflect the specific loading characteristics due to downwash discontinuities. As the downwash field is also related to the planform geometry, the paneling configuration is dependent upon the planform shape. In general the loading characteristics on a lifting surface depend roughly on two distinct categories of configurations. The first category is related to planform edges, tips, cranks, and apexes, among which the leading-edge singularity in subsonic flows and the smoothness of the loading at trailing edges (Kutta condition) are the familiar ones. The second category is related to discontinuous downwash field, such as those due to control-surface deflections.

In reference 23, the differential equation governing the flow near the planform breaks (i.e., the corners, tips, cranks, and apexes, fig. 24) is reduced to an algebraic eigenvalue problem. Each flow region near the planform break is idealized as being infinite in extent; i.e., an angular sector. The solutions for each region are not unique because of the lack of a boundary condition at infinity. The differential equation and the boundary conditions are both homogeneous; solutions can be found only for certain eigenvalues, and the corresponding solution is an eigenfunction. These solutions for each angular region are the local solutions, which are then patched into the outer solution valid on the remainder of the flow field.

The loading characteristics near the control-surface hinge line and side edges are developed in reference 14 for a nonswept control surface using the matched asymptotic expansion method. The inner solution that governs the flow characteristics near the control-surface leading edges, side edges, and corners is further applied to cover the special situation where the control hinge line extends to the tip of the lifting surface in references 11 through 13 and 15. A survey of the loading singularities inherent in the linearized wing theory is given in reference 24. The available solutions are tabulated with regard to the discontinuities in surface slope, planform breaks, dihedral, etc. The singularities are categorized as either local or global. By local singularity, the singularity strengths--not only the form--are fixed by the condition at the singularity line and are therefore independent of the general shape and motion of the lifting surface. The global singularities are those that do not permit the coefficient of singularity strength to be determined prior to the specification of the wing planform shape and upwash distribution due to the motion. These undetermined coefficients indicate the fact that the lowest order inner expansions of the solutions are actually the eigenvalue problem as treated in reference 23. In some cases, the coefficients can be fixed through the matching process where the method of inner and outer expansion has been shown to apply, as illustrated in reference 14. Some of the solutions have been integrated into the kernel function procedures with success and improvement, as in references 11 through 13.

Once the loading characteristics near the planform breaks or control-surface hinge line and side edges are known, it is possible to express the total loading $\lambda(x)$ as a linear combination of the singular loading functions $g_k(x)$ corresponding to each particular region and the regular loadings as

$$\lambda(x) = \sum_{k=1}^m a_k g_k(x) + \sum_{j=1}^n L_j(x) \lambda(x_j) \quad (65)$$

Upon substitution into equation (53), we find at $x = x_i$,

$$\sum_{k=1}^m a_k \int_a^b g_k(\xi) K(x_i; \xi) d\xi + \sum_{j=1}^n \lambda(\xi_j) \int_a^b L_j(\xi) K(x_i; \xi) d\xi = w(x_i) \quad (66)$$

Using the notation in equations (59) and (63), we have

$$\sum_{k=1}^m a_k MIC_{ik} + \sum_{j=1}^n \lambda_j AIC_{ij} = w_i \quad (67)$$

where $w_i \equiv w(x_i)$ and $\lambda_j \equiv \lambda(x_j)$.

Since there are $(m+n)$ unknowns on the left side of equation (67) but only n regular control points for which w_i ($i=1, n$) are given, the system of equations in equation (67) can be made determinate by supplying m additional control points. Each of these additional control points is used to determine the coefficient of singularity strength associated with the singular region on the planform and is located somewhere in the region.

Recalling the methods of solving integral equations in section 4.2, one notices that the solution procedure just outlined is equivalent to a combination of the algebraic method and the collocation method. The distinct feature of the solution written in the form of equation (65) is that the correct loading characteristics near the planform breaks or control-surface hinge line and side edges can be properly accounted for by using the accurate quadrature integration technique since the panel methods (especially the constant-pressure panel) are very poor in handling the flow regions with rapid change of loading conditions. Once that part has been taken care of, the rest can be easily handled by the usual panel methods.

In the special case when the singularities in these flow regions are local, that is, the singularity strengths a_k as well as the form $g_k(x)$ are independent of the general shape and motion of the lifting surface and they are considered as known (cf. ref. 24), then we can rewrite equation (67) as

$$\sum_{j=1}^n \lambda_j AIC_{ij} = w_i - \sum_{k=1}^m a_k MIC_{ik} \quad (68)$$

The summation on the right-hand side of equation (68) is the downwash associated with the loadings in the singular regions; hence, the right-hand side becomes the residual downwash, which is presumably smoother than the original downwash distribution. One can find the residual loading w_j ($j=1, n$) using the standard technique in FLEXSTAB. The total loading is the sum of the loadings corresponding to the singular regions and the residual loading.

The improvement given above is not only applicable to the constant-strength panel method FLEXSTAB but also to other panel methods. In the panel methods, the singularity strength on each panel has been prescribed to be either constant (e.g., FLEXSTAB), linearly varying (e.g., ref. 25), or of higher order. In the PAN AIR pilot code, the doublet singularity employed to

simulate the lift is assumed to be quadratically varying and also continuous across the panel edge by a least-squares spline fit over the neighboring panels. As the degree of the polynomial assumed for the singularity distribution increases, so the complication of the solution increases. As long as the degree of the polynomial for the singularity distribution is so limited, an error will exist that is more pronounced in the singular regions, because the loadings in those regions (e.g., logarithmic function, inverse square root) usually cannot be accurately expressed by lower order polynomials.

To conclude this section, two numerical examples are given to illustrate the effect of the paneling scheme on the accuracy of the solution. The first example is the load distribution on the YF-16 wing with flap deflected by 0.1 rad. The details of the paneling of this particular example are shown in figure 1. The chordwise load distributions at three spanwise stations are shown in figure 25, (a) through (c). Also included in the figure are the residual loadings that are obtained by subtracting the singular loadings from the total loadings shown in the same figures. These singular loadings are the inner solutions obtained from the method of matched asymptotic expansion (ref. 14), with modifications applied to provide the proper loading conditions near the wing leading edge, trailing edge, and side edges (refs. 11 through 13). As stated in reference 14, the inner solution of this type yields not only the form but also the strength of the singularity along the hinge line; thus the nonvanishing values of the residual loadings near the hinge line indicate the discrepancy between the predicted loadings and the loadings the linearized theory should actually yield. These figures also show that FLEXSTAB overpredicts the loads over the wing with control surface deflected. The downwash distribution corresponding to the singular loading⁽¹⁾ at each control point along three spanwise stations is shown together with the step downwash distribution in figure 25(d). The large value of the residual loading along the hinge line results from improper paneling that does not fully reflect the

(1) The downwash corresponding to the singular loading computed here is only an approximation of MIC_{ij} in equation (59), i.e.,

$$w_{i,AE} = MIC_{i1} = \iint K(x_i, y_i; \xi, \eta) g_1(\xi, \eta) d\xi d\eta \\ \approx \sum_j AIC_{ij} g_1(x_j, y_j)$$

where (x_j, y_j) are panel centroid locations.

singular behavior near the hinge line and the side edges. The accuracy of the solution can be improved if the new schemes, equations (65) through (68), are used.

The second example is a 35-deg sweptback wing of aspect ratio 4 as depicted in figure 21. To retain the proper singular behavior near the control-surface hinge line and side edges as predicted in the linearized theory, the wing and partial-span, trailing-edge control surface are paneled using the simple cosine function distribution. The total loadings and the residual loadings along five spanwise stations are shown in figure 26(a) through (e). It is noticed that the residual loadings near the hinge line (fig. 26(b) through (d)) are much smaller than those in the YF-16 case. This indicates that with proper paneling in the neighborhood of the planform discontinuities, the FLEXSTAB results of the airload on the control surface are reasonably close to those predicted by the inner solution derived from the method of matched asymptotic expansion. The downwash field corresponding to the singular loadings is shown in figure 26(f) along with a step-function distribution of the prescribed downwash due to a control deflection of 10 deg. The comparisons of the chordwise pressure distribution near the midspan between the FLEXSTAB result, the experimental data of reference 21, and the collocation methods of references 13 and 26 are shown in figures 27 and 28. The FLEXSTAB result is shown to overpredict the loading behind the hinge line only slightly compared with test data and the results of other numerical methods.

SECTION V

RECOMMENDATIONS FOR FUTURE RESEARCH AREAS FOR HINGE-MOMENT ANALYSIS

The subject of theoretical prediction of control-surface hinge moment involves a wide spectrum of aerodynamic disciplines. Although one may conveniently take the steady solution as the lower limit of the more general unsteady solution, the different ranges of flight conditions (Mach number, in particular) make the problem very complicated and thus beyond regular treatment. For example, in the transonic regime, the shock appears in the flow field and interferes with the boundary layer. Under such circumstances, the

flow field is nonuniform in the sense that the governing differential equation in one region has entirely different characteristics from the other. That is, one may have a supersonic flow regime (flow equation being of hyperbolic type) embedded in the subsonic main flow (elliptic type). In addition, the flow equation in a layer adjacent to the wing surface is of parabolic type. Thus, the nonuniform flow has deterred the general solution.

Although the major part of the flow field can be idealized as conservative, the effect of viscosity cannot be completely ignored (the Kutta condition is the consequence of this effect). The effect of viscosity plays a significant role in the upper-surface flow of a positively deflected control surface. The adverse pressure gradient toward the trailing edge of the flap retards the flow to such an extent as to cause the flow to become separated. Even though claims have been made implying success in obtaining the approximate solution of the flow phenomena up to the separation point (or line), the solution beyond the separation is still elusive. A common assumption is that the pressure is constant in the bubble of separated and recirculated flow. A reasonable scheme used to handle such a type of flow field would be of an iterative nature. The boundaries of different flow regimes (boundary layer, thick wake, and potential flow) are initially assumed; then the solution to each flow regime is obtained until a solution is converged that satisfies all of the boundary conditions.

The shape of a wake is another aspect of the flow that deserves some attention. Although the wake does not significantly affect the flow on the wing as it does on the tail or stabilizer, a scheme that can estimate the self-deformation (or true position) of the wake may prove to be useful in imposing the boundary condition on the aft lifting surfaces and flaps.

A new modeling technique for trailing-edge wake analysis using a potential-flow program based on the vortex method (Boeing TEA 372) was suggested in reference 27. It was claimed that the large fluctuation in either lift level or lift-curve slope predicted by panel methods for a flapped wing arises from the variation in the path assigned to trailing vorticity, especially that of the wingtip and flap side edges. A reasonably effective modeling scheme was suggested as a result of helium-bubble-flow visualization for a Boeing advanced-technology airfoil with flaps. Examples of modeling guidelines are:

- 1) All vortices shed at wingtip should be modeled as straight lines leaving the trailing edge in the freestream direction.
- 2) The wake leaving the trailing edge of either wing or flap should be bent in the direction of the bisector between trailing edge and freestream, and then aligned with the freestream after a short distance.

Another area of concern is the flow phenomenon near the gaps of the control-surface side edges. It is evident that the hinge-moment calculation must properly account for the flow pattern as a result of the viscous effect. This is the case when mathematical models are devised to simulate the actual flow problem by using the compromising boundary conditions. For instance, in predicting the pressure distribution on the 35-deg sweptback wing using the PAN AIR pilot program, three different arbitrary mathematical models are used that differ in the representation of the gaps on the control-surface side edges and in the boundary condition specifications (exact or approximate). The solution corresponding to each mathematical model differs significantly near the side edges, as expected. It is difficult to determine which model more closely resembles the actual flow condition since the supporting experimental data are still lacking. Once the flow characteristics are more thoroughly understood, an optimum model can be constructed using a wide variety of the options available from the advanced panel aerodynamic program currently being developed. Numerical experimentation with different mathematical models is expected to be necessary in using the potential-flow program to solve the real flow problem as in the deflected control surface. The concept guiding this approach can be illustrated by the case of predicting load distribution on a low-aspect, highly swept wing set at a large angle of attack. The load on the wing is dominated by separated flow right from the leading edge. The potential-flow method provides no means of solution when the flow becomes separated. However, from the observed flow pattern, the separated flow and wakes can be simulated by conceiving a rolling-up free-vortex system with feeding sheets, fed sheet, vortex core, etc. The boundary conditions are appropriately applied at the sheets whose locations are found by iteration until the solution converges to the one that compares favorably with the measurement (refs. 28 and 29).

The same concept can be applied not only to the flow modeling over the control surface but also to a wide variety of aerodynamic problems such as free jet, slipstream, plume with entrainment, evolution of wake, etc. In this

sense, we can extend the range of applicability of the potential flow outside the thin layer dominated by the viscous effect to include the vast regime of the flow field created by the viscous effect, provided the mathematical model can be devised to fit the salient portions of the real flow very well. Application of this sort is valuable since viscosity is always present. The foregoing problems constitute the unfinished aspects of aerodynamic technology and should be viewed as long-term research projects as far as hinge-moment prediction is concerned.

The short-term research project is improving the accuracy of the hinge-moment calculation based on the linear aerodynamic theory. The valid range of linear theory is associated with thin, small-curvature cambered wings at small-angle-of-attack cruising at Mach numbers away from the critical value. Flow of this type is free of separation and shock formation, so that equation (1) applies. Under such circumstances, the linearized boundary condition may be adequately applied since it is consistent mathematically with the linearized flow equation and the linear relationship between pressure and perturbation velocity. All the methods discussed in section III offer some solutions varying to a certain extent from one to another. The panel methods, in particular, are superior because pressure loading functions need not be assumed prior to the solution, as required in the collocation method. However, a systematic study of paneling configurations has yet to be made. Generally it is not possible to use very dense paneling because of the constraints of cost or capacity of the computer.

In order to alleviate the difficulty of obtaining the optimum paneling, which is crucial to the solution near the hinge line, side edges, or planform breaks, the inner solutions obtained from the asymptotic expansion method in these regions can be incorporated into the panel methods as described in section 4.3. The recommended method subsumes the distinctive features of the existing numerical schemes in the sense that the solution will properly reflect the loading conditions in regions of rapid change of flow properties. The philosophical aspect of the solution procedure is nothing more than saying that the more one knows about the answer, the more closely one can guess the outcome. The success of the proposed numerical scheme, however, cannot be assessed prior to actual implementation.

SECTION VI

CONCLUSIONS

The success of any method for control-surface hinge-moment prediction must ultimately be evaluated by its ability to yield the result that agrees with experimental data. One criterion would be that different approaches to a mathematical idealization of the physical problem should yield the same result. In view of the complicated flow phenomena associated with the control deflection, enhanced physical understanding of the problem is necessary for the mathematical treatment of the subject. The problem is essentially nonlinear in such flow phenomena as boundary-layer separation evolving to free vortex flow or shock waves interacting with boundary layers. The principle of superposition no longer applies and, thus, forms an unfinished area of the subject. In cases where the major part of the flow field can be characterized as potential and the perturbation due to the presence of the body is small, the linearized potential-flow theory finds its application. Because of the mathematical tractability of the theory, the elegant representation of the solution in a convenient form renders various numerical schemes possible.

Comparison of the hinge moments obtained by the Boeing and AFFDL FLEXSTAB analyses for the basic (AFFDL) paneled YF-16 model showed the expected agreement for the rigid airplane, but the comparison for the flexible airplane showed differences of up to 50% in some derivatives. Since these differences were too frequent to be typographical, it is apparent that there must be some differences between AFFDL and Boeing in SD&SS input data, NASTAP data, or the ESIC program.

With regard to the near-field/far-field option, the erratic results obtained may be due to coding errors. An investigation using a simple four-panel model confirms this supposition.

The importance of correct hinge-line location is obvious from the results presented. In the case of the flaperon, the hinge line was misplaced in the AFFDL results so that the leading row of panels subtracted from, rather than added to, the hinge moments, thus leading to the very small derivatives obtained. A similar but smaller error may exist on the horizontal tail.

The analysis of the four different paneling schemes employed (excluding the erratic near-field/far-field results) showed some variation between the hinge moments. For the rudder, which is more isolated from the other thin bodies, the hinge moments vary relatively little from scheme to scheme. However, for the flaperon and (even more so) for the horizontal tail, the hinge moments are more panel dependent. In the case of the latter, this may in part be due to the effect of downwash at the tail. It is noticeable that the hinge moments obtained from the low-density model were generally the smallest.

Without comparing the results with other data (such as wind tunnel data), it is difficult to decide which paneling scheme gives the best results. Similarly, there are at present no definite criteria for obtaining the optimum paneling for a given configuration. Since the hinge moments are affected by the paneling, it is desirable that such criteria be formulated.

It is apparent from this and other studies (e.g., ref. 2) that generally FLEXSTAB overestimates the hinge moments $C_{h\alpha}$, $C_{h\delta}$, etc., when compared with wind tunnel data. This is because actual control-surface load distributions are affected by such parameters as the trailing-edge angle. FLEXSTAB does not calculate such effects; however, the program is useful in that it calculates hinge moment and stability derivatives that are not easily found in any other way, together with the effects of airplane flexibility on their derivatives.

Regarding the semiempirical methods of Datcom, the hinge-moment prediction is restricted to the linear range of small angles. Since the method is based on the lifting-line theory with the effect of sweep, etc., accounted for by using the lifting-surface theory, its applicability is limited to high-aspect-ratio wings with sealed controls. A method for predicting the loading in the transonic range is still lacking and the wing-body interaction is not included. The Datcom method is, therefore, outdated in view of the more sophisticated engineering numerical methods available at present.

The series or kernel-function method has the traditional beauty in that only a minimal number of exact pressure functions are embedded in the solution. However, a practical limitation does exist for selecting suitable pressure functions to fit physical reality, such as the loading at the wing-body intersection. Besides that, the truncation error is always present, hence convergence appears to be a problem.

With the advent of the high-speed computers, the number of undetermined coefficients need not be so limited and consequently the pressure functions need not be assumed. The same problem can be solved by the panel influence methods. The panel method belongs also to the finite-element method in the sense that the boundary condition is only satisfied at finite points on the configuration. With the panel methods, the computation of the loading distribution on the multiple bodies (control surfaces, in particular) poses no special problem from the computational point of view, except that the convergence of the solution may not always be achieved. In order to reach a convergent solution, a dense paneling near the hinge line and side edges is required because the loadings in these regions exhibit singular behavior attributable to the linearized theory.

Since any computing machine is limited in its capacity to handle the large computational problem, a proper paneling scheme that renders the solution convergent with a limited number of panels needs to be sought. Thus, with proper paneling schemes, each numerical program may yield a solution that is the solution to the mathematical modeling of the physical problem. To enhance the solution convergence, a scheme is proposed that incorporates the pressure loading functions known from the method of asymptotic expansion near the regions of singularity--such as those on the planform leading edge, control-surface hinge line, and side edges--into the panel methods. The proposed scheme uses the kernel-function procedures and the panel methods so that the two categories serve to complement each other to yield the desired potential-flow solution. The value of such a scheme, however, can only be measured through further research and application, which is recommended.

REFERENCES

1. Hotz, A. F., "Hinge Moment Parameter Estimation Using Level 2.02 FLEXSTAB," AFFDL-TM-77-15, January 1977.
2. Dornfeld, G. M., "A Method for Predicting the Stability Characteristics of Control Configured Vehicles," Vol. IV--"FLEXSTAB 2.01.00 B-52E LAMS Demonstration Case and Results," AFFDL-TR-74-91, 1974. (AD-B005 730L)
3. Dusto, A. R., et al., "A Method for Predicting the Stability Characteristics of an Elastic Airplane," Vol. I--"FLEXSTAB 3.01.00 Theoretical Description," Boeing document D6-44361-1, May 1977; Vol. III--"FLEXSTAB 3.01.00 Program Description," Boeing document D6-44361-3, May 1977. (AD-B022 227L)
4. Peloubet, R. P., et al., "Application of Three Aeroservoelastic Stability Analysis Techniques," AFFDL-TR-76-89, September 1976. (AD-B015 902L)
5. Etkin, B., *Dynamics of Atmospheric Flight*, John Wiley & Sons, 1972.
6. Woodward, F. A., et al., "Analysis and Design of Supersonic Wing-Body Combinations, Including Flow Properties in the Near Field," Part 1, "Theory and Application," NASA CR-73106, 1967.
7. Woodward, F. A., "A Unified Approach to the Analysis and Design of Wing-Body Combinations at Subsonic and Supersonic Speeds," AIAA paper No. 68-55.
8. Woodward, F. A., "Analysis and Design of Wing-Body Combinations at Subsonic and Supersonic Speeds," *Journal of Aircraft*, Vol. 5, No. 6, pp. 528-534, 1968.
9. Manro, M. E., et al., "Transonic Pressure Measurements and Comparison of Theory to Experiment for an Arrow-Wing Configuration," Vol. III, NASA CR-132729, 1975.
10. *USAF Stability and Control DATCOM*, Flight Control Division, AFFDL, Wright-Patterson Air Force Base, Ohio, 1960.
11. Rowe, W. S., Winther, B. A., and Redman, M. C., "Predictions of Unsteady Aerodynamic Loadings Caused by Trailing Edge Control Surface Motions in Subsonic Compressible Flow," Analysis and Results, NASA CR-2003.
12. Rowe, W. S., Winther, B. A., and Redman, M. C., "Unsteady Subsonic Aerodynamic Loadings Caused by Control Surface Motions," *Journal of Aircraft*, Vol. 11, No. 1, 1974.
13. Rowe, W. S., et al., "Prediction of Unsteady Aerodynamic Loadings Caused by Leading Edge and Trailing Edge Control Surface Motions in Subsonic Compressible Flow," Analysis and Results, NASA CR-2543, 1975.
14. Landahl, M., "Pressure-Loading Functions for Oscillating Wings With Control Surfaces," *AIAA Journal*, Vol. 6, No. 2, 1968.

15. Ashley, H., and Rowe, W. S., "On the Unsteady Aerodynamic Loading of Wings With Control Surfaces," *Z. Flugwiss* 18, Heft 9/10, 1970.
16. Rubbert, P. E., et al., "A General Method for Determining the Aerodynamic Characteristics of Fan-in-Wing Configurations," Vol. 1, "Theory and Application," technical report 67-61A, USAA V LABS, 1967. (AD 667 980)
17. Rubbert, P. E., and Saaris, G. R., "Review and Evaluation of a Three-Dimensional Lifting Potential Flow Analysis Method for Arbitrary Configurations," AIAA paper No. 72-188.
18. Lamb, H., *Hydrodynamics*, Dover Publications, 1945.
19. Johnson, F. T., and Rubbert, P. E., "Advanced Panel-Type Influence Coefficient Methods Applied to Subsonic Flows," AIAA paper No. 75-50.
20. Johnson, F. T., "A General Panel Method for the Analysis and Design of Arbitrary Configurations in Subsonic Flows," Boeing document D6-43808, 1976.
21. Hammond, A. D., and Keffer, B. M., "The Effect at High Subsonic Speeds of a Flap-Type Aileron on the Chordwise Pressure Distribution Near Midsemispan of a Tapered 35° Sweptback Wing of Aspect Ratio 4 Having NACA 65A006 Airfoil Section," NACA RM L53C23, 1953.
22. Kopal, Zdeněk, *Numerical Analysis*, Chapman and Hall, London, 1955.
23. Medan, R. T., "Aerodynamic Loads Near Cranks, Apexes and Tips of Thin, Lifting Wings in Incompressible Flow," AGARD-CP-204, September 1976.
24. Ashley, H., "Some Considerations Relative to the Predictions of Unsteady Airloads on Lifting Configurations," *Journal of Aircraft*, Vol. 8, No. 10, 1971.
25. Woodward, F. A., "An Improved Method for the Aerodynamic Analysis of Wing-Body-Tail Configurations in Subsonic and Supersonic Flow," Part I, "Theory and Application," NASA CR-2228, May 1973.
26. Medan, R. T., "Steady, Subsonic, Lifting Surface Theory for Wings With Swept, Partial Span, Trailing Edge Control Surfaces," NASA TN D-7251, 1973.
27. Verna, C., "Experimental Development of a Technique for Modeling High-Lift Configurations in Three-Dimensional Potential Flow Programs," Boeing document D6-45114, 1977.
28. Brune, G. W., et al., "A Three-Dimensional Solution of Flows Over Wings With Leading Edge Vortex Separation," Part I, NASA CR-132709, 1975.
29. Johnson, F. T., et al., "An Improved Method for the Prediction of Completely Three-Dimensional Aerodynamic Load Distributions of Configurations With Leading Edge Vortex Separation," AIAA paper No. 76-417.

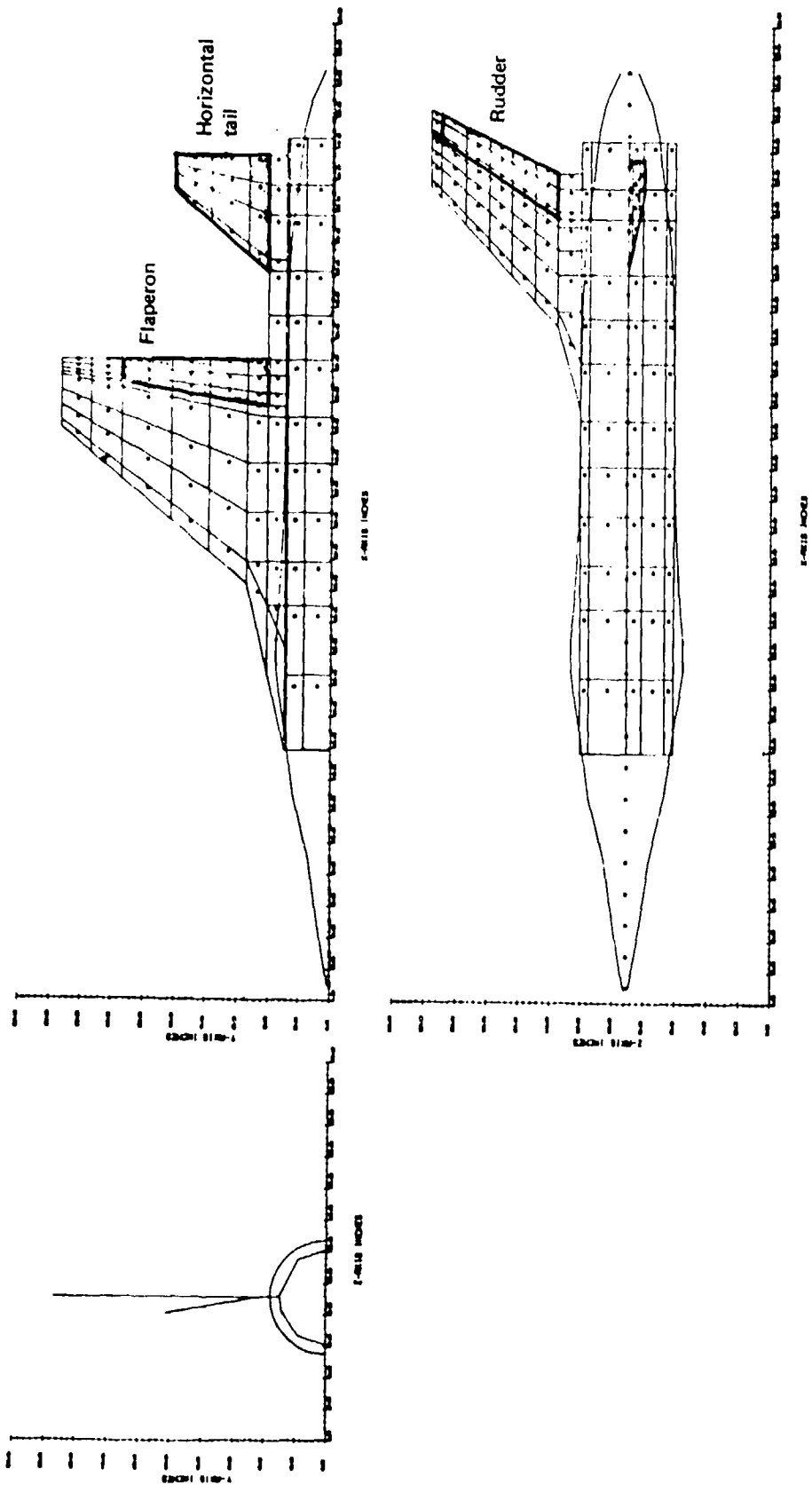


Figure 1. YF-16 Model With Basic Paneling

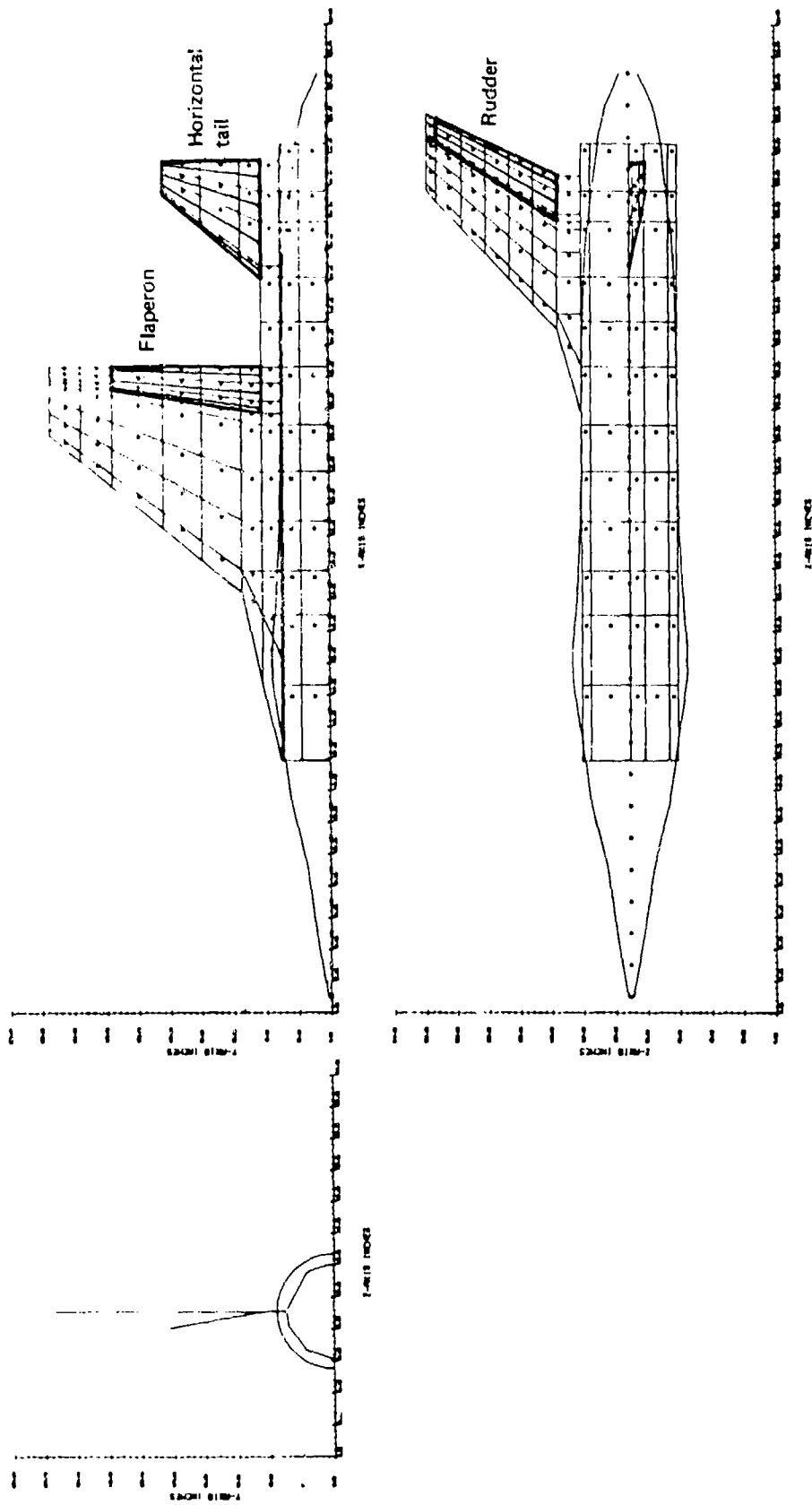


Figure 2. YF-16 Model With Low-Density Near-Field/Far-Field Simulation

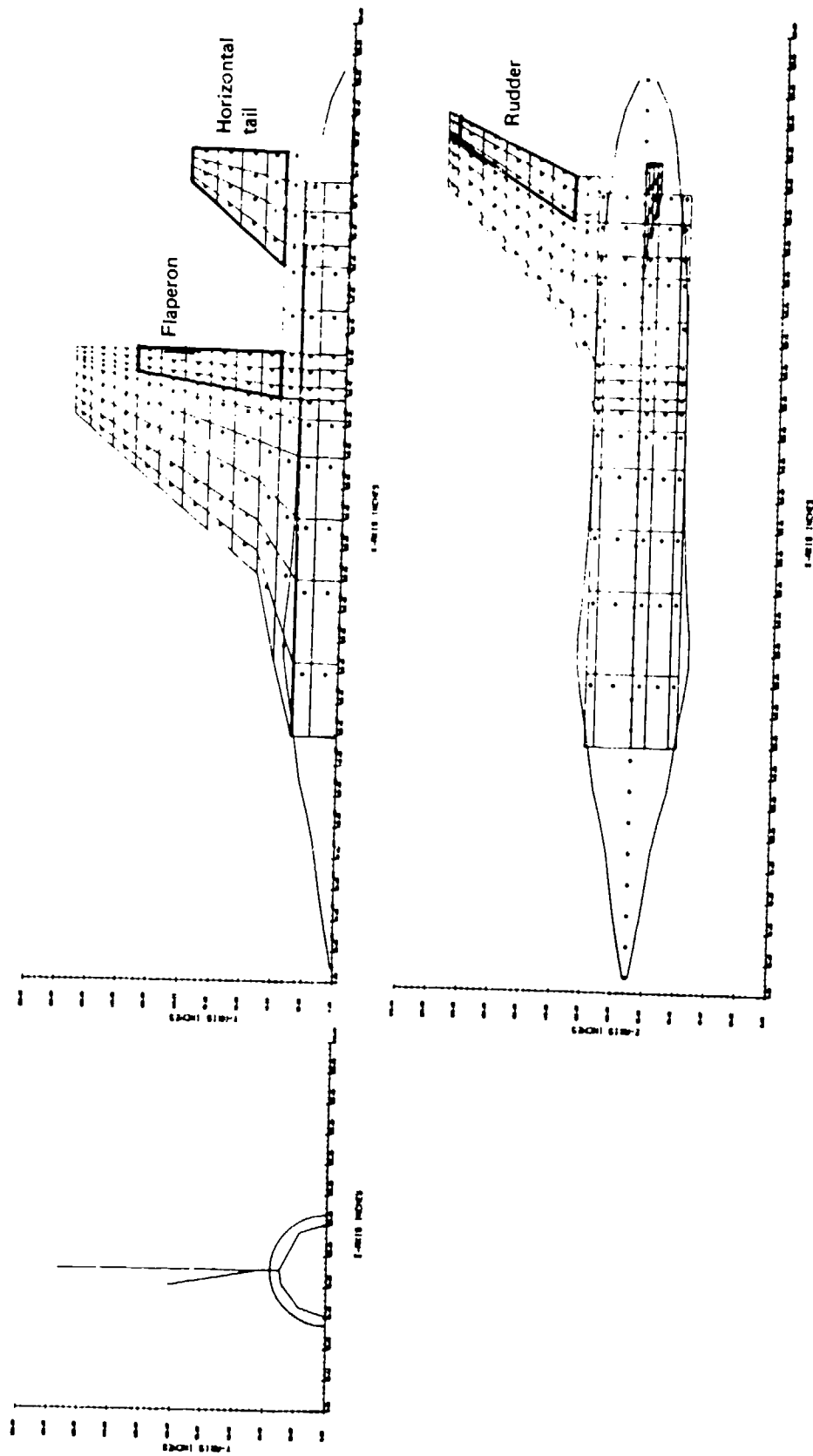
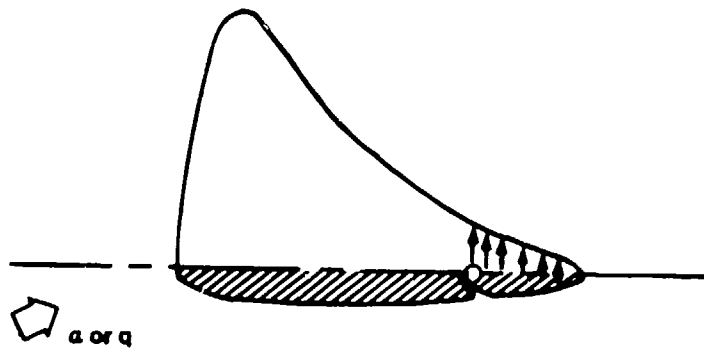
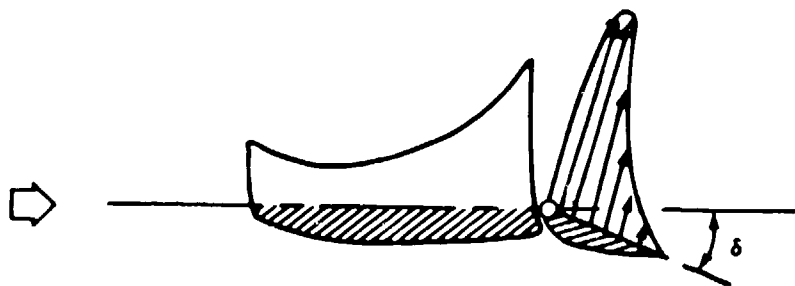


Figure 3. YF-16 Model With "Improved" Paneling



(a) Control surface not deflected



(b) Control surface deflected

Figure 4. Typical Loading on Control Surface

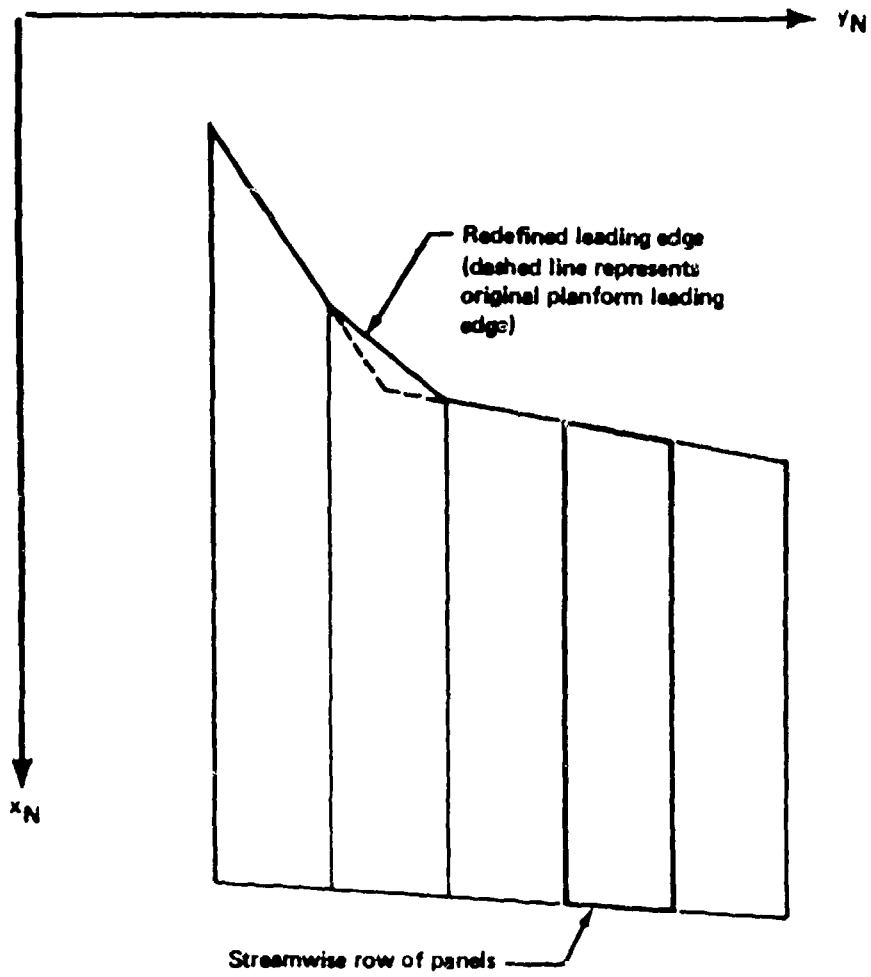
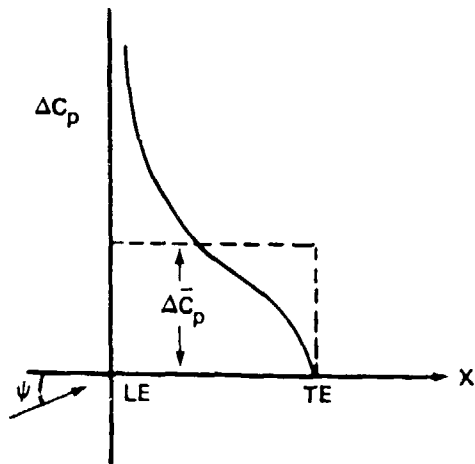
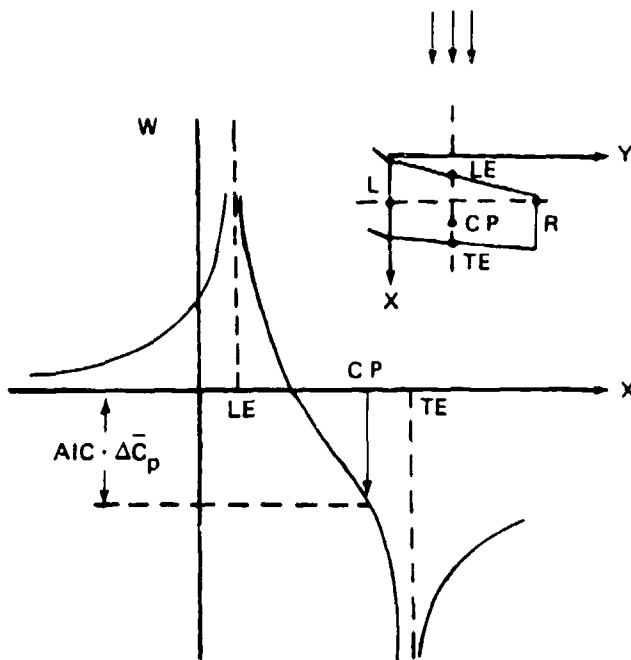


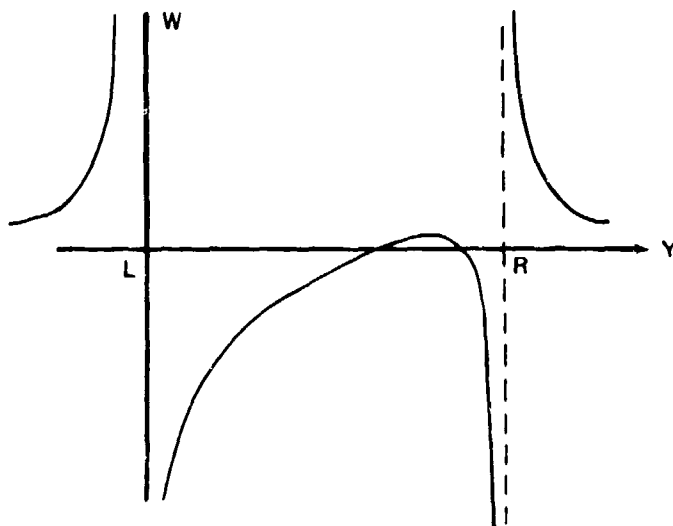
Figure 5. Breakpoint Edge Redefinition



(a) Typical chordwise load distribution of a lifting surface



(b) Chordwise downwash distribution of a constant-pressure panel



(c) Spanwise downwash distribution of a constant-pressure panel

Figure 6. Typical Load and Downwash Distributions on a Constant-Pressure Panel and on a Wing in Subsonic Flow

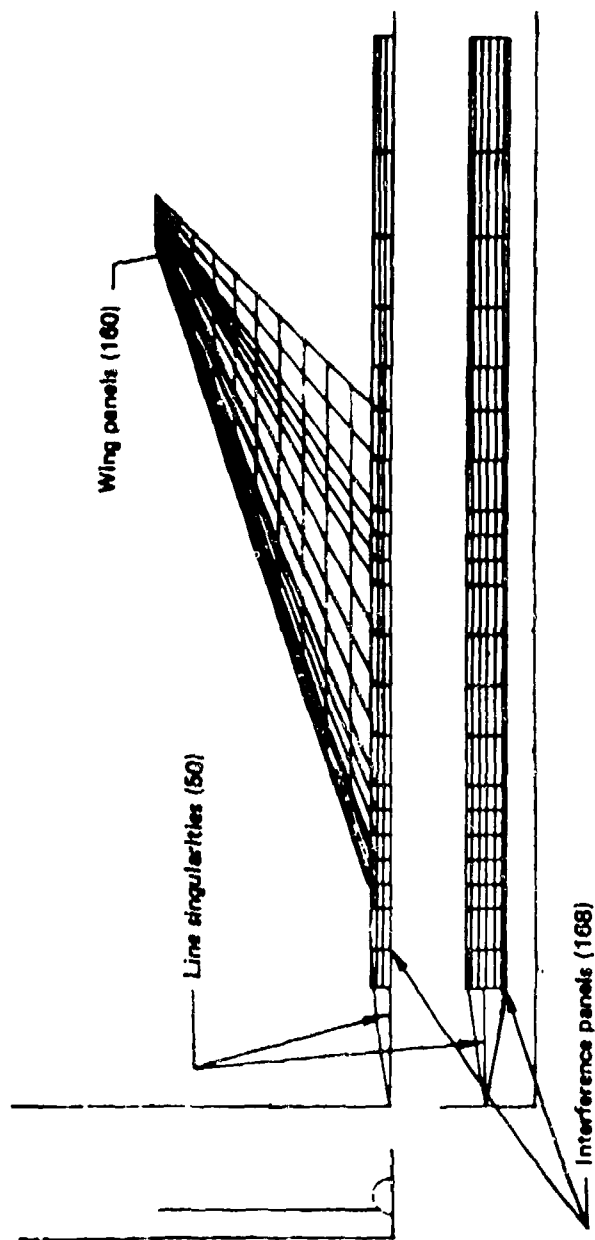
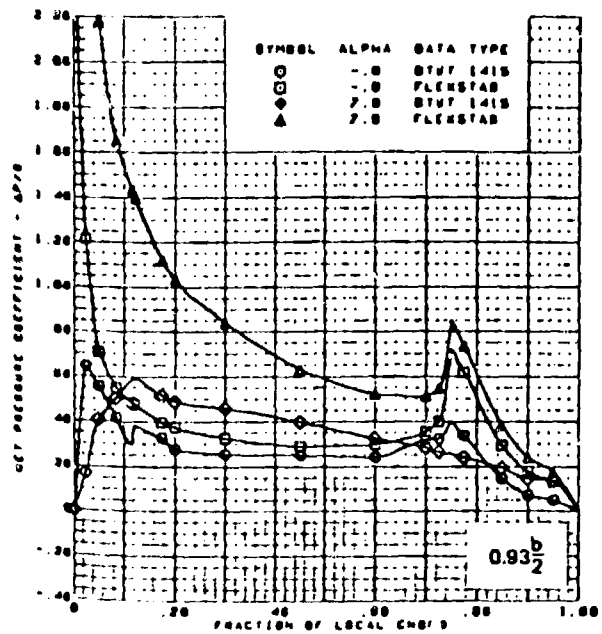
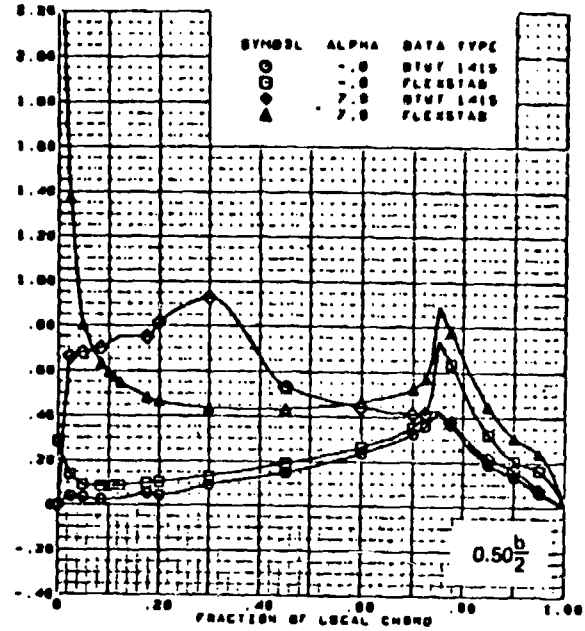
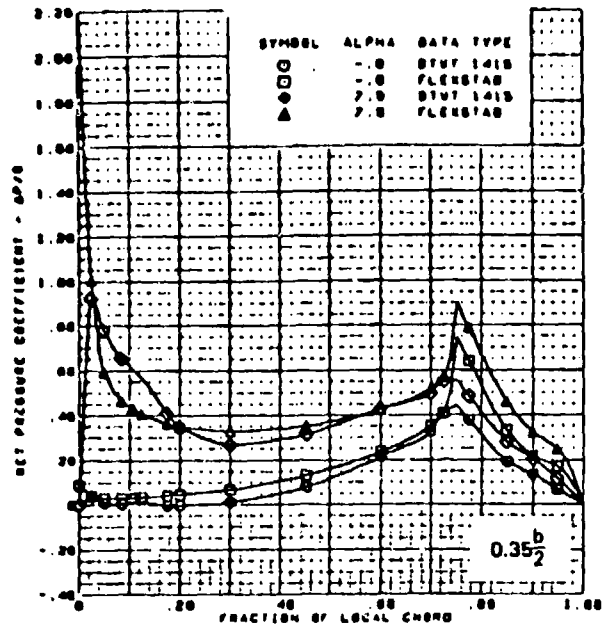


Figure 7. Arrangement of Panels Used for FLEXSTAB Analysis of Arrow-Wing-Body Configuration



M = 0.85
 Flat wing, round LE
 LE deflection, full span = 0.0 deg
 TE deflection, full span = 8.3 deg

Figure 8. Load Distributions on the Arrow-Wing-Body Configuration—FLEXSTAB Versus Experiment

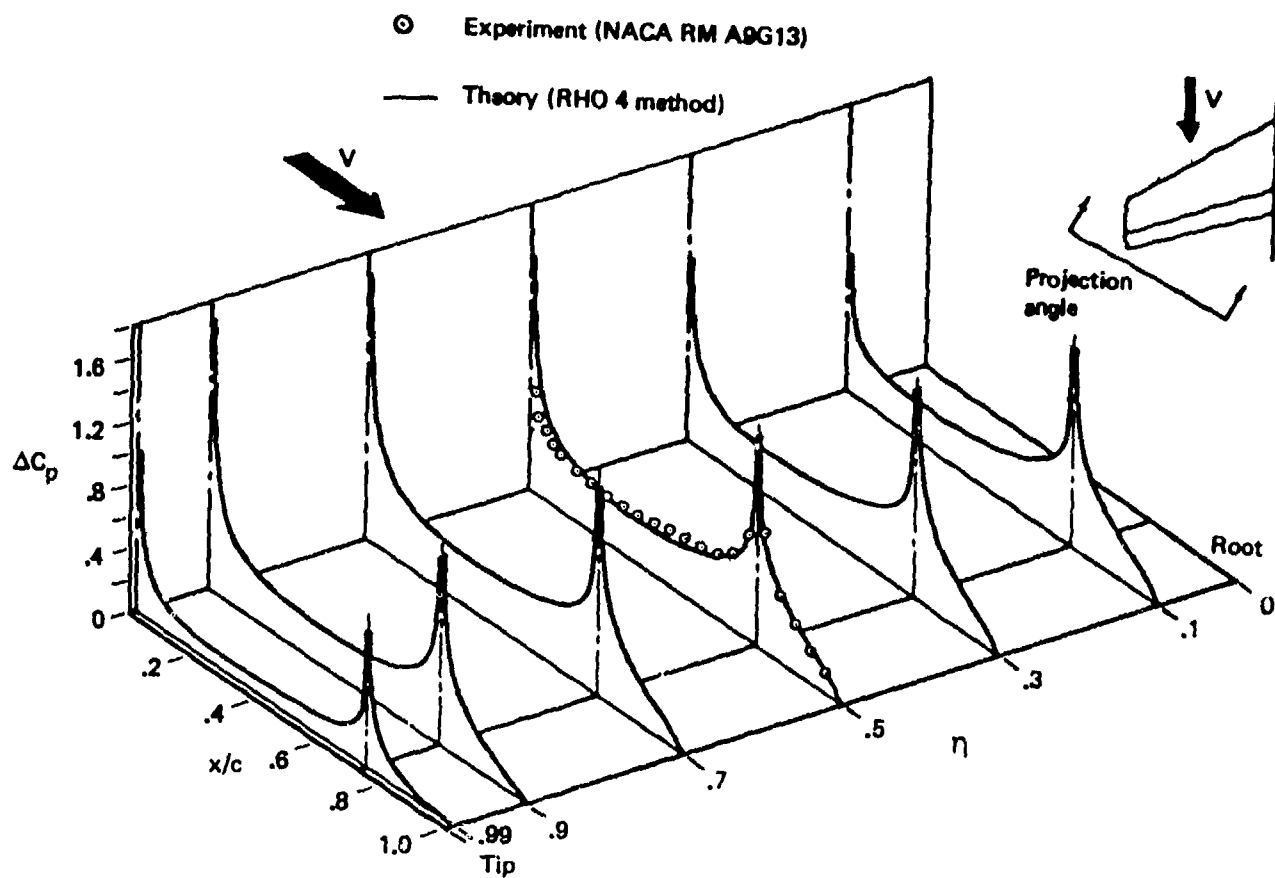


Figure 9. Theoretical and Experimental Chordwise Load Distributions for a Full-Span Flap Deflected by $\delta = 10$ deg at $\alpha = 0$ deg and $M = 0.21$

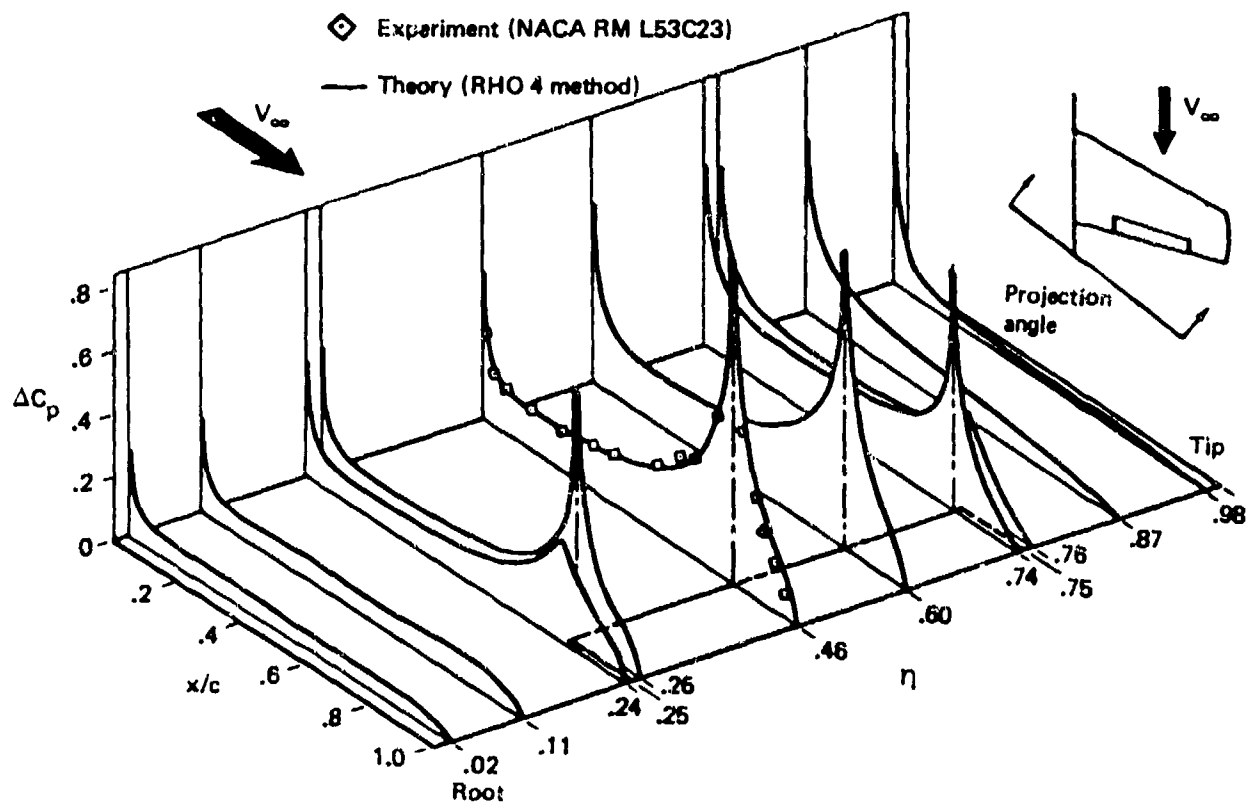


Figure 10. Theoretical and Experimental Load Distributions for Partial-Span Flap Deflected by $\delta = 10$ deg at $\alpha = 0$ deg and $M = 0.60$

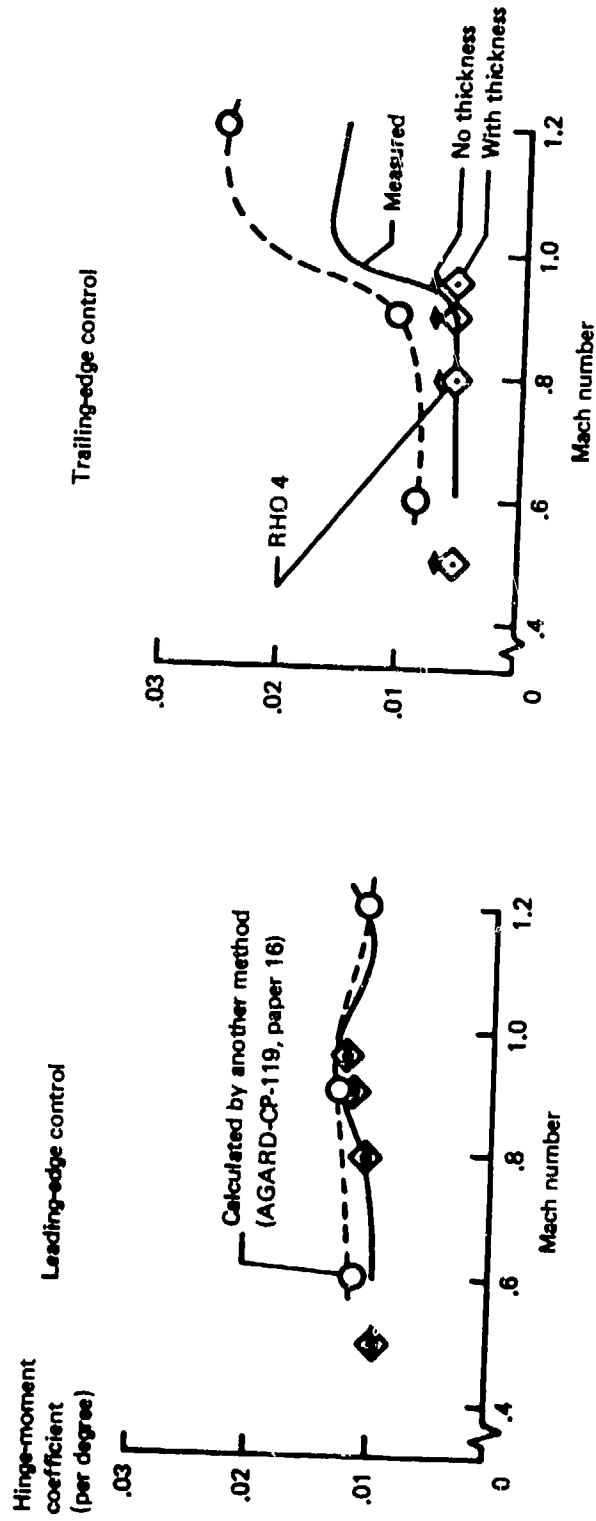
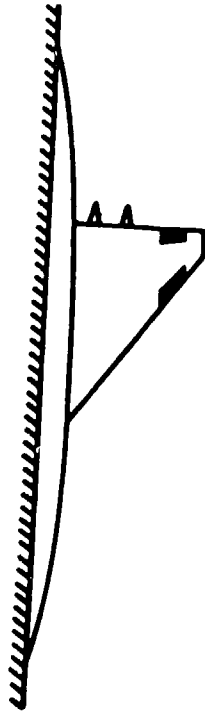


Figure 11. Comparison of Measured and Calculated Static Hinge-Moment Coefficients

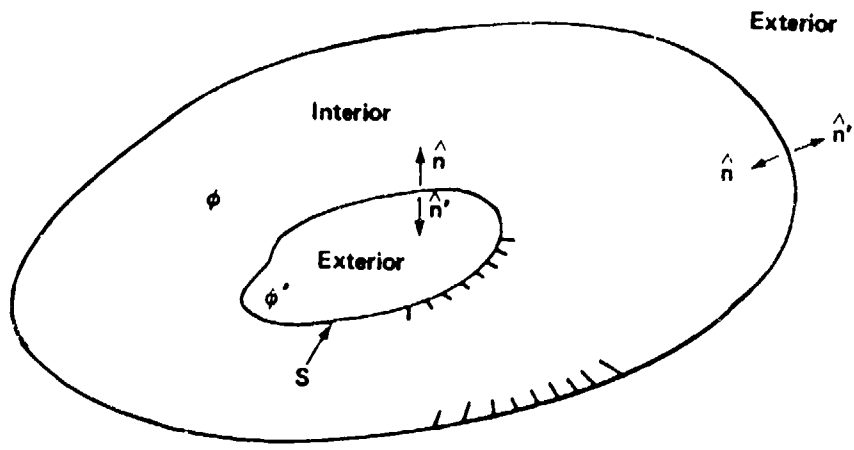


Figure 12. Potential-Flow Regions

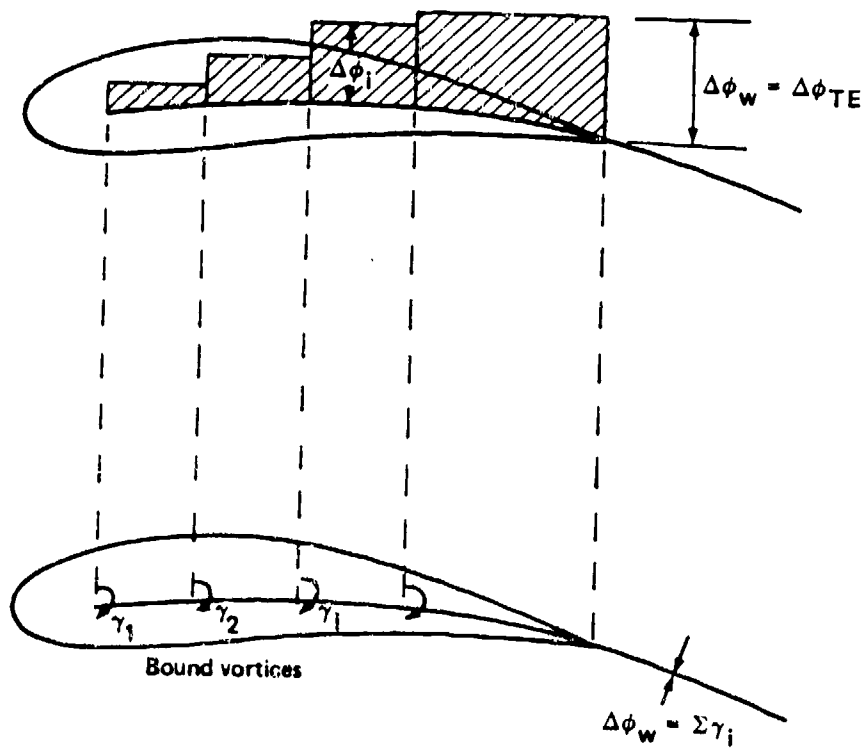


Figure 13. Internal Vortex Strength

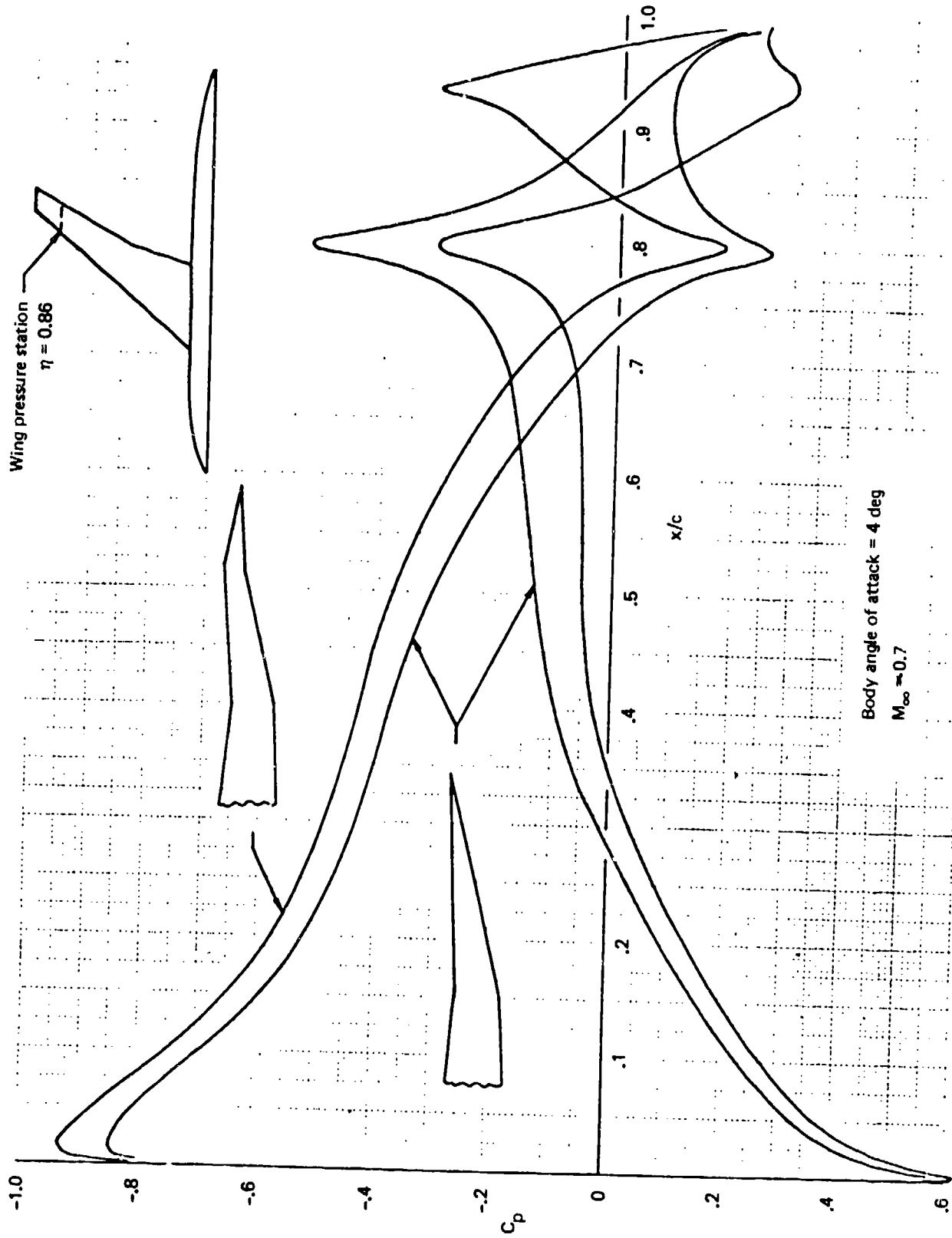


Figure 14. Outboard Boeing 747 Wing Pressure Distributions for Two Aileron-Tab Configurations

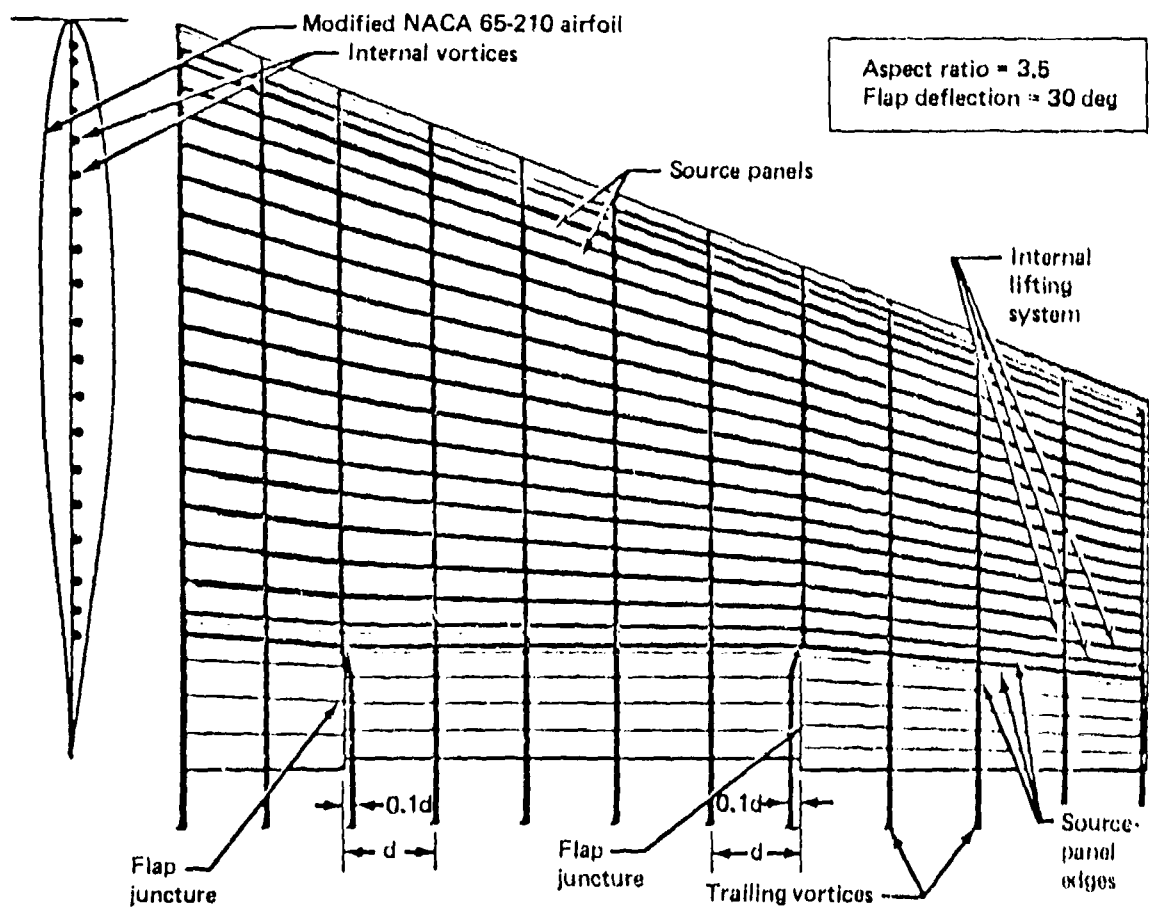


Figure 15. Source-Panel and Internal Vortex Arrangement on NASA Model Wing With Deflected Flap

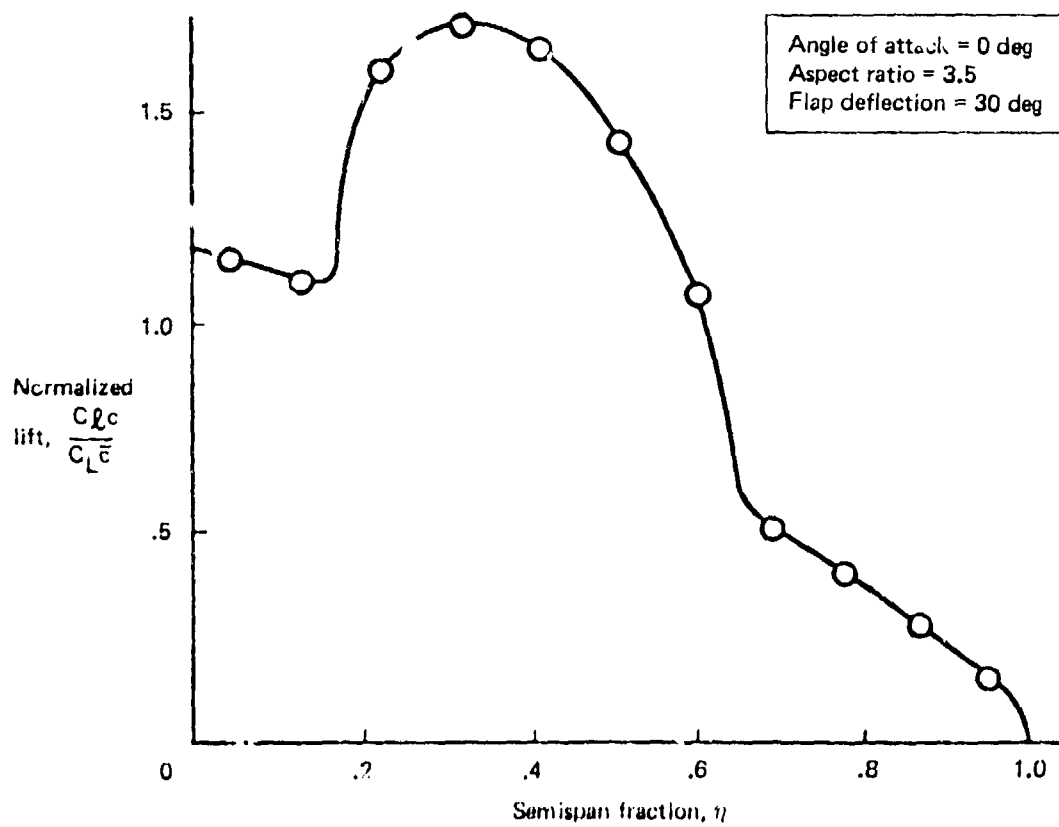
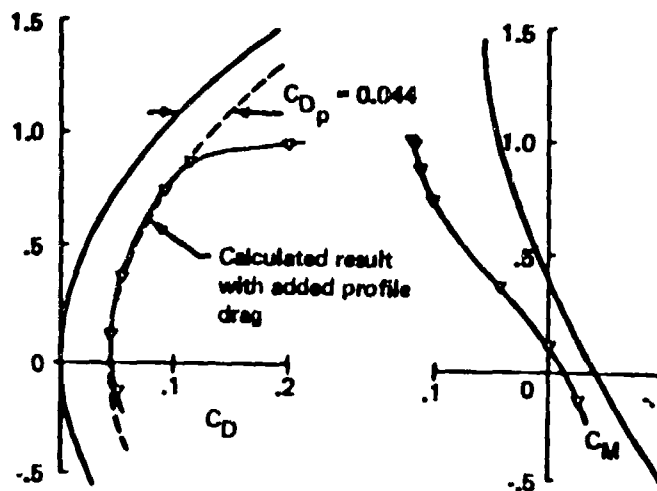
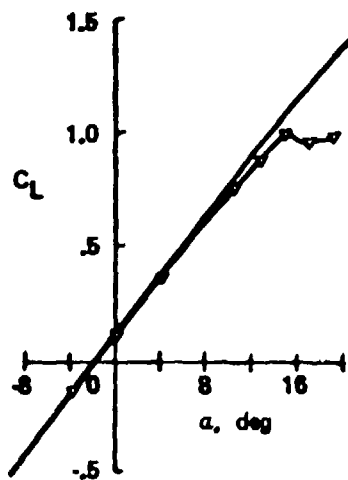
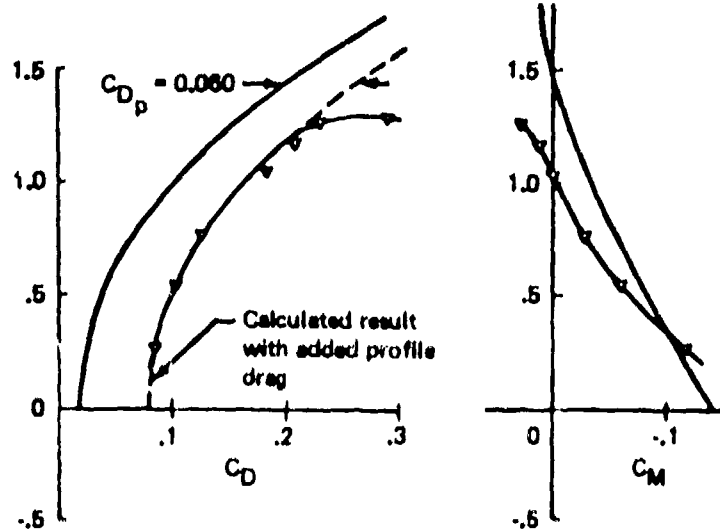
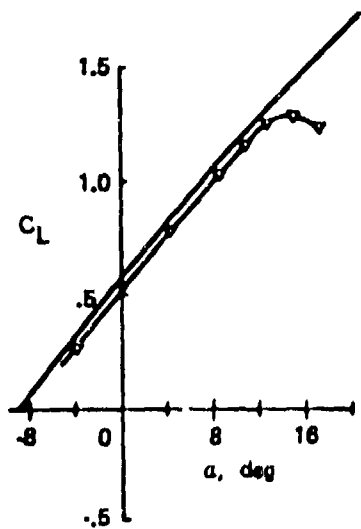


Figure 16. Spanwise Load Distribution on NASA Model Wing



(a) Flap deflection = 0 deg



(b) Flap deflection = 30 deg

$$S_f = 6.1 \times 10 \text{ in}^2$$

$$C_r = 137 \text{ in}$$

Moment ref. coordinates

$$x_r = 88.4 \text{ in}$$

$$y_r = 0 \text{ in}$$

$$z_r = -24 \text{ in}$$

— Calculated results (wing)

- - - Experimental results (wing, body)

(Ref. NASA TN D-1650)

Figure 17. Comparison of Theoretical Force and Moment Results With Experimental Data on NASA Model Wing

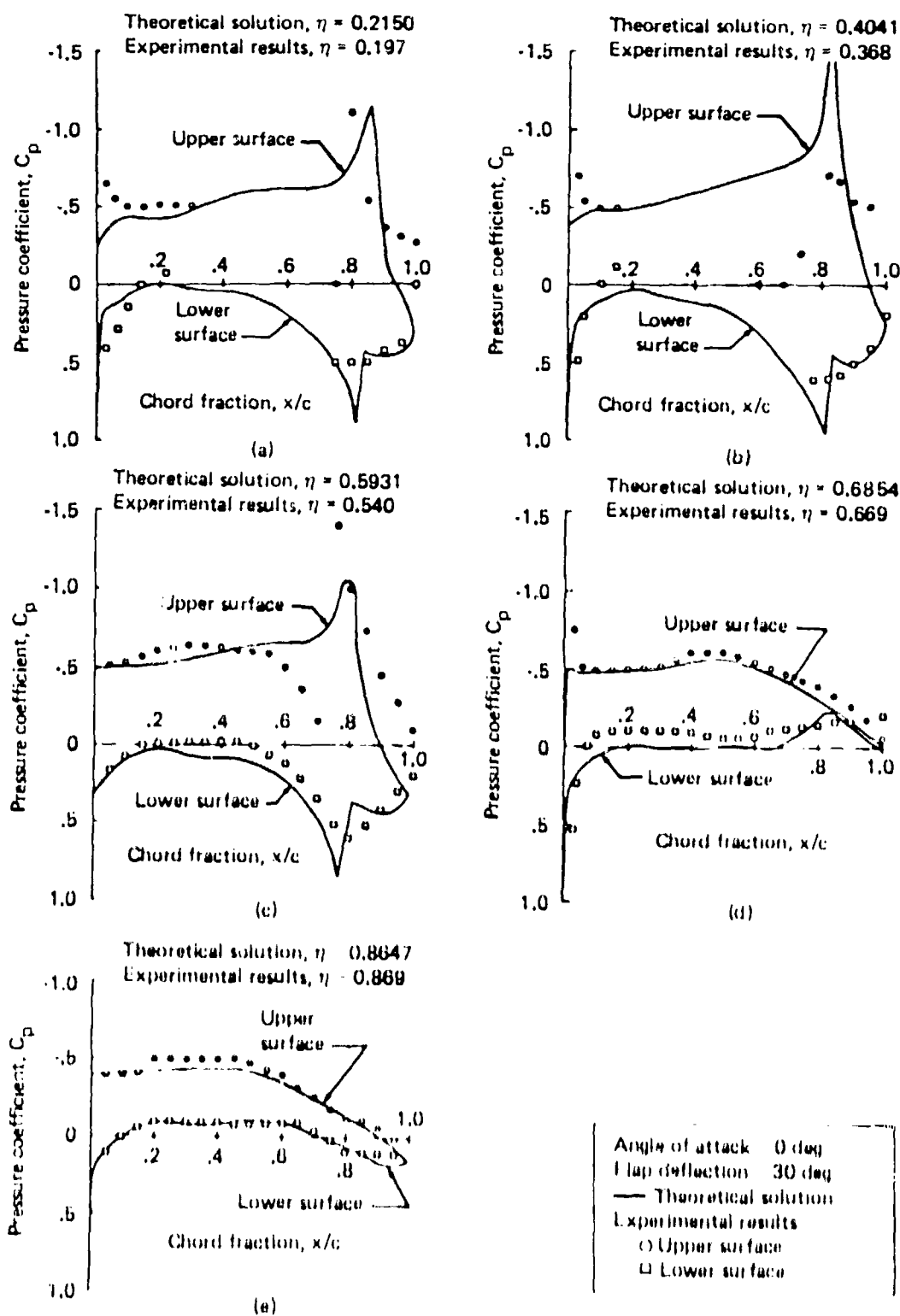
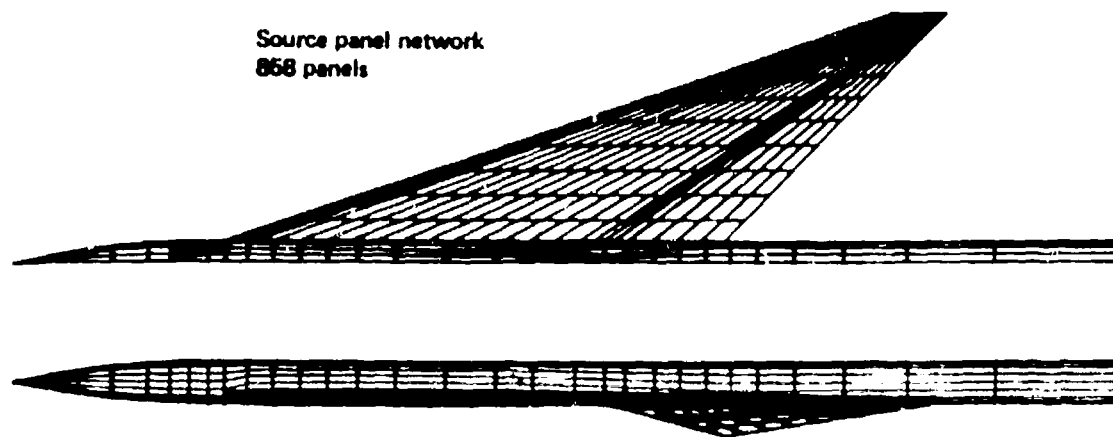


Figure 18. Comparison of Theoretical and Experimental Pressure Distributions on NASA Model Wing



Vortex network
207 panels

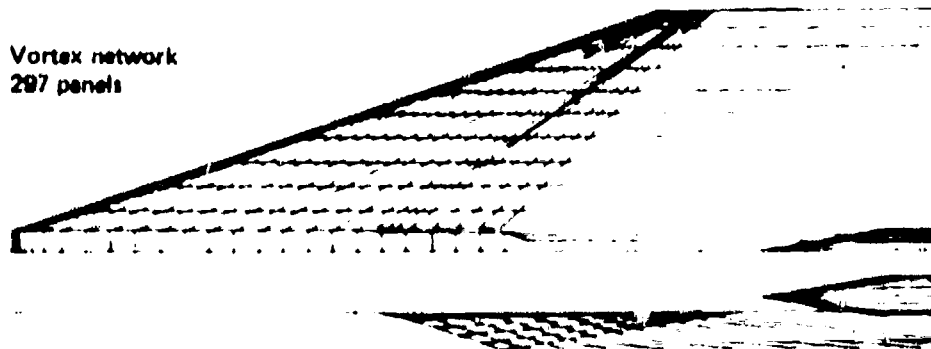


Figure 19. Arrangement of Panels Used for TEA 230 Analysis of Arrow-Wing-Body Configuration

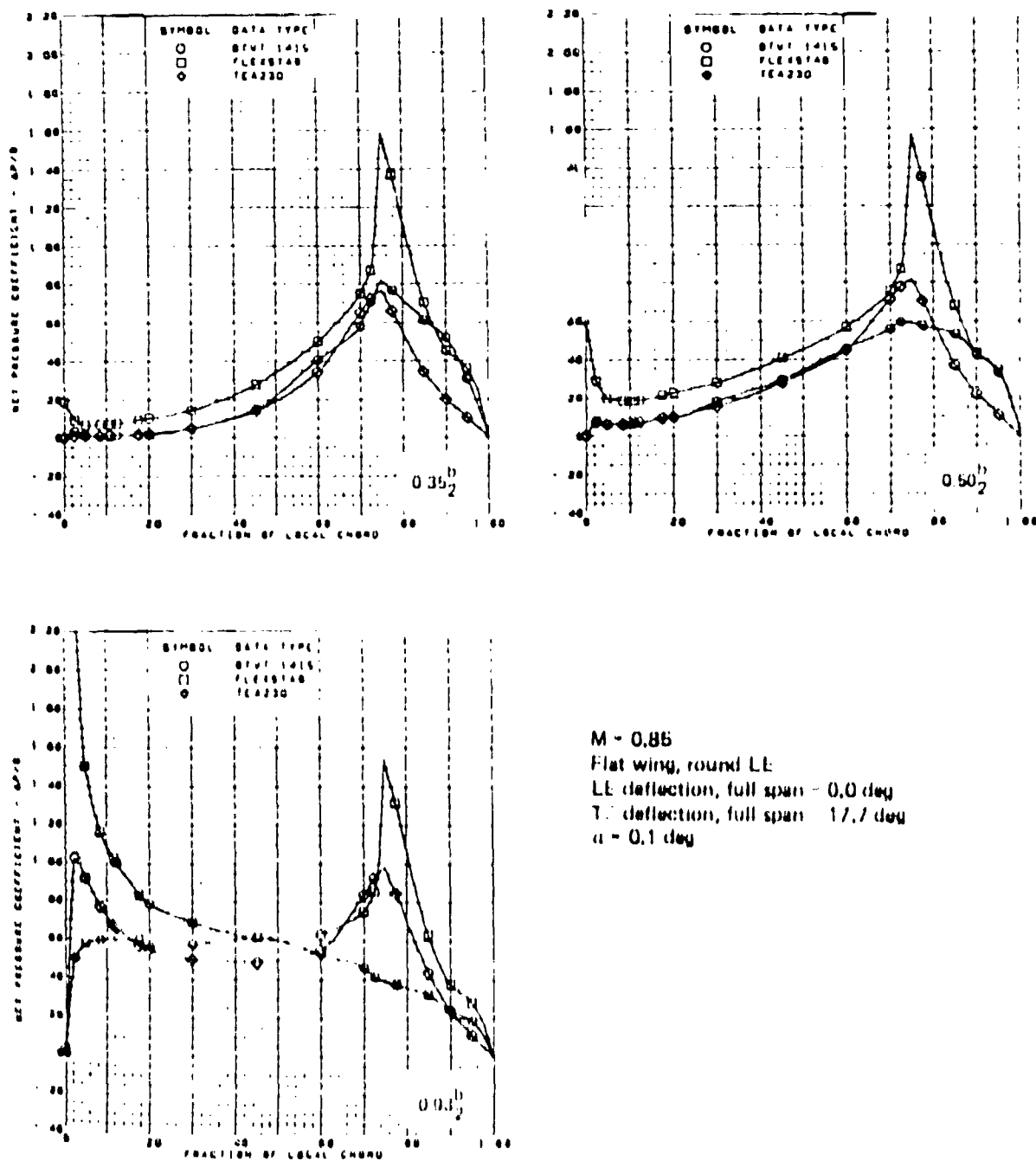


Figure 20. Load Distributions on the Arrow-Wing-Body Configuration TEA 230, FLEXSTAB Versus Experiment

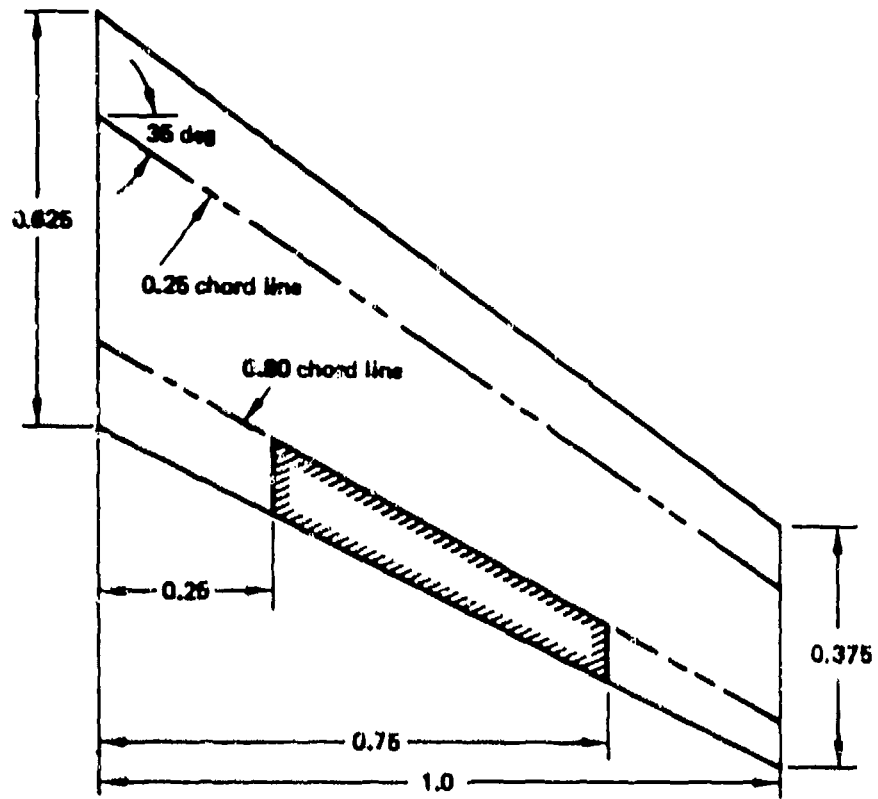


Figure 21. A 35-deg Sweptback Wing With Control Surface

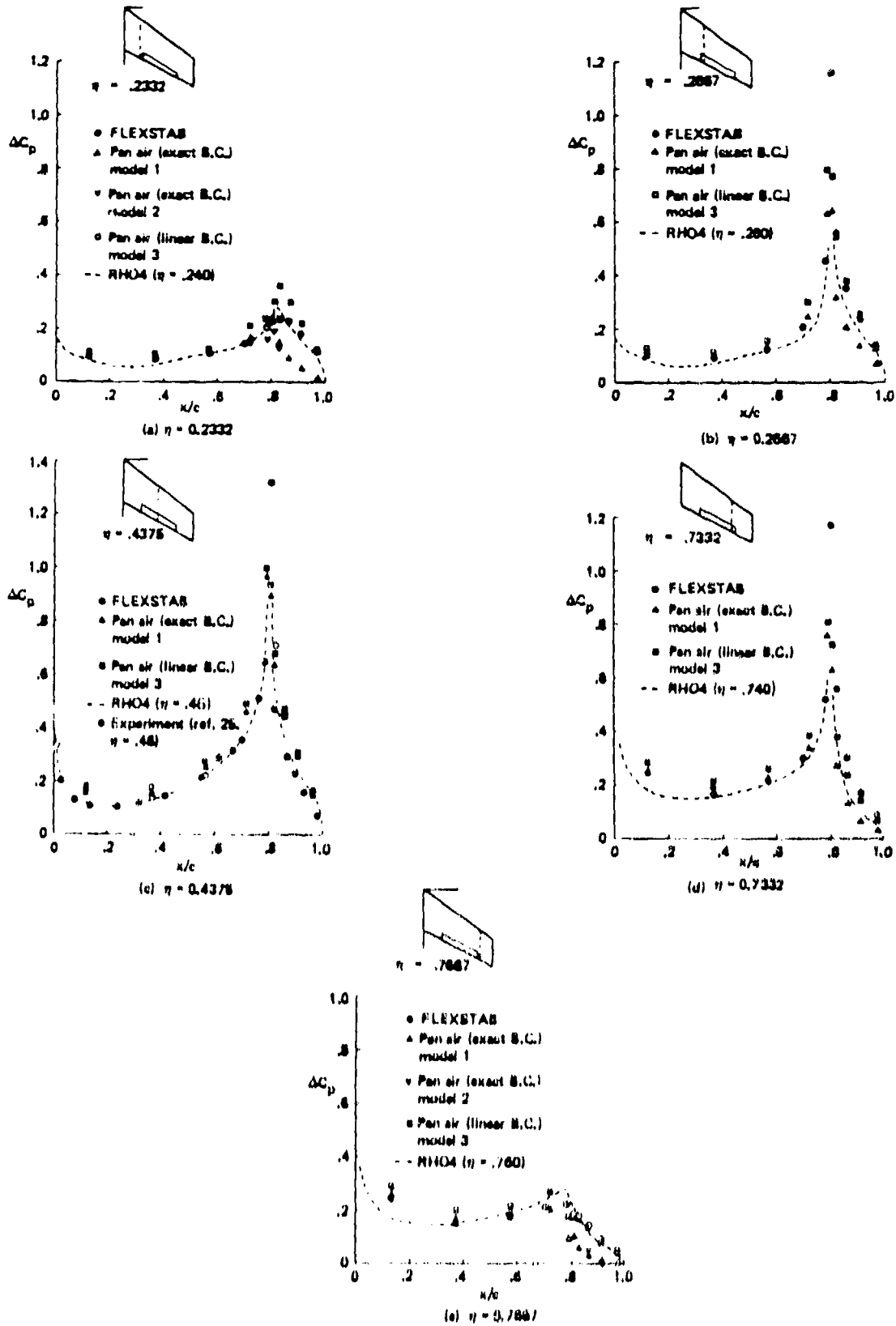


Figure 22. Theoretical Lift Distributions on NASA Wing

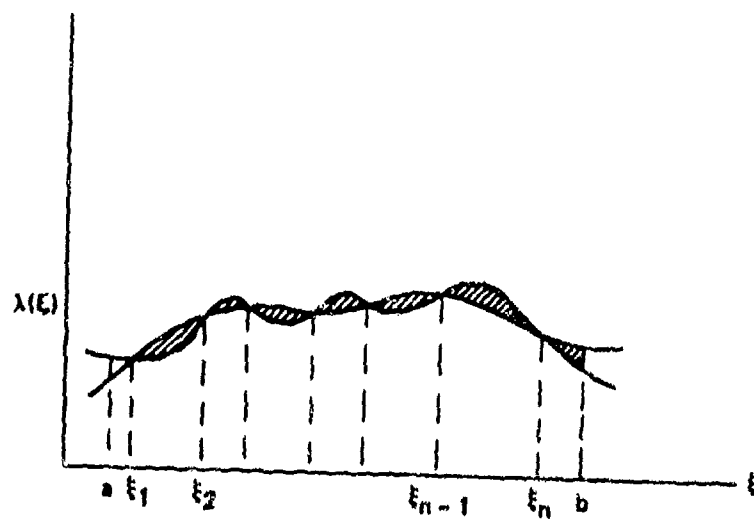


Figure 23. Graphic Illustration of Equation (54)

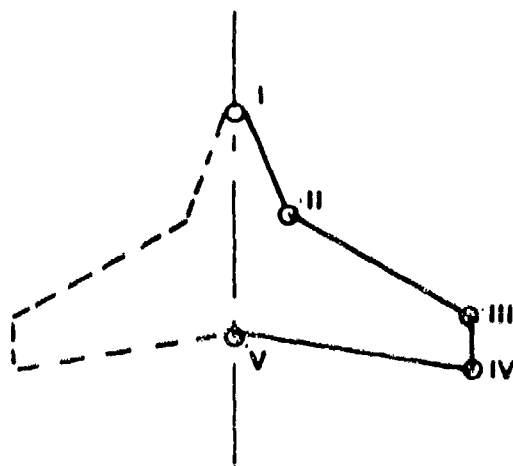


Figure 24. Platform Breakpoints

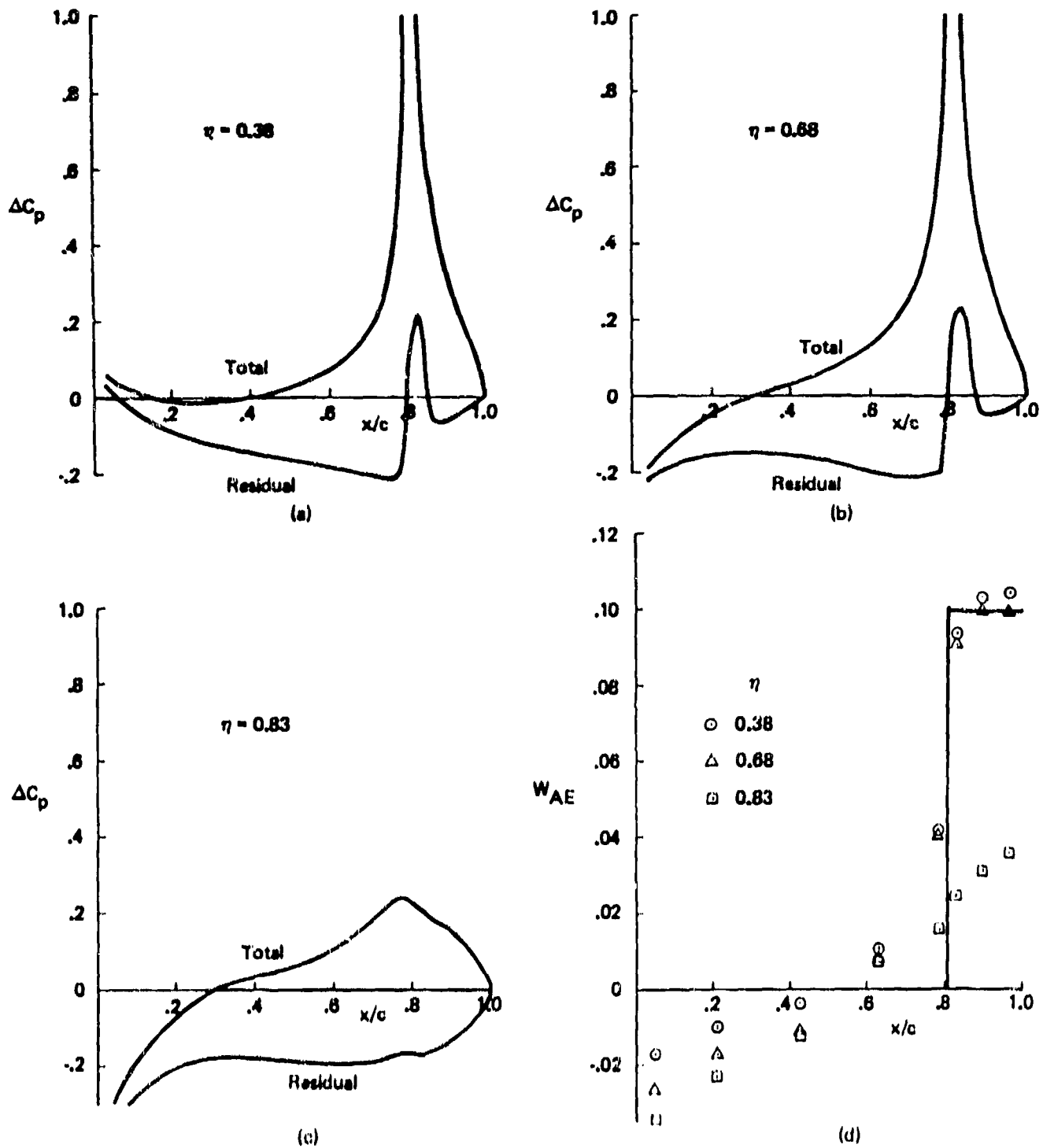


Figure 25. Load and Downwash Distributions on YF-16 Wing With Control Surface

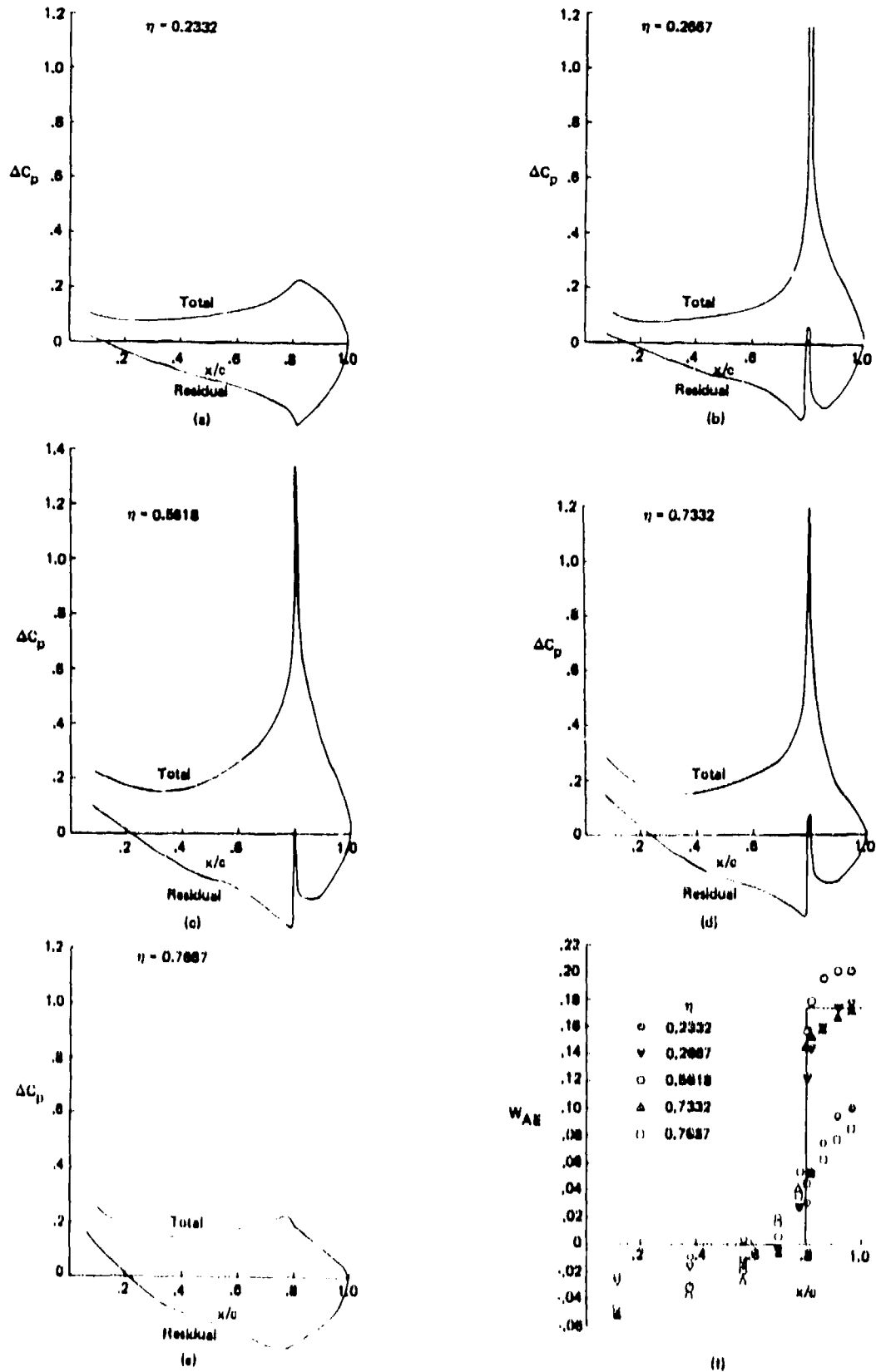


Figure 26. Load and Downwash Distributions on a 35-degree Sweptback Wing With Control Surface

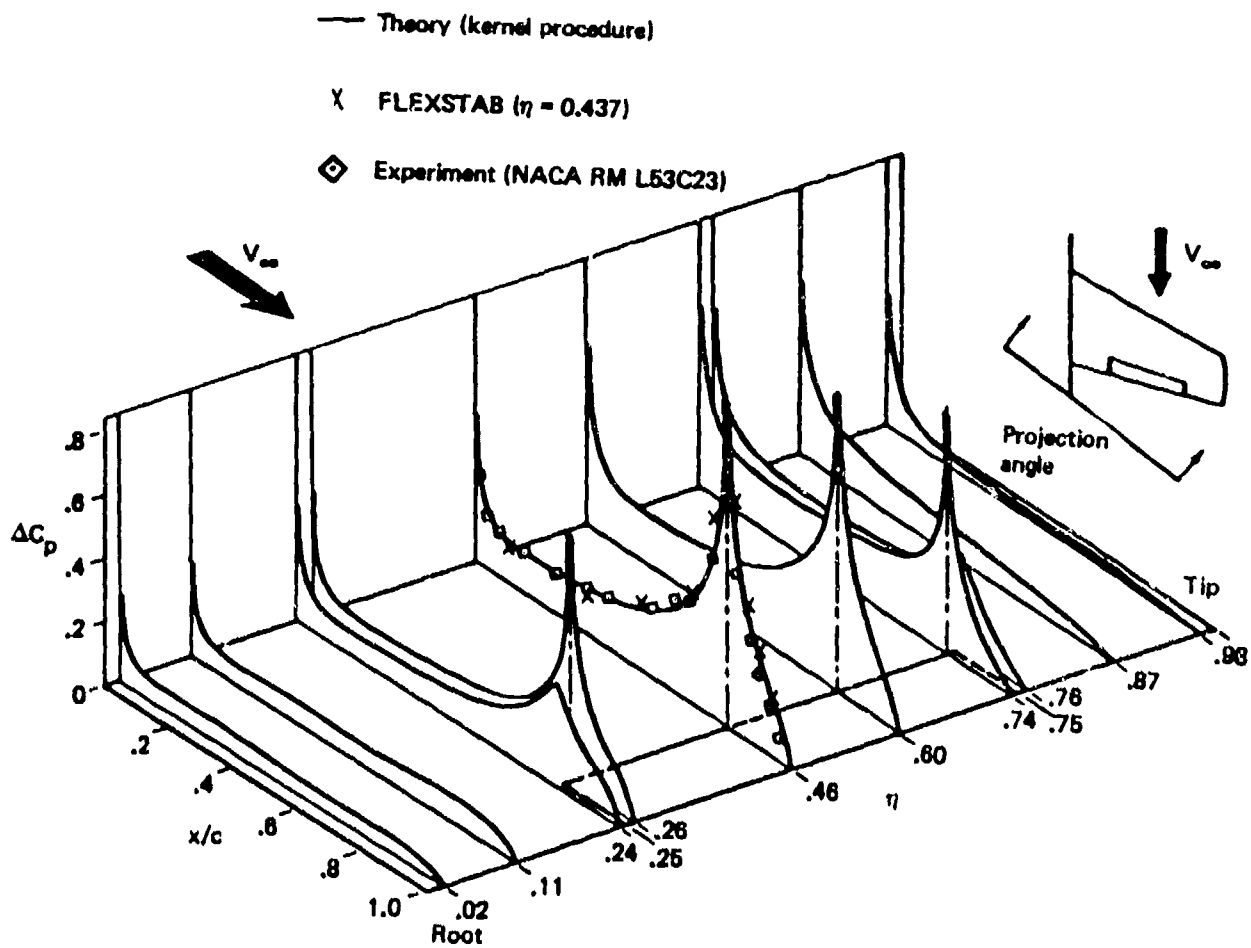


Figure 27. Theoretical and Experimental Pressure Distributions for Partial-Span Flap Deflected by $\delta = 10$ deg at $\alpha = 0$ deg and $M = 0.60$

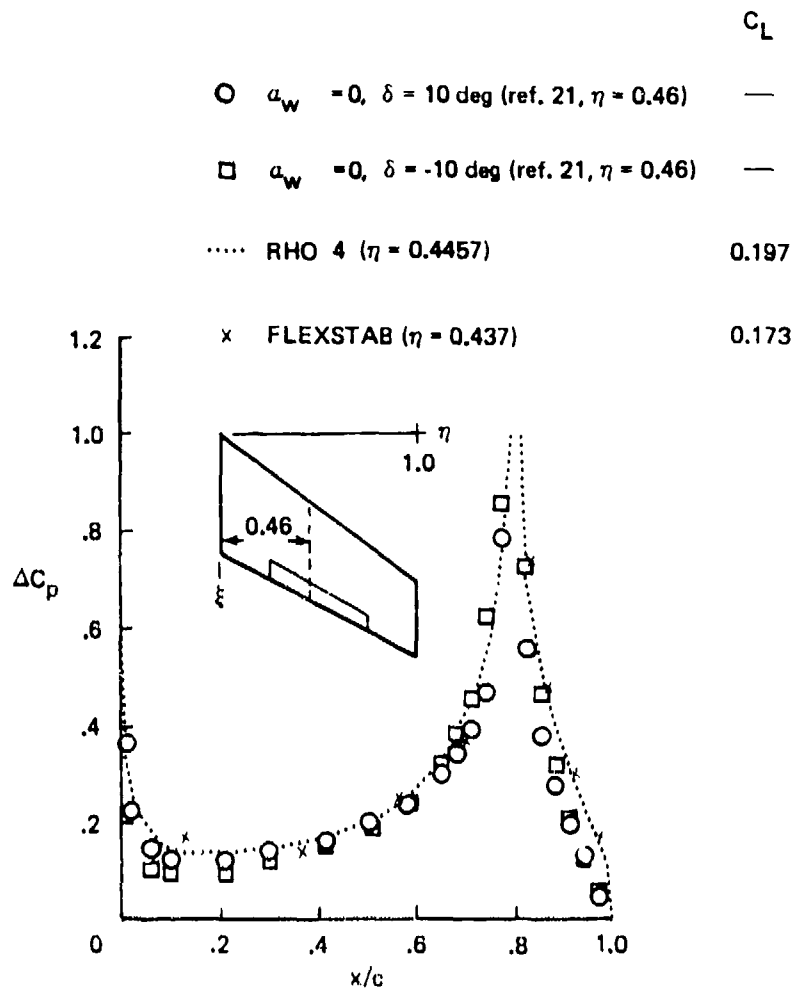


Figure 28. Comparison of Experimental and Calculated Lifting-Pressure Distributions on a Sweptwing With Partial-Span Flap at $M = 0.60$

TABLE 1
SD&SS RUNS FOR CORRELATION AND HINGE-MOMENT IMPROVEMENT (ITEM 2.0)

Run No.	Paneling scheme	Elastic option	Altitude	Near/far option	Notes
1	Basic	Residual-elastic	SL	No	Correlation with AFFDL Flaperon hinge-line location incorrect to compare with AFFDL results
2	Basic	Residual-elastic	15,000 ft	No	
3	Basic	Rigid	15,000 ft	On flaperon only	
4	Basic	Rigid	SL	No	Redefine certain thin bodies to improve model Flaperon hinge location correct
5	Basic and strake	Rigid	SL	No	
6	Basic	Rigid	SL	On flaperon only	
7	Low density	Residual-elastic	SL	No	
8	Optimum	Rigid	SL	No	

TABLE 2
ANTISYMMETRIC STABILITY AND CONTROL DERIVATIVES COMPARISON OF FLEXSTAB
AND WIND TUNNEL DATA (FROM REF. 4), BASIC PANELED MODEL

Derivative (per rad)	Wind tunnel			FLEXSTAB (Boeing)		
	Rigid	Flexible		Rigid	Flexible	
		SL	15,000 ft		SL	15,000 ft
$C_{Y\beta}$	-1.243	-1.112	-1.121	-0.8221	-0.7353	-0.7637
$C_{n\beta}$.260	.239	.256	.1919	.1462	.1619
$C_{l\beta}$	-.1157	-.080	-.086	-.0761	-.0869	-.0796
C_{Yp}	.90	.78	.83	.9762	.8352	.8813
C_{np}	-.456	-.40	-.428	-.4667	-.4609	-.4181
C_{lp}	.171	.135	.165	.1040	.1171	.1301
$C_{Y\dot{\beta}}$.014	.013	.014	-.0295	-.0119	-.0111
$C_{n\dot{\beta}}$	-.004	-.003	-.003	.0213	.0173	.0191
$C_{l\dot{\beta}}$	-.325	-.26	-.28	-.3423	-.3924	-.4013
$C_{Y\delta_a}$	0	0	0	.1637	.0994	.1203
$C_{n\delta_a}$	-.038	-.036	-.0355	-.0637	-.0351	-.0422
$C_{l\delta_a}$	-.1339	-.0770	-.0922	-.2188	-.1494	-.1770
$C_{Y\delta_r}$.209	.1060	.126	.4115	.2441	.299
$C_{n\delta_r}$	-.1066	-.0673	-.079	-.2249	-.1360	-.1661
$C_{l\delta_r}$.0355	.0180	.022	.0579	.0449	.0476
α	1 deg			1.3259 deg	1.3259 deg	1.9231 deg

TABLE 3
COMPARISON OF HINGE-MOMENT DERIVATIVES—AFFDL AND BOEING, BASIC
PANELED MODEL

Control surface	Derivative (per rad)	AFFDL			Boeing		
		Rigid	Flexible		Rigid	Flexible	
			15,000 ft	SL		15,000 ft	SL
Flaperon	$C_{h\alpha}$	-0.000367	—	—	-0.000367	—	—
	$C_{h\hat{q}}$	- .00230	—	—	- .00230	—	—
	$C_{h\delta}^S$	- .000434	—	—	- .000434	—	—
	$C_{h\hat{u}}$	- .000045	—	—	- .000045	—	—
	$C_{h\hat{a}}$	- .52434	—	—	- .52424	—	—
	$C_{h\hat{q}}$	- .004019	—	—	- .004019	—	—
	$C_{h\delta}^S$	- .000015	—	—	- .0000147	—	—
	$C_{h\beta}$.000055	0.000064	0.000071	.000055	0.000046	0.000041
	$C_{h\hat{p}}$	- .00009	- .000067	- .000048	- .00009	- .000141	- .000182
	$C_{h\hat{r}}$	- .000027	- .000042	- .000053	- .000027	- .000016	- .000016
	$C_{h\delta}^A$	- .000249	- .000242	- .000237	- .000249	- .000141	- .000076
	$C_{h\hat{\beta}}$	- .004092	- .003921	- .004011	- .004092	- .003988	- .004177
	$C_{h\hat{p}}$	- .000324	- .000312	- .000305	- .000324	- .000302	- .000287
	$C_{h\hat{r}}$.000063	.000061	.000060	.000063	.000061	.000060
	$C_{h\delta}^A$	- .000013	- .000012	- .000012	- .000013	- .000012	- .000010

TABLE 3 (CONTD)

COMPARISON OF HINGE-MOMENT DERIVATIVES—AFFDL AND BOEING,
BASIC PANELED MODEL

Control surface	Derivative (per rad)	AFFDL			Boeing		
		Rigid	Flexible		Rigid	Flexible	
			15,000 ft	SL		15,000 ft	SL
Horizontal tail	$C_{h\alpha}$	0.001921	-	-	0.001921	-	-
	$C_{h\hat{\alpha}}$	-.02255	-	-	-.02255	-	-
	$C_{h\delta}^S$	-.004901	-	-	-.004901	-	-
	$C_{h\hat{\alpha}}$	-.000848	-	-	-.000891	-	-
	$C_{h\hat{\alpha}}$	-8.05998	-	-	-8.05993	-	-
	$C_{h\hat{\alpha}}$	-.106008	-	-	-.106006	-	-
	$C_{h\delta}^S$	-.000144	-	-	-.000144	-	-
	$C_{h\beta}$.001621	0.002049	0.002433	.001621	0.002283	0.002857
	$C_{h\hat{\rho}}$.000605	.000939	.001357	.000604	.001071	.001547
	$C_{h\hat{\rho}}$	-.002859	-.003071	-.003258	-.002643	-.003145	-.003536
	$C_{h\delta}^A$	-.003840	-.004670	-.005444	-.003846	-.005278	-.006518
	$C_{h\hat{\beta}}$.223056	.195740	.181482	.223054	.176564	.144711
	$C_{h\hat{\rho}}$	-.004839	-.005186	-.005513	-.004838	-.005299	-.005722
	$C_{h\hat{\rho}}$	-.003988	-.003367	-.002904	-.003897	-.003001	-.002242
	$C_{h\delta}^A$	-.000127	-.0001192	-.000106	-.000127	-.0001113	-.000090

TABLE 3 (CONCLUDED)
COMPARISON OF HINGE-MOMENT DERIVATIVES—
AFFDL AND BOEING, BASIC paneled MODEL

Control surface	Derivative (per rad)	AFFDL			Boeing		
		Rigid	Flexible		Rigid	Flexible	
			15,000 ft	SL		15,000 ft	SL
Rudder	$C_{h\beta}$	0.00070	0.000794	0.000851	0.00070	0.000774	0.000826
	$C_{h\dot{\beta}}$.000132	.000099	.000068	.000132	.000094	.000062
	$C_{h\dot{\alpha}}$	- .001573	- .001579	- .001583	- .001573	- .001559	- .001558
	$C_{h\delta}$	- .002043	- .001854	- .001727	- .002043	- .001855	- .001731
	$C_{h\dot{\beta}}^A$.078782	.066570	.061809	.078782	.066945	.06235
	$C_{h\dot{\beta}}^B$.000412	.000398	.000390	.000412	.000392	.000382
	$C_{h\dot{\alpha}}^A$	- .001504	- .001254	- .001091	- .001504	- .001262	- .001102
	$C_{h\dot{\alpha}}^B$	- .00001	- .000008	- .000006	- .00001	- .000008	- .000007

TABLE 4
COMPARISON OF BOEING AND AFFDL FLAPERON HINGE-MOMENT
DERIVATIVES USING THE NEAR-FIELD/FAR-FIELD OPTION
(LOW-DENSITY PANELING) ON THE BASIC MODEL, RIGID AIRPLANE

Derivative (per rad)	AFFDL		Boeing	
	Basic	Near/far on basic	Basic	Near/far on basic
$C_{h\alpha}$	- .000367	- .000867	- .000367	- .000483
$C_{h\hat{\alpha}}$	- .00230	- .002603	- .00230	- .002235
$C_{h\delta}^S$	- .000434	- .003812	- .000434	- .0004802
$C_{h\hat{\delta}}$	- .000045	- .000136	- .000045	- .00015
$C_{h\hat{\alpha}}$	- .52434	.044515	- .52424	- .317428
$C_{h\hat{\delta}}$	- .004019	- .003542	- .004019	- .002636
$C_{h\delta}^S$	- .000015	- .000005	- .0000147	- .0000083
$C_{h\beta}$.000055	.000062	.000055	.000045
$C_{h\hat{\beta}}$	- .00009	- .000209	- .00009	- .000124
$C_{h\hat{\gamma}}$	- .000027	- .000001	- .000027	- .000032
$C_{h\delta}^A$	- .000249	- .003513	- .000249	- .000351
$C_{h\hat{\beta}}$	- .004092	- .004757	- .004092	- .003753
$C_{h\hat{\rho}}$	- .000324	- .000156	- .000324	- .000264
$C_{h\hat{\tau}}$.000063	.000074	.000063	.000056
$C_{h\delta}^A$	- .000013	- .000005	- .000013	- .000009

TABLE 5
COMPARISON OF FLAPERON HINGE-MOMENT DERIVATIVES OF BASIC paneled MODEL WITH INCORRECT AND CORRECT HINGE LINES, RIGID AIRPLANE

Control surface	Derivative (per rad)	Hinge line incorrect	Hinge line correct
Flaperon	C_{h_a}	-0.000367	-0.001146
	$C_{h_q}^{\wedge}$	- .002300	- .006373
	$C_{h_{\delta}}^S$	- .000434	- .005046
	$C_{h_u}^{\wedge}$	- .000038	- .000050
	$C_{h_a}^{\wedge}$	- .553539	-1.48630
	$C_{h_q}^{\wedge}$	- .004019	- .009279
	$C_{h_{\delta}}^S$	- .0000140	- .0000306
	$C_{h_{\beta}}$.000055	.000122
	$C_{h_p}^{\wedge}$	- .00009	- .000307
	$C_{h_r}^{\wedge}$	- .000030	- .000080
	$C_{h_{\delta}}^A$	- .000249	- .004548
	$C_{h_{\beta}}^{\wedge}$	- .004321	- .010653
	$C_{h_p}^{\wedge}$	- .000324	- .000993
	$C_{h_r}^{\wedge}$.000063	.000153
	$C_{h_{\delta}}^A$	- .000012	- .000027

TABLE 6
COMPARISON OF HINGE-MOMENT DERIVATIVES
FOR VARIOUS PANELING CONFIGURATIONS

Control surface	Derivative (per rad)	Basic paneling	Basic paneling with strake	Basic paneling I.D NF/FF on flaperon	LD paneling	Improved paneling
Flaperon	$C_{h\alpha}$	-0.001146	-0.001175	-0.001314	-0.00106	-0.001085
	$C_{h\alpha}^{\wedge}$	- .006373	- .006497	- .005763	- .005901	- .006351
	$C_{h\delta}^S$	- .005046	- .005112	- .0047185	- .0044235	- .0048215
	$C_{h\alpha}^{\wedge}$	- .000050	- .000053	- .000031	- .000047	- .000074
	$C_{h\alpha}^A$	-1.486299	-1.542958	- .716687	-1.35821	-1.550761
	$C_{h\alpha}^{\wedge}$	- .009279	- .009386	- .005248	- .008081	- .006351
	$C_{h\delta}^S$	- .0000306	- .0000309	- .000014	- .000026	- .00003018
	$C_{h\beta}$.000122	.000124	.000098	.000114	.000133
	$C_{h\beta}^{\wedge}$	- .000307	- .000309	- .000380	- .000283	- .000287
	$C_{h\gamma}^{\wedge}$	- .00008	- .000081	- .000068	- .000075	- .000080
	$C_{h\delta}^A$	- .004548	- .004593	- .004480	- .003965	- .004335
	$C_{h\beta}^A$	- .010653	- .010823	- .009226	- .010249	- .011605
	$C_{h\beta}^{\wedge}$	- .000993	- .001009	- .000641	- .000909	- .000967
	$C_{h\gamma}^A$.000153	.000156	.000131	.000147	.000164
	$C_{h\delta}^A$	- .000027	- .000028	- .000016	- .000024	- .000027

TABLE 6 (CONTD)
COMPARISON OF HINGE-MOMENT DERIVATIVES FOR VARIOUS PANELING CONFIGURATIONS

Control surface	Derivative (per rad)	Basic paneling	Basic paneling with strake	Basic paneling LD NF/FF on flaperon	LD paneling	Improved paneling
Horizontal tail	$C_{h\alpha}$	0.001921	0.001933	0.001493	0.002485	0.001755
	$C_{h\dot{q}}$	- .02255	- .022574	- .021331	- .017558	- .018783
	$C_{h\delta^S}$	- .004901	- .004895	- .004888	- .003062	- .004068
	$C_{h\dot{u}}$	- .000998	- .000939	- .001014	- .000891	- .000901
	$C_{h\dot{\alpha}}$	-8.51040	-8.594526	-7.34355	-7.882348	-7.107366
	$C_{h\dot{q}}$	- .106008	- .106329	- .106233	- .097523	- .094317
	$C_{h\delta^S}$	- .000136	- .000136	- .000136	- .000138	- .000120
	$C_{h\beta}$.001621	.001616	.001581	.000965	.001262
	$C_{h\dot{p}}$.000605	.000608	.000481	.000641	.000396
	$C_{h\dot{r}}$	- .00261	- .002624	- .002573	- .001879	- .002113
	$C_{h\delta^A}$	- .003846	- .003844	- .003844	- .0022214	- .0033692
	$C_{h\dot{\beta}}$.235522	.235626	.240377	.249017	.212466
	$C_{h\dot{p}}$	- .004839	- .004858	- .004516	- .00444	- .004311
	$C_{h\dot{r}}$	- .003898	- .003900	- .003958	- .004112	- .003557
	$C_{h\delta^A}$	- .0001219	- .0001219	- .0001219	- .0001219	- .000106

TABLE 6 (CONCLUDED)
COMPARISON OF HINGE-MOMENT DERIVATIVES FOR VARIOUS PANELING CONFIGURATIONS

Control surface	Derivative (per rad)	Basic paneling	Basic paneling with strake	Basic paneling LD NF/F on flapron	L/D paneling	Improved paneling
Rudder	$C_{h\beta}$	0.000700	0.000700	0.000701	0.000637	0.000651
	$C_{h\hat{p}}$.000132	.000129	0.000133	0.000121	0.000133
	$C_{h\hat{r}}$	- .001573	-0.001573	-0.001573	-0.001443	-0.001487
	$C_{h\delta}$	- .002043	-0.002043	-0.002043	-0.001797	-0.001983
	$C_{h\hat{\beta}}$.083185	0.083172	0.083136	0.075232	0.080189
	$C_{h\hat{p}}$.000412	0.000415	0.000407	0.000377	0.000407
	$C_{h\hat{r}}$	- .001504	-0.001504	-0.001503	-0.001337	-0.001459
	$C_{h\hat{\delta}}$	- .00001	-0.00001	-0.00001	-0.000008	-0.00001

TABLE 7
COMPARISON OF (BOEING) FLEXSTAB DERIVED HINGE MOMENTS $C_{h\alpha}$, $C_{h\delta}^S$ and $C_{h\delta}^A$
WITH WIND TUNNEL AND SIMULATION DATA, RIGID AIRPLANE

Control surface	Derivative (per rad)	Basic model	Basic model with strake	Basic model LD NF/FF	Low density paneling	Improved paneling	Wind tunnel	Simulation data
Flaperon	$C_{h\alpha}$	-0.001146	-0.001175	-0.001314	-0.00106	-0.001085	-0.001346	-0.001375
	$C_{h\delta}^S$	- .005046	- .005112	- .004719	- .004424	- .004822	- .002905	- .002750
	$C_{h\delta}^A$	- .004548	- .004593	- .00448	- .003965	- .004335	- .002950	- .002750
Horizontal tail	$C_{h\alpha}$	0.001921	0.001933	0.001493	0.002485	0.001755	0.0003151	0.001060
	$C_{h\delta}^S$	- .004901	- .004895	- .004888	- .003062	- .004068	- .007105	- .007160
	$C_{h\delta}^A$	- .003846	- .003844	- .003844	- .002221	- .003369	- .007105	- .007160
Rudder	$C_{h\beta}$	0.000700	0.000700	0.000701	0.000637	0.000651	0.000710	0.000515
	$C_{h\delta}$	- .002043	- .002043	- .002043	- .001797	- .001983	- .001048	- .000083

TABLE 8
METHODOLOGIES OF POTENTIAL-FLOW PROGRAMS

Program	Year developed	Panel geometry	Source panel	Doublet panel	Line source	Line doublet	Restrictions
FLEXSTAB	1971	Flat	Linear, $M < 1$ Constant, $M > 1$	Linear (constant vorticity)	Constant, $M < 1$ Linear, $M > 1$	Quadratic	Thin body, body of revolution
RHO 4	1974	Flat lifting surface					Planar lifting surface only, $M < 1$
TEA 230	1968	Flat for source, arbitrary for doublet	Constant	Constant			$M < 1$
PAN AIR pilot code	1975	Paraboloidal	Linear	Quadratic			